

# Kinematic wavefield attributes in seismic imaging

---

## Kinematische Wellenfeldattribute in seismischen Abbildungsverfahren

Zur Erlangung des akademischen Grades eines

DOKTORS DER NATURWISSENSCHAFTEN

bei der Fakultät für Physik  
der Universität Karlsruhe (TH)  
genehmigte

DISSERTATION

von

Dipl.-Geophys. Kai-Uwe Vieth  
aus Wilhelmshaven

Tag der mündlichen Prüfung:

25. Mai 2001

Referent:

Prof. Dr. Peter Hubral

Korreferent

Prof. Dr. Serge Shapiro



# Zusammenfassung

## Englische Fachbegriffe

Die vorliegende Dissertation ist mit Ausnahme dieser Zusammenfassung in englischer Sprache geschrieben. Da Veröffentlichungen in der Geophysik praktisch ausschließlich in Englisch verfasst werden, sind viele aus dem Englischen kommende Fachtermini auch in der deutschen Sprache gebräuchlich. Bei neueren Fachbegriffen – wie „Common-Reflection-Surface Stack“ – existiert oft kein angemessenes deutsches Äquivalent. In solchen Fällen wurde deshalb bewusst auf die Übersetzung verzichtet.

## Einleitung

Die Zielsetzung der seismischen Datenverarbeitung besteht darin die Lösung eines inversen Problems zu finden. Dabei möchte der Geophysiker oder speziell der Reflexionsseismiker mit Hilfe des aufgezeichneten Wellenfeldes ein geologisches Bild erhalten. Dieses Abbild des Erduntergrundes wird z.B. in der Erdölindustrie verwendet, um zu entscheiden, wo Bohrlöcher gebohrt werden. Falls ein Bohrloch „trocken“ ist, das heißt, dass kein Kohlenwasserstoffreservoir gefunden wurde, liegt der Verlust im Bereich mehrerer Millionen Dollar. Daher gibt es stets Bemühungen die Qualität bestehender Abbildungsverfahren zu verbessern und gleichzeitig die Kosten der Datenverarbeitung zu senken.

Im Prinzip benötigt der Geophysiker vier Schritte, um das Erdinnere abzubilden:

- i. Führe eine Datenakquisition durch, bei der jeder Tiefenpunkt mehrmals beleuchtet wird. Das Resultat sind sogenannte mehrfach überdeckte Daten.
- ii. Konstruiere ein erstes grobes, glattes elastisches Modell des Untergrundes.
- iii. Erstelle eine simulierte *zero-offset* (ZO) Sektion. Dies ist ein Seismogramm, bei dem Quelle und Empfänger an ein und demselben Ort sind.
- iv. Transformiere die ZO Sektion von dem Zeitbereich in den Tiefenbereich. Dieser Prozess wird als Tiefenmigration bezeichnet.

Jeder der vier Schritte ist in der geophysikalischen Literatur durch eine große Anzahl von Publikationen ausführlich dokumentiert. Ich möchte hier nur auf zwei exzellente Bücher

verweisen, die wiederum eine Vielzahl von Veröffentlichungen zitieren. Das Buch von Yilmaz (1987) beschäftigt sich mit vielen praktischen Aspekten der seismischen Datenverarbeitung, wohingegen sich das Buch von Sheriff und Geldart (1995) mehr auf die Theorie und die Seismologie konzentriert. Rein theoretisch und sehr ausführlich behandeln Aki und Richards (1980) die Wellenausbreitung in der Erde.

In dieser Arbeit konzentriere ich mich auf die Anwendung von drei kinematischen Wellenfeldattributen, mit der Absicht einerseits die Qualität der Bilder im Zeit- und Tiefenbereich zu verbessern und andererseits die Rechenzeit der letzten drei Schritte zu reduzieren. Dabei taucht die Frage auf: „Ist es möglich, dreiviertel des Abbildungsprozesses mit nur drei kinematischen Wellenfeldattributen zu bewältigen?“ Die Antwort lautet: „Im Prinzip ja.“ Natürlich ist die Anwendung der kinematischen Wellenfeldattribute von konventioneller Datenverarbeitung begleitet und die Attribute sind in konventionelle Konzepte eingearbeitet.

## Charakteristische Muster und Attribute in der Seismik

Mustererkennung und Musterbeschreibung sind die Basis wissenschaftlicher Arbeit. Ein ganzer Katalog seismischer Attribute steht zur Verfügung. Diese Attribute charakterisieren geometrische, kinematische, dynamische oder statistische Muster in den aufgezeichneten Daten. Chen und Sidney (1997) zählen ungefähr 80 seismische Attribute zur Reservoirbestimmung und Reservoirbeobachtung auf, die in den letzten 30 Jahren gefunden wurden. Zwei dieser Attribute werden in dieser Arbeit verwendet. Das eine ist der *semblance coefficient* (Ähnlichkeitskoeffizient), der für die Kohärenzanalyse eingesetzt wird. Das andere ist die Enveloppe, die hier im Bereich der zerstörungsfreien Prüfung eingesetzt wird. Die drei kinematischen Wellenfeldattribute, sprich die des *Common-Reflection-Surface (CRS) Stack*, sind nicht in dem Katalog erwähnt, da der CRS Stack sehr neu ist, Tygel et al. (1997). Dieser simuliert eine modellunabhängige ZO Sektion von mehrfach überdeckten Daten. Das heißt, dass keine Geschwindigkeitsinformationen über den Untergrund bekannt sein müssen. Die ZO Sektionen des CRS Stack sind durch die Kohärenzanalysen an den Daten bestimmt. Eine andere modellunabhängige ZO Simulationemethode ist die *multifocusing homeomorphic imaging* Methode. Die kinematischen Attribute dieser Methode werden zur Vorhersage und zur Abschwächung bzw. Unterdrückung von Mehrfachreflexionen angewandt, Keydar et al. (1998) und Zaske et al. (1999). Bevor ich einen Überblick über die Anwendungen der kinematischen Wellenfeldattribute des CRS Stack gebe, was einem Überblick dieser Arbeit gleichkommt, beschreibe ich kurz, nach welchen Mustern viele Reflexionsseismiker suchen, um das Erdinnere abzubilden.

Ein grundlegendes Muster in der Seismik ist eine hyperbolische Reflexionskurve, die man erhält, wenn das Signal einer Punktquelle von vielen Empfängern aufgezeichnet wird (*common-shot configuration*). Der Einfachheit halber befinden sich die Quelle und die Empfänger auf einer ebenen Erdoberfläche wie in Abbildung 1. Für eine ebene, horizontale Grenzschicht beschreibt die Reflexionskurve eine Hyperbel. Die Gleichung der Laufzeitkurve ist eine Funktion der Entfernung zwischen Quelle und Empfänger (*off-*

set), der Geschwindigkeit des Mediums oberhalb der Grenzschicht und der doppelten Laufzeit der Vertikalen zwischen Quelle und Reflektor. Falls der Reflektor geneigt oder gekrümmt ist, muss die Funktion der Laufzeitkurve entsprechend geändert werden, um die Reflexionskurve, oder Teile dieser, weiterhin richtig im Seismogramm beschreiben zu können. Die hyperbolische Laufzeitkurve im Seismogramm wird Primärreflexion genannt, wenn die propagierende Welle nur einmal auf ihrem Weg von der Quelle durch das Medium zu den Empfängern reflektiert wurde. Wird die eingestrahlte Welle mehrmals zwischen zwei Reflektoren reflektiert, treten die bereits oben erwähnten Mehrfachreflexionen auf. Theoretisch sind die kinematischen Wellenfeldattribute des CRS Stack immer mit Primärreflexionen verknüpft.

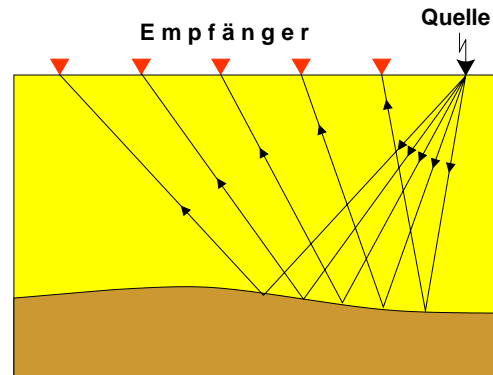


Abbildung 1: Common-shot configuration.

Jäger et al. (2001), Mann et al. (1999) und Müller (1999) haben gezeigt, dass der CRS Stack *zero-offset* Sektionen mit verbessertem Signal-zu-Rausch (S/N) Verhältnis und verbesserter Kontinuität der Reflexionsereignisse im Vergleich zu herkömmlichen ZO Simulationen erzeugt. Mit anderen Worten: Die charakteristischen Muster in den gemessenen Daten werden unter Verwendung des CRS Stack besser beschrieben als durch herkömmliche Methoden. Diese Ergebnisse haben mich ermutigt, mit den CRS Stack Attributen nach Anwendungen zu suchen, um weitere Schritte des Abbildungsprozesses des Erduntergrundes zu verbessern oder zu beschleunigen.

## Übersicht und Zusammenfassung der Arbeit

### Strahlentheorie

Die Strahlentheorie bildet die Basis für den CRS Stack, die *true-amplitude (TA)* Migration und die Inversion eines Geschwindigkeitsmodells. Die Hochfrequenzapproximation der akustischen Wellengleichung führt zur Beschreibung der Wellenpropagation mittels Strahlen. Dabei beschreibt die Eikonalgleichung (1) die Kinematik der Strahlen und die Transportgleichung (2) die Dynamik:

$$(\nabla\tau)^2 = \frac{1}{c^2} \quad (1)$$

$$2\nabla A \cdot \nabla\tau + A\nabla^2\tau = 0. \quad (2)$$

Die Gleichungen von Bortfeld (1989) beschreiben Laufzeiten in der näheren Umgebung eines (zentralen) Strahls, so genannte paraxiale Laufzeiten, mittels der *surface-to-surface* Propagatormatrix  $\underline{T}$ . Die Propagatormatrix verknüpft Verschiebungsvektoren und Differenzen von Langsamkeitsvektoren, die sich auf verschiedenen Flächen befinden, linear

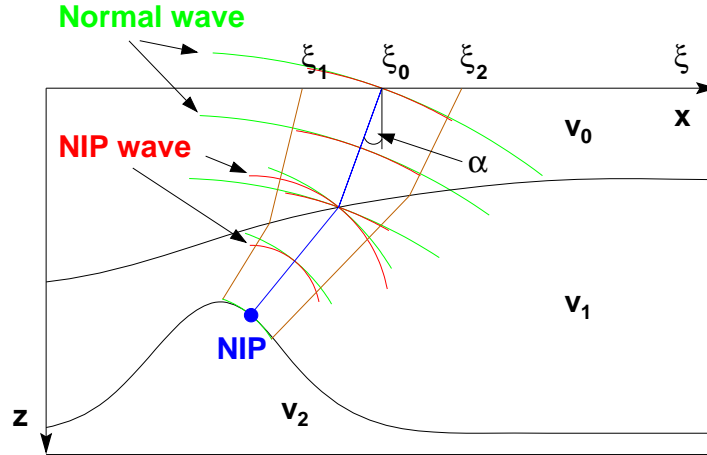


Abbildung 2: Illustration der NIP- und N-Eigenwellen sowie des Auftauchwinkels  $\alpha$ , des Normalstrahls.

miteinander, siehe Gleichung (2.13) und Abbildungen 2.1 und 2.2. Das Besondere daran ist, dass lediglich die Vektoren auf der Anfangs- und Endfläche bekannt sein müssen. Informationen über das Medium dazwischen sind nicht notwendig. Mit Hilfe der paraxialen Laufzeiten sowie der  $4 \times 4$  Matrix  $\underline{\mathbf{T}}$  bzw. ihrer vier  $2 \times 2$  Submatrizen werden die (erste) Fresnelzone, die (erste) projizierte Fresnelzone und der geometrische Ausbreitungsverlust (*geometrical spreading, GS*) von Hubral et al. (1992b) und Schleicher et al. (1997) ausgedrückt. Desweiteren basieren sowohl der CRS Stack als auch meine *parsimonious true-amplitude* Migration auf den Bortfeldschen Formulierungen.

Fast alle zitierten Veröffentlichungen in dieser Arbeit behandeln die 3-D Wellenausbreitung. Von Kapitel 2.3 an schreibe ich alle Gleichungen für den 2-D Fall. Der Grund dafür ist sehr einfach: Zum momentanen Zeitpunkt ist die praktische Arbeit mit dem CRS Stack für den 2-D *zero-offset* Fall möglich. Trotzdem können sämtliche Methoden, die in dieser Arbeit präsentiert werden, für 3-D erweitert und auch praktisch umgesetzt werden, wenn der 3-D CRS Stack programmtechnisch fertiggestellt ist.

### Common-Reflection-Surface Stack

Der Operator des CRS Stack wird durch die hyperbolische Laufzeitgleichung

$$t_{hyp}^2(\xi, h) = \left[ t_0 + \frac{2}{v_0}(\xi - \xi_0) \sin \alpha \right]^2 + \frac{2}{v_0} t_0 \cos^2 \alpha \left[ \frac{(\xi - \xi_0)^2}{R_N} + \frac{h^2}{R_{NIP}} \right] \quad (3)$$

im *midpoint-half-offset*-Zeitraum  $(\xi-h-t)$  beschrieben. Seien  $\xi_S$  und  $\xi_G$  die Akquisitionskordinaten von Quelle und Empfänger, so ist die *midpoint*-Koordinate  $\xi = (\xi_G + \xi_S)/2$  und die *half-offset*-Koordinate  $h = (\xi_G - \xi_S)/2$ . Die Zweiweglaufzeit des Normalstrahls ist  $t_0$ , die Mediumsgeschwindigkeit der ersten Schicht  $v_0$ . Die drei CRS Stack Attribute  $\alpha$ ,

---

$R_{NIP}$  und  $R_N$  entsprechen dem Auftauchwinkel des Normalstrahls an der Erdoberfläche, dem Radius der Wellenfront des explodierenden Diffraktors *NIP* (*normal incidence point*) und dem Radius der Wellenfront eines am Punkt *NIP* explodierenden Reflektorelementes, Hubral (1983). Anhand der Abbildung 2 wird deutlich, dass die CRS Stack Attribute integrative Größen sind. Das heißt, dass jedes Attribut durch den gesamten Verlauf des Normalstrahls vom Punkt *NIP* zum Auftauchpunkt  $\xi_0$  bestimmt ist. Durch eine Kohärenzanalyse entlang des CRS Stack Operators werden die CRS Stack Attribute gewählt, die die höchste Kohärenz aufweisen. Die Normalwelle besitzt am Punkt *NIP* dieselbe Krümmung wie der Reflektor. Diese Kurve wäre im Dreidimensionalen eine Fläche, eben eine *common-reflection-surface*. Die paraxialen Laufzeiten der Gleichung (3) spannen im  $(\xi-h-t)$  Raum eine Fläche auf, über die summiert wird. Das Summationsergebnis, die Stapelung (engl. *stack*), wird in den Punkt  $P_0$  mit den Koordinaten  $(\xi_0, h = 0, t_0)$  platziert, siehe Abbildung 3.3. Wird dies für alle Punkte der Ebene  $h = 0$  durchgeführt, ist das Ergebnis eine simulierte *zero-offset* Sektion.

Bislang ist die Größe der Apertur willkürlich bzw. auf der Basis von Erfahrungen gewählt worden. Eine minimale Apertur, die das beste S/N Verhältnis ergibt, stimmt mit der so genannten (ersten) projizierten Fresnelzone überein, die unter Verwendung der CRS Stack Attribute ausgedrückt werden kann, siehe Gleichung (3.11) für die parabolische Laufzeitformel (3.2) bzw. Gleichung (3.12) für die hyperbolische Laufzeitformel (3). Da stets von der ersten Fresnelzone oder ersten projizierten Fresnelzone die Rede ist, wird das Wort „erste(n)“ im weiteren nicht mehr erwähnt. Im 2-D Fall, der hier immer betrachtet wird, reduziert sich die Fresnelzone auf eine „Fresnelkurve“. Ich bleibe jedoch bei dem Ausdruck Fresnelzone. Geometrisch betrachtet ist die projizierte Fresnelzone die erste Fresnelzone auf dem Reflektor projiziert entlang von paraxialen Normalstrahlen auf die Akquisitionsfläche. In Abbildung 2 ist der blaue Strahl der (normale) Zentralstrahl und die braunen (normalen) Strahlen sind zugehörige Paraxialstrahlen. Die erste Fresnelzone auf dem Reflektor entspricht lokal der Normalwelle am Punkt *NIP* und ist begrenzt durch die Paraxialstrahlen, die im Zeitbereich folgendes Kriterium erfüllen: Die Laufzeitdifferenz zwischen dem reflektierten Paraxialstrahl und dem diffraktierten Strahl, der durch die Punkte  $\xi_1$  und *NIP* verbunden ist, ist gleich der Länge des Signals  $T_W$  bzw. im Frequenzbereich gleich der halben Länge der Periode  $T$  eines monofrequenten Signals. Dies gilt natürlich auch für den Paraxialstrahl, der die zweite Grenze der projizierten Fresnelzone  $\xi_2$  markiert. Damit wird die Apertur für ZO berechnet und basiert nicht mehr auf Abschätzungen und Erfahrungen.

Da sich der CRS Stack Operator über endliche *offsets* erstreckt, die Gleichungen jedoch nur für ZO gelten, habe ich eine Näherung auf der Basis der Arbeit von Kvasnička and Červený (1996) vorgeschlagen. Da die Implementation dieser Näherung in den bestehenden CRS Stack sehr zeitintensiv sein wird, steht diese Arbeit noch aus. Trotzdem wird die projizierte Fresnelzone zur Bestimmung der Apertur bereits im CRS Stack wie folgt genutzt: Für den neuen Fresnel CRS Stack wird die Ellipse in Abbildung 3.8 als Apertur verwendet. Für ZO entspricht die Apertur (kleine Achse der Ellipse) der projizierten Fresnelzone, die große Halbachse der Ellipse entspricht in *half-offset* Richtung ebenfalls der projizierten Fresnelzone.

An einem realen Datenbeispiel (zur Verfügung gestellt von der BEB Erdöl Erdgas GmbH) ist zu erkennen, dass der Fresnel CRS Stack der Abbildung 3.12 nicht nur besser ist als die entsprechende konventionelle ZO Simulation in Abbildung 3.9, sondern auch besser ist als der bereits existierende Initial CRS Stack (Abbildung 3.11) und Optimised CRS Stack (Abbildung 3.10). Was bedeutet hier „besser“? Zum einen ist das S/N Verhältnis gegenüber den anderen ZO Simulationen größer geworden, zum anderen wurde die Auflösung erhöht, ohne dass die Kontinuität der Reflexionsereignisse nachgelassen hat. In den Kästen A bis D sind Unterschiede in den Sektionen gut erkennbar.

In der Theorie wird davon ausgegangen, dass der geometrische Ausbreitungsverlust in einem geschichteten Medium, z.B. eine Schicht von Meeressedimenten, gegenüber allen anderen Verlusten während der Wellenpropagation dominiert. Kann man den geometrischen Ausbreitungsverlust rückgängig machen, erhält man ein Seismogramm das, Reflexionsereignisse zu großen Laufzeiten sichtbar macht, und was viel bedeutender ist, die Amplituden der Reflexionsereignisse geben, bis auf einen konstanten Faktor, die Quellstärke, den Reflexionskoeffizienten der jeweiligen geologischen Grenzschichten wieder. Der 2-D GS Faktor (3.16) berechnet nur den Verlust in der Strahlebene (*in-plane GS*). In der realen Erde findet der Ausbreitungsverlust auch senkrecht dazu statt (*out-of-plane GS*). Dieser kann mittels Gleichung (3.18) approximiert werden.

Dadurch, dass der Ausbreitungsverlust durch die CRS Stack Attribute berechnet werden kann, ist es nicht mehr notwendig, einen beliebigen Verstärkungsfaktor zu verwenden, um Reflexionsereignisse sichtbar zu machen. Desweiteren sind die Amplituden in den GS-korrigierten ZO Sektionen ein Maß für die Impedanzkontraste im Untergrund und liefern somit direkt geologische Informationen. Voraussetzung für die Verwendbarkeit der Informationen ist ein so genanntes *true-amplitude pre-processing*. Leider wurde auf die Erhaltung der Amplitudenverhältnisse während der Datenverarbeitung des BEB Datensatzes nicht konsequent geachtet. Die Unterschiede und Vorteile zwischen Abbild 3.12, konventioneller Verstärkungsfaktor, und Abbild 3.13, *in-plane GS*- und *out-of-plane GS*-Faktor, sind dennoch zu sehen. Alle Reflexionsereignisse sind in Abbildung 3.13 zu erkennen; nahe der Oberfläche sind sie schwächer. Die große, stark verrauschte Region unterhalb der Domstruktur wurde nicht hervorgehoben, sondern abgeschwächt.

Der neue Fresnel CRS Stack, die projizierte Fresnelzone sowie der geometrische Ausbreitungsverlust finden in den kommenden Abschnitten weitere Verwendung.

### **True-amplitude Migration mit CRS Stack Attributen**

Das Ziel der *true-amplitude* Migration ist die Transformation der ZO Sektion aus dem Zeitbereich in den Tiefenbereich unter Berücksichtigung der Amplituden. Das heißt, dass die Amplituden nach der Transformation den Reflexionskoeffizienten der Grenzschichten entsprechen, bzw. um einen konstanten Faktor abweichen. Für die TA Migration verwende ich die gewichtete modifizierte Diffraktionsstapelung von Schleicher et al. (1993).

---

Diese Migration vom Kirchhofftyp geht davon aus, dass der Untergrund aus Diffraktionspunkten zusammengesetzt ist. Gleichung (4.4) ist die entsprechende zweidimensionale TA Migration. In Worte gefaßt geht man bei diesem Typ der *post-stack* Kirchhoff-Migration wie folgt vor, siehe dazu Abbildung 4.2:

- i. Für einen beliebigen Punkt  $M$  im Untergrund, welcher nicht mit einem Punkt  $M_R$  auf einem Reflektor übereinstimmen muß, werden mittels *ray tracing* Strahlen zu jedem ZO Quell-Empfänger Paar gezogen. Damit ist die Diffraktionskurve  $T_D$  bekannt.
- ii. Die antikausale halbe Zeitableitung wird von jeder analytischen Spur berechnet. Der Imaginärteil der analytischen Spur wird mit Hilfe der Hilberttransformierten der realen, sprich gemessenen, Spur berechnet.
- iii. Jeder Punkt der Diffraktionskurve wird mit der Gewichtsfunktion (4.10) multipliziert.
- iv. Die Daten entlang der Diffraktionskurve werden gestapelt, das heißt aufsummiert, mit  $1/\sqrt{2\pi}$  multipliziert und in den zugehörigen Diffraktionspunkt in die Tiefe platziert.
- v. Dies wird für jeden Punkt des diskretisierten Untergrundes durchgeführt.

Nachdem die konventionelle Methode bekannt ist, erkläre ich meine 2-D *parsimonious true-amplitude* Migration. Das Wort „parsimonious“ heißt übersetzt „geizig“ oder „sparsam“. Im Laufe der Erläuterungen wird deutlich bzw. weise ich darauf hin, warum dieses Adjektiv gewählt wurde.

Eine simulierte ZO Sektion des CRS Stack dient als Eingangsdatensatz für die *parsimonious* TA Migration. Die zugehörigen CRS Stack Attribute werden entweder für eine Migration mittels Stapelung oder *mapping* verwendet. Zunächst gehe ich auf die Migration mittels Stapelung ein. Die Diffraktionskurve wird mit der hyperbolischen paraxialen Laufzeitgleichung (3) berechnet, indem  $R_N = R_{NIP}$  gesetzt wird. Damit hat die Normalwelle am Punkt  $NIP$  den Radius Null, entsprechend eines Diffraktionspunktes. Folglich ist das aufwändige *ray tracing* wie in Punkt i.) bzw. Abbildung 4.2 nicht erforderlich. Desweiteren wird nicht entlang der gesamten Diffraktionskurve, die durch die Aufnahmegeometrie beschränkt ist, aufsummiert, sondern nur innerhalb der projizierten Fresnelzone, siehe gestrichelte Linien ausgehend von  $\xi_1$  und  $\xi_2$  in Abbildung 4.3.

In der Abbildung ist zu sehen, dass die projizierte Fresnelzone um den stationären Punkt  $N_R$  platziert wurde. Der stationäre Punkt ist derjenige, an dem die Diffraktionskurve  $T_D$  und die Reflexionskurve  $T_R$  tangential zueinander sind. Den Hauptanteil des reflektierten Signals erhält man durch die Aufsummierung innerhalb der projizierten Fresnelzone zentriert um den stationären Punkt. Dies wurde ausführlich von Schleicher et al. (1997) und Sun (1998) gezeigt. Sie haben auch gezeigt, dass sich das S/N Verhältnis verschlechtert, wenn die Apertur größer gewählt wird, und dass das Migrationsrauschen zunimmt, wenn der stationäre Punkt am Rand bzw. außerhalb der Apertur liegt. Folglich ist die

Kenntnis des stationären Punktes wichtig, um ein Abbild guter Qualität zu erhalten. Der Auftauchpunkt des Normalstrahls entspricht dem stationären Punkt. Da mit jedem Zeitsample des CRS Stack ein Normalstrahl verknüpft ist, ist der stationäre Punkt gleich der  $\xi$ -Koordinate eines jeden Zeitsamples. Bislang ist der CRS Stack das einzige Verfahren, das automatisch die Lage des stationären Punktes liefert.

Nachdem die analytische Spur und die antikausale halbe Zeitableitung berechnet und die Signale auf der Diffraktionskurve mit der Gewichtsfunktion multipliziert wurden, wird das innerhalb der projizierten Fresnelzone gestapelte Signal in den Punkt  $M_R = NIP$  platziert. Hierfür wird lediglich ein Strahl, der Normalstrahl von  $\xi_0$  zu  $M_R = NIP$ , gezogen. Ein Nachteil besteht darin, dass die Strahlen nicht von jedem Punkt in der Tiefe zu jeder ZO Lokation entlang der  $\xi$ -Achse gezogen werden, sondern „nur“ jeder Normalstrahl, dessen Lage über den Zeitbereich und den Auftauchwinkel bestimmt ist: Nicht jedem Punkt im diskretisierten Tiefenbereich wird ein Signal zugeordnet. Dies geschieht aufgrund der Fokussierung und Defokussierung von Strahlen, während sie durch das Geschwindigkeitsmodell gezogen werden, es sei denn, dieses ist sehr einfach. Die entstehenden Lücken in den Reflektoren sind deutlich in Abbildung 4.12 zu sehen.

Diese Lücken schließen sich, wenn zwei weitere Normalstrahlen durch das Modell gezogen werden. Diese paraxialen Normalstrahlen starten an den Rändern der projizierten Fresnelzone. Die zugehörigen Auftauchwinkel und Laufzeiten werden mit den Gleichungen (4.12) bis (4.14) von Höcht et al. (1999) berechnet. Zusätzlich wird die Normalwelle in den Punkt  $NIP$  zurückpropagiert. Die Schnittpunkte der paraxialen Normalstrahlen mit der Normalwelle bei  $NIP$  stimmen näherungsweise mit den Grenzen der tatsächlichen ersten Fresnelzone auf der Grenzschicht überein. Nun wird das gestapelte Signal nicht nur dem Punkt  $M_R$  zugeordnet, sondern allen Punkten auf der Fresnelzone mit Krümmungsradius  $R_N$  am Punkt  $M_R = NIP$ . Abbildung 4.13 zeigt, dass alle Lücken geschlossen sind.

Eine schnellere Methode als das Stapeln ist das *mapping*. Dabei wird die ZO Sektion des CRS Stack mit dem entsprechenden *geometrical spreading* multipliziert, was dem gewünschten *true-amplitude* Signal (4.3) gleicht. Dies kann direkt dem jeweiligen Tiefenpunkt bzw. der Fresnelzone in der Tiefe zugeordnet werden.

Mit Hilfe von verrauschten und unverrauschten synthetischen, mehrfach überdeckten Daten wurde der Initial und Fresnel CRS Stack generiert. Ich habe zuerst überprüft, ob die Amplituden der ZO Simulationen mit, per *ray tracing* bestimmten, ZO Amplituden übereinstimmen. Die Abweichungen des Fresnel CRS Stack waren sehr gering und deutlich kleiner als die des Initial CRS Stack, Abbildungen 4.7 bis 4.10. Bei den durchgeführten Migrationen hat sich herausgestellt, dass das Ergebnis der *mapping* Methode, angewandt auf den Fresnel CRS Stack, die besten Werte liefert, Abbildungen 4.14 bis 4.21.

Die *parsimonious* TA Migration wurde auf einen Ausschnitt des BEB Datensatzes angewandt, siehe Abbildung 5.7. Da nur ein *ray tracer* für geschichtete Medien zur Verfügung stand, der auch die CRS Stack Attribute verarbeiten konnte, war es nicht möglich, die Migration auf den kompletten BEB Datensatz anzuwenden, siehe dazu auch den nächsten

---

Abschnitt. Wenn ein *ray tracer* mit entsprechenden Möglichkeiten für so genannte Hintergrundgeschwindigkeitsmodelle zur Verfügung stünde, hätte der gesamte BEB Datensatz migriert werden können.

### **Erstellung eines Geschwindigkeitsmodells mittels CRS Stack Attributen**

Für die Simulation der ZO Sektion und für die Berechnung der projizierten Fresnelzone, des geometrischen Ausbreitungsverlustes oder der Diffraktionskurve war kein Geschwindigkeitsmodell erforderlich. Sämtliche Resultate waren datenabhängig. Die Tiefenmigration bedingt ein Geschwindigkeitsmodell. Unter der Verwendung der Horizont-Inversion von Majer (2000) kann ein geschichtetes Geschwindigkeitsmodell mit konstanten Schichtgeschwindigkeiten produziert werden. Bislang war es nur möglich, synthetische Daten zu verwenden, da die Fluktuationen der CRS Stack Attribute dann sehr klein waren. Da sich dies bei realen Daten dramatisch ändert, musste ein Glättungsalgorithmus gefunden werden, der eine stabile Inversion garantiert. Mit der Implementation der *robust locally weighted regression* von Cleveland (1979) ist es nun möglich, CRS Stack Attribute von Realdaten zu invertieren, um ein Geschwindigkeitsmodell zu erstellen. Die Horizont-Inversion ergab ein Geschwindigkeitsmodell für einen Teil des BEB Datensatzes, das dem Geschwindigkeitsmodell der konventionellen Methode (NMO/DMO Analyse) ähnlich ist.

Die Stabilisierung der Inversion von Realdaten schließt den Kreis der rein datenabhängigen *true-amplitude* Migration. Für komplexere ZO Sektionen müssen Lösungen gefunden werden, die die Lücken in den Daten schließen, wenn ein Horizont dadurch unterbrochen wurde, dass die Daten im Zeitbereich nicht geeignet waren. Das tritt z.B. dann auf, wenn das S/N Verhältnis sehr klein ist oder wenn kollabierende Strukturen ein Reflexionsereignis unterbrechen, siehe Box A in Abbildung 3.12.

### **Anwendung des CRS Stack und der Migration in der zerstörungsfreien Prüfung**

Der CRS Stack wurde zum ersten Mal im Bereich der zerstörungsfreien Prüfung (*non-destructive testing, NDT*) angewandt. Die synthetischen Modelle repräsentieren Beton, der nicht wie die Erde als geschichtetes Medium modelliert wird, sondern als ein zufallsverteiltes Medium. Risse oder Fremdkörper, die in dem Beton eingebettet sind, sollen abgebildet werden. Die übliche Datenakquisition in NDT besteht aus ein oder zwei Spuren (*zero-offset* und ein *offset*). Die verwendete Quelle emittiert eher eine ebene Welle als eine Kugelwelle. Diese Vereinfachungen beschränken die Möglichkeiten bei der Abbildung. Um die Vorteile eines mehrfach überdeckten Datensatzes, wie er in der Reflexionsseismik üblich ist, zu zeigen, wurde ein solcher für zufallsverteilte Medien mittels Finite-Differenzen-Methoden erstellt. Anschließend hat der CRS Stack aus dem Datensatz eine ZO Sektion generiert. Im Vergleich mit dem Standardverfahren in NDT zeigt der Fresnel CRS Stack deutlich den geeigneten Einschluss, siehe Abbildungen 6.21, 6.22 und 6.24.

Für die Tiefenmigration ist eine standardmäßige 2-D Kirchhoff-Migration mit konstanter Geschwindigkeit eingesetzt worden. Das Novum bei letzterem ist, dass während der Migration eine Kohärenzanalyse gemacht wird. Ein Kohärenzmaß ist die in der Geophysik weit verbreitete *semblance*, Neidell and Taner (1971). Ein anderes Kohärenzmaß ist die  $\sigma$ -Korrelation (Gelchinsky et al., 1986), die unterschiedliche Phasengeschwindigkeiten berücksichtigt. Die Ableitung der *semblance* wurde als neues Attribut eingeführt, um die Auflösung der zugehörigen *semblance* Sektion zu erhöhen. Es hat sich bei den drei verschiedenen Modellen gezeigt, dass der Riss oder die Fremdkörper in den *semblance* Sektionen deutlich zu erkennen waren und ihre Lokalisierung in den tiefenmigrierten Bildern verbessert werden konnte. Diese Aussage trifft bei der  $\sigma$ -Korrelation und bei der Ableitung der *semblance* nur auf die Experimente zu, bei denen eine ebene Welle in das Medium eingebracht wurde. Bei dem mehrfach überdeckten Datensatz, bei dem der CRS Stack zur Anwendung kam, wurde eine Punktquelle eingesetzt. Bei diesem Datensatz konnten keine verwertbaren Ergebnisse mit der  $\sigma$ -Korrelation oder der Ableitung der *semblance* erzielt werden, was eventuell an dem deutlich schlechteren S/N Verhältnis im Vergleich zum Ebene-Welle Experiment lag. Die Anwendung des CRS Stack und der Kohärenzanalyse während der Migration an Realdaten wäre eine zukünftige Arbeit.

### Schlussbemerkung

Es hat sich gezeigt, dass für die kinematischen CRS Stack Attribute eine Vielzahl von Anwendungsmöglichkeiten existieren. Die bereits bestehenden Verfahren können auf 2-D *finite-offset* und 3-D erweitert werden. Eine sehr interessante neue Anwendung wäre die *angle-versus-offset* (AVO) Analyse, die durch einen 2-D *finite-offset* CRS Stack möglich wird.

# Contents

<b>Zusammenfassung</b>	<b>i</b>
<b>Abstract</b>	<b>xv</b>
<b>1 Introduction</b>	<b>1</b>
1.1 Patterns and attributes in seismics . . . . .	2
1.2 Overview of this thesis . . . . .	3
<b>2 Ray theory</b>	<b>5</b>
2.1 Basics . . . . .	5
2.1.1 Wave equation . . . . .	5
2.1.2 Eikonal and transport equation . . . . .	6
2.1.3 2-D wave propagation . . . . .	8
2.2 Paraxial rays and propagator matrix . . . . .	8
2.2.1 Rays in 2-D . . . . .	10
2.3 Paraxial traveltimes . . . . .	10
2.4 Fresnel zone . . . . .	11
2.5 Projected Fresnel zone . . . . .	13
2.6 Geometrical spreading . . . . .	16
2.6.1 Geometrical spreading in 2-D . . . . .	16
2.6.2 Geometrical spreading in 2.5-D . . . . .	19
<b>3 Common-Reflection-Surface Stack</b>	<b>21</b>
3.1 Basics . . . . .	21
3.1.1 Conventional stacking . . . . .	21
3.1.2 Eigenwaves . . . . .	23
3.1.3 CRS traveltimes . . . . .	23
3.1.4 Comparison of traveltimes equations . . . . .	25
3.1.5 Parameter search . . . . .	26
3.2 Application of attributes . . . . .	28
3.2.1 Projected Fresnel zone . . . . .	28
3.2.2 Projected Fresnel zone for finite-offset configuration . . . . .	29
3.2.3 Proposal for an aperture in offset-direction . . . . .	32
3.2.3.1 Implementation . . . . .	32
3.2.4 Geometrical spreading in terms of CRS Stack attributes . . . . .	34

3.2.5	Discussion . . . . .	34
3.3	Real data example . . . . .	35
3.3.1	The new Fresnel CRS Stack compared with the old CRS stacks . . . . .	38
3.3.2	CRS Stack attribute sections and new applications . . . . .	40
<b>4</b>	<b>True-amplitude migration with CRS Stack attributes</b>	<b>45</b>
4.1	2-D true-amplitude Kirchhoff migration . . . . .	46
4.1.1	2.5-D true-amplitude Kirchhoff migration . . . . .	49
4.1.2	Stationary point . . . . .	49
4.1.3	Steps of conventional 2-D TA Kirchhoff migration . . . . .	50
4.2	Parsimonious 2-D true-amplitude migration . . . . .	50
4.2.1	Stacking . . . . .	51
4.2.2	Mapping . . . . .	53
4.2.3	Data selection via CRS Stack coherence section . . . . .	53
4.3	Synthetic example . . . . .	54
4.3.1	True-amplitude CRS Stack . . . . .	55
4.3.2	True-amplitude migration . . . . .	55
4.3.3	Geometrical spreading for map migration and as a “natural” gain function . . . . .	62
4.3.4	2.5-D migration . . . . .	63
<b>5</b>	<b>Velocity model derived by CRS Stack attributes</b>	<b>65</b>
5.1	Horizon inversion . . . . .	65
5.2	Robust locally weighted regression . . . . .	67
5.3	Real data example . . . . .	68
5.3.1	Data picking . . . . .	68
5.3.2	Data smoothing . . . . .	69
5.3.3	Velocity model . . . . .	69
5.3.4	Parsimonious 2.5-D TA migration . . . . .	72
<b>6</b>	<b>Application of CRS Stack and migration in non-destructive testing</b>	<b>75</b>
6.1	Random media . . . . .	75
6.2	Data acquisition in non-destructive testing . . . . .	76
6.3	Wavefield attributes and coherence measures for imaging . . . . .	77
6.3.1	Envelope . . . . .	77
6.3.2	Semblance and derivative of semblance . . . . .	77
6.3.3	$\sigma$ -correlation — a combined phase and group correlation . . . . .	78
6.3.3.1	$\sigma$ -correlation . . . . .	80
6.4	Migration and correlation . . . . .	81
6.4.1	Crack-model . . . . .	81
6.4.2	Poly-model . . . . .	86
6.5	Dip-model — The CRS Stack in NDT . . . . .	90
<b>7</b>	<b>Conclusions and perspectives</b>	<b>93</b>
	<b>References</b>	<b>95</b>

<b>A</b>	<b>Some properties of the ray propagator matrix</b>	<b>101</b>
A.1	Reverse ray . . . . .	101
A.2	Symplecticity . . . . .	101
A.3	Chain rule . . . . .	102
<b>B</b>	<b>Projected Fresnel zone - finite-offset configuration</b>	<b>103</b>
	<b>Index</b>	<b>107</b>
	<b>Danksagung</b>	<b>109</b>
	<b>Lebenslauf</b>	<b>111</b>



# Abstract

In my thesis I make use of kinematic wavefield attributes to improve the quality of 2-D seismic images and to reduce the computation time for processing. With the kinematic wavefield attributes of the model independent Common-Reflection-Surface Stack I (i) determine the minimum aperture for stacking, (ii) compute the geometrical spreading which is required for true-amplitude processing and (iii) developed a parsimonious true-amplitude zero-offset post-stack migration.

The minimum aperture is defined by the projected first Fresnel zone and yields a zero-offset section with the optimal signal-to-noise ratio. The geometrical spreading is used as a “natural” data-driven gain function which is exact for 2-D and approximated for 2.5-D. With the Common-Reflection-Surface Stack the normal ray associated with each zero-offset sample is known. Instead of tracing many rays for each diffraction point in order to obtain the corresponding diffraction traveltime curve, I only trace the normal ray down and approximate the diffraction traveltime curve by means of the kinematic wavefield attributes.

The simulation of the zero-offset section, the computation of the projected Fresnel zone, and the geometrical spreading are data-driven. However, for the migration I need a macro-velocity model. A co-worker used the attributes for a velocity model inversion using synthetic data. With the application of a robust locally weighted regression, I make the inversion process stable for real data. Thus, I present the complete processing chain – zero-offset simulation, velocity model inversion, depth migration – to obtain a subsurface image without the use of an initial velocity model but by means of data-driven attributes.

For the first time, the Common-Reflection-Surface Stack is applied to synthetic non-destructive testing data where the elastic waves propagate through a random medium which represents concrete. An effective constant velocity is used for the post-stack depth migration of the zero-offset section. During the migration two different coherence analyses are performed with the aim to better localise a crack or a foreign body within the concrete.



# Chapter 1

## Introduction

The purpose of seismic data processing is to solve the inverse problem. That is, given the recorded wavefield, geophysicists want to determine the geologic structure. This image of the earth's subsurface serves, for example, in the oil industry as a reference to decide where bore-holes are going to be drilled. If a bore-hole is "dry", i.e., no hydrocarbon reservoir was found, the loss is in the range of millions of dollars. Therefore, the aim is to find methods which improve the quality of today's images and to decrease the cost of data processing. The work on hand is a contribution to those aims.

In principle the geophysicist has to perform four steps in order to obtain an image of the earth's subsurface:

- i. Acquire data which illuminate each depth point several times. The result is a so-called multi-coverage data set.
- ii. Construct an initial macro-earth model.
- iii. Produce a simulated zero-offset (ZO) section. It is a seismogram where source and receiver are at coincident location.
- iv. Transform the time domain ZO section into the depth domain. This process is termed time-to-depth migration or simply post-stack depth migration.

Each of the four steps is documented in the geophysics literature by an immense number of publications – using pre-stack depth migration (PreSDM), item iii. and iv. reduce to one step. In this thesis, I focus on the application of three kinematic wavefield attributes with the intention to reduce the computation time of the last three steps and to improve the quality of the time and depth domain sections. The question that arises is: Is it possible to cover three quarter of the imaging process with just three kinematic attributes? The answer is: In principle, yes. Of course, conventional processing accompanies the application of the kinematic wavefield attributes and they are embedded in conventional concepts.

## 1.1 Patterns and attributes in seismics

Pattern recognition and pattern description is the basis for scientific work. A whole catalogue of seismic attributes is available which describes specific measurements of geometric, kinematic, dynamic or statistical patterns derived from seismic data. Chen and Sidney (1997) list about 80 seismic attributes for reservoir forecasting and monitoring found in the last 30 years. Two of them are used in this thesis: The semblance coefficient which is used for coherence analysis and the envelope that is applied to non-destructive testing data. The three kinematic wavefield attributes, namely the Common-Reflection-Surface (CRS) Stack attributes, are not mentioned in the list because the CRS Stack is quite new, Tygel et al. (1997). It simulates a model-independent ZO section from multi-coverage data. This means that no initial velocity information is required. The CRS Stack is data-driven using coherence analysis. Another model-independent ZO simulation method is the multifocusing homeomorphic imaging technique. Its kinematic attributes are used to predict and attenuate multiples, Keydar et al. (1998) and Zaske et al. (1999). Before I give an overview of the applications of the kinematic wavefield attributes of the CRS Stack which is equivalent to an overview of the thesis, I describe what kind of patterns many geophysicists, including me, are looking for in order to image the subsurface.

In seismics, a fundamental pattern is the hyperbolic reflection event that is obtained if the signal of a point source is recorded by many receivers (common-shot configuration). Shot and receivers are, for simplicity, supposed to be on a flat earth's surface as depicted in Figure 1.1. For a flat horizontal interface and a homogeneous overburden the reflection event is a hyperbola which is described by the Pythagorean theorem. The traveltime equation is a function of the distance between source and receiver (offset), the velocity of the medium above the interface and the traveltime of twice the vertical path from the source to the interface. If the interface dips or is curved, the traveltime function has to be changed in order to describe the hyperbolic curve or parts of it in the seismogram. The hyperbolic traveltime curve in the seismogram is called primary reflection if the propagating wave was reflected only once along its path from the source through the earth to the receivers. The kinematic wavefield attributes of the CRS Stack are always related to primary reflections.

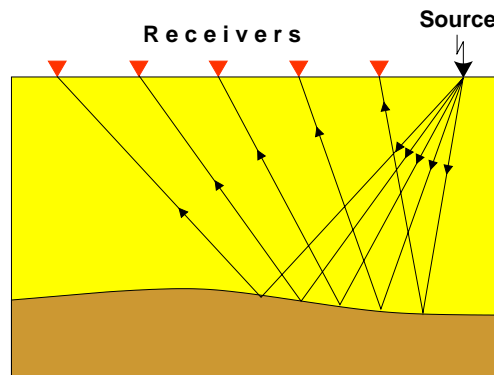


Figure 1.1: Common-shot configuration.

Jäger et al. (2001), Mann et al. (1999), and Müller (1999) showed that the CRS Stack yields zero-offset sections with increased signal-to-noise ratio and increased continuity of reflection events compared to conventional ZO simulations, like PreSDM or normal-moveout/dip-moveout (NMO/DMO) Stack. In other words, the patterns in the recorded

data are better described by the use of the new CRS Stack than by conventional methods.

## 1.2 Overview of this thesis

The fundamentals of ray theory are summarised in Chapter 2 which are needed to gain a comprehensive understanding of the CRS Stack, the true-amplitude (TA) migration, and the velocity model inversion. It shows that the high-frequency solution of the acoustic wave equation leads to the description of wave propagation by means of rays. Bortfeld's formulation of paraxial traveltimes by means of the surface-to-surface propagator matrix  $\underline{\mathbf{T}}$  in 1989 are the basis for the Fresnel zone, projected Fresnel zone and the geometrical spreading as expressed by Hubral et al. (1992b) and Schleicher et al. (1997). The cited publications (also in the following chapters) usually handle 3-D wave propagation. From Section 2.3 on, I express all equations for the 2-D case. The reason is simple: At the present stage, the CRS Stack works, in practice, for 2-D zero-offset. All methods presented in the thesis can be extended to 3-D, once the 3-D CRS Stack is available.

In Chapter 3, I write down the basics of the CRS Stack and present the first applications to a real data set. There, the projected Fresnel zone and the geometrical spreading is expressed in terms of CRS Stack attributes. An application of the projected Fresnel zone is given with the new Fresnel CRS Stack and I propose how to choose the stacking aperture for finite-offset. The geometrical spreading is utilised as a "natural" gain function to enhance weak reflections at large ZO traveltimes. The out-of-plane geometrical spreading is approximated by CRS Stack attributes. Thus, the "natural" gain function is applicable to real data if the subsurface parameters do not vary perpendicular to the acquisition line (2.5-D situation) and if the velocity distribution is well described by the root-mean-square (RMS) velocity.

Both, the projected Fresnel zone and the geometrical spreading, in terms of data-driven CRS Stack attributes, are of major importance for my parsimonious true-amplitude migration in Chapter 4. The migration is parsimonious with respect to three items: 1.) It makes use of the minimal migration aperture, determined by the projected Fresnel zone. As it is centered around the stationary point, it is also the optimal migration aperture, Schleicher et al. (1997) and Sun (1998). 2.) The diffraction curve which is required for the diffraction stack is not determined by ray tracing but is given by an analytical hyperbolic expression. 3.) Only a maximum of three rays have to be traced in order to assign the stacked signal to the corresponding depth point.

I use synthetic data for the tests in Chapter 4. First, I check whether an output of the CRS Stack is suitable for a TA migration. Second, I test the parsimonious true-amplitude migration.

A velocity model was not needed for the simulation of the ZO section as well as for the computation of the projected Fresnel zone or the geometrical spreading. However, a velocity model is required for the time-to-depth migration. In Chapter 5, the CRS Stack attributes of a real data set enter the horizon inversion of Majer (2000) which produces

a layered velocity model with constant layer velocities. Before, it was only possible to use synthetic data as the fluctuations of the CRS Stack attributes were small. As this changes dramatically in a real data set, a smoothing algorithm had to be found to guarantee a stable inversion. For this task, I employed the robust locally weighted regression of Cleveland (1979) and tested it on the real data set of Chapter 3.

In Chapter 6, the CRS Stack is, for the first time, applied to the area of non-destructive testing (NDT). The synthetic models represent concrete which is not modelled as a layered medium, like the earth, but as a random medium. Cracks or foreign bodies, embedded in the concrete, have to be imaged. The standard data acquisition in NDT consists of one or two traces (zero-offset and one offset) with sources emitting rather plane waves than spherical waves. This simplicity restricts the capabilities of imaging. In order to show the advantages of a multi-coverage data set in imaging, as it is common practice in reflection seismics, such a data set was generated with a subsequent application of the CRS Stack. For the time-to-depth migration, a standard 2-D constant velocity Kirchhoff migration was utilised. There, the novelty is a coherence analysis performed during migration. One coherence measure is the semblance (Neidell and Taner, 1971) another is the  $\sigma$ -correlation (Gelchinsky et al., 1986), which accounts for different phase velocities. The derivative of the semblance is introduced as a new attribute in order to increase the resolution of the corresponding semblance section.

## Chapter 2

# Ray theory

Ray theory is one possibility of describing the propagation of seismic body waves. Other methods, e.g., finite-difference (FD), Kelly et al. (1976), or finite-element (FE), Strang and Fix (1973), methods are also widely used. Those methods discretise the medium and the wave equation and thus provide a solution for the wavefield on a grid. All methods have, of course, advantages and disadvantages and are, therefore, used depending on boundary conditions and tasks to be fulfilled. The description of wave propagation by means of FD computations is especially suitable for a heterogeneous medium where the physical parameters vary on a length scale smaller than the dominant wavelength of the propagating signal. This method is very accurate but the memory and computation time requirements are often very large. Ray theory yields good results for inhomogeneous, isotropic and anisotropic, layered, smoothly varying media. The ray theory does not have to overcome problems like grid dispersion and reflections from model boundaries. The constraints with regard to the ray code, i.e., the type of wave, are also more comprehensive. E.g., multiples can easily be suppressed by not taking their ray code into account. The appearance of multiples is inevitable when FD schemes are applied. For a profound study on ray theory, the reader is recommended to refer to Červený (2001) and Popov (1996).

## 2.1 Basics

### 2.1.1 Wave equation

The wave equation is the basis of the mathematical description of wave propagation. It is obtained by inserting Hooke's law into the equation of motion for the continuum. Hooke's law is valid for small deformations and linearly relates the strain in a deformed body to the applied stress. The derivation of the general elastodynamic equation can be found, e.g., in Aki and Richards (1980). For a homogeneous, isotropic, elastic medium it reads in 3-D:

$$\rho \frac{\partial^2 \mathbf{u}(\mathbf{r}, t)}{\partial t^2} = \mathbf{f}(\mathbf{r}, t) + (\lambda + 2\mu) \nabla [\nabla \cdot \mathbf{u}(\mathbf{r}, t)] - \mu \nabla \times [\nabla \times \mathbf{u}(\mathbf{r}, t)]. \quad (2.1)$$

Here,  $\mathbf{u}(\mathbf{r}, t)$  denotes the displacement vector at location  $\mathbf{r}$  and time  $t$ .  $\mathbf{f}(\mathbf{r}, t)$  is the density of the external body force. The density  $\rho$  and the Lamé parameter  $\lambda$  and  $\mu$  determine the physical properties of the medium. In Equation (2.1)  $\nabla = \frac{\partial}{\partial x}\hat{\mathbf{x}} + \frac{\partial}{\partial y}\hat{\mathbf{y}} + \frac{\partial}{\partial z}\hat{\mathbf{z}}$  is the gradient operator and  $\mathbf{r} = (x, y, z)^T$  denotes the global Cartesian coordinates. Hooke's law linearly relates stress and strain whereas the elastodynamic equation relates the spatial variations of the stress tensor with the time variations of the displacement vector  $\mathbf{u}(\mathbf{r}, t)$ . To solve the differential equation (2.1), it can be separated into two wave equations by taking once the divergence and once the curl of that equation. This yields (a) a wave equation for the rotational part of the wavefield and is associated with two shear waves (S-waves) and the shear modulus  $\mu$ . From now on, I focus on (b) the wave equation for the compressional part and I assume that the medium does not show any resistance to shear stress ( $\mu = 0$ ):

$$\nabla[\lambda\nabla \cdot \mathbf{u}(\mathbf{r}, t)] - \rho \frac{\partial^2 \mathbf{u}(\mathbf{r}, t)}{\partial t^2} = \mathbf{f}(\mathbf{r}, t). \quad (2.2)$$

Now, divide Equation (2.2) by  $\rho$ , take the divergence,  $\nabla \cdot$ , and replace the displacement vector  $\mathbf{u}(\mathbf{r}, t)$  by the (scalar) pressure field  $p(\mathbf{r}, t) = -\lambda\nabla \cdot \mathbf{u}(\mathbf{r}, t)$  which yields the so-called *acoustic wave equation*:

$$\nabla \left[ \frac{1}{\rho} \nabla(p(\mathbf{r}, t) + p_0(\mathbf{r}, t)) \right] - \frac{1}{\lambda} \frac{\partial^2 p(\mathbf{r}, t)}{\partial t^2} = 0. \quad (2.3)$$

The applied pressure  $p_0$  represents in Equation (2.3) the pressure distribution equivalent to the force density  $\mathbf{f}(\mathbf{r}, t) = -\nabla p_0(\mathbf{r}, t)$ . Equation (2.3) becomes even more familiar if the density is constant:

$$\nabla [p(\mathbf{r}, t) + p_0(\mathbf{r}, t)] - \frac{1}{c^2} \frac{\partial^2 p(\mathbf{r}, t)}{\partial t^2} = 0, \quad (2.4)$$

where  $c = \sqrt{\frac{\lambda}{\rho}}$  is the propagation velocity of a disturbance. The Lamé parameters and the density depend on the vector  $\mathbf{r}$  if the medium is inhomogeneous.

### 2.1.2 Eikonal and transport equation

The kinematic and dynamic properties of wave propagation can be computed with ray theory using a high-frequency ansatz for the acoustic wave equation. There exists also a high-frequency solution of the elastodynamic wave equation which is not relevant in the context of this thesis. The high-frequency solution requires the material parameters of the medium not to vary greatly over distances of the order of a wavelength  $\lambda$ , i.e., the medium has to be "smooth". The ansatz to find an approximate time-harmonic high-frequency solution of the acoustic wave equation (2.4) is

$$p(\mathbf{r}, t) = A(\mathbf{r})e^{-i\omega(t-\tau(\mathbf{r}))}, \quad (2.5)$$

with  $\omega$  denoting the angular frequency. A general ansatz would be  $p(\mathbf{r}, t) = A(\mathbf{r})w(t - \tau(\mathbf{r}))$ , where  $w(t - \tau(\mathbf{r}))$  denotes an arbitrary function. Inserting Equation (2.5) into expression (2.4) and using the vectorial identity  $\nabla \cdot (\mathbf{a}\mathbf{b}) = \mathbf{b} \cdot \nabla \mathbf{a} + \mathbf{a} \nabla \cdot \mathbf{b}$ , the wave equation (2.4) becomes

$$-\omega^2 A \left[ (\nabla \tau)^2 - \frac{1}{c^2} \right] + i\omega \left[ 2\nabla A \cdot \nabla \tau + A \nabla^2 \tau \right] + \nabla^2 A = 0. \quad (2.6)$$

In Equation (2.6) are three terms with two unknowns. To find a solution for the unknowns  $\tau$  and  $A$ , the last term of the order  $\omega^0$  in Equation (2.6) is negligible compared to the terms of order  $\omega^1$  and  $\omega^2$  for  $\omega \gg 0$ , i.e., for high frequencies. Because of this assumption, the solution will be a high-frequency solution of the acoustic wave equation. The exception to the rule are caustics, cusps and at points where waves are critically reflected and generate head waves. There, ray theory breaks down and the term of order  $\omega^0$  is not negligible anymore. Finally, the first and second term on the left hand side remain to be solved. They yield the *eikonal equation*

$$(\nabla \tau)^2 = \frac{1}{c^2} \quad (2.7)$$

and *transport equation*

$$2\nabla A \cdot \nabla \tau + A\nabla^2 \tau = 0. \quad (2.8)$$

The eikonal equation represents a non-linear partial differential equation of the first order for the travelttime  $\tau(\mathbf{x})$ , which is termed the eikonal. The eikonal equation can be solved with the method of characteristics, Bronstein and Semendjajew (1991), which leads to the so-called *ray tracing system* which is equivalent to a system of six ordinary differential equations:

$$\frac{d\mathbf{r}}{d\tau} = c^2 \mathbf{p} \quad (2.9)$$

$$\frac{d\mathbf{p}}{d\tau} = -\frac{1}{c} \frac{dc}{d\mathbf{r}}, \quad (2.10)$$

where  $\mathbf{p} = (p_1, p_2, p_3)^T$  is the slowness vector and  $|\mathbf{p}| = 1/c$ . Thus, the connection between wave equation and ray theory is established by solving the high-frequency part of the wave equation by the method of characteristics.

The dynamic property of a wave, viz. the amplitude, is determined by the transport equation. It represents a linear partial differential equation of the first order in  $A(\mathbf{r})$ . Using ray coordinates, the solution of the transport equation reads

$$A = \frac{\Psi_0(\gamma_1, \gamma_2)}{\sqrt{\frac{J}{c}}}. \quad (2.11)$$

$\Psi_0$  is the constant of integration only depending on the ray coordinates  $\gamma_1$  and  $\gamma_2$  which represent arbitrary take-off parameters, e.g., two independent components of the slowness vector at the source. The parameter  $J$  is the so-called *ray Jacobian*, i.e., it is a functional determinant:

$$J = \frac{1}{c} \left| \frac{d(x, y, z)}{d(\tau, \gamma_1, \gamma_2)} \right|. \quad (2.12)$$

$\tau$  is the eikonal. For fixed  $\gamma_1$  and  $\gamma_2$ , one special ray is described and the parameter  $\tau$  indicates a position of a point on this ray. More details about the ray Jacobian and its significance in ray theory can be found in Chapter 2.6.

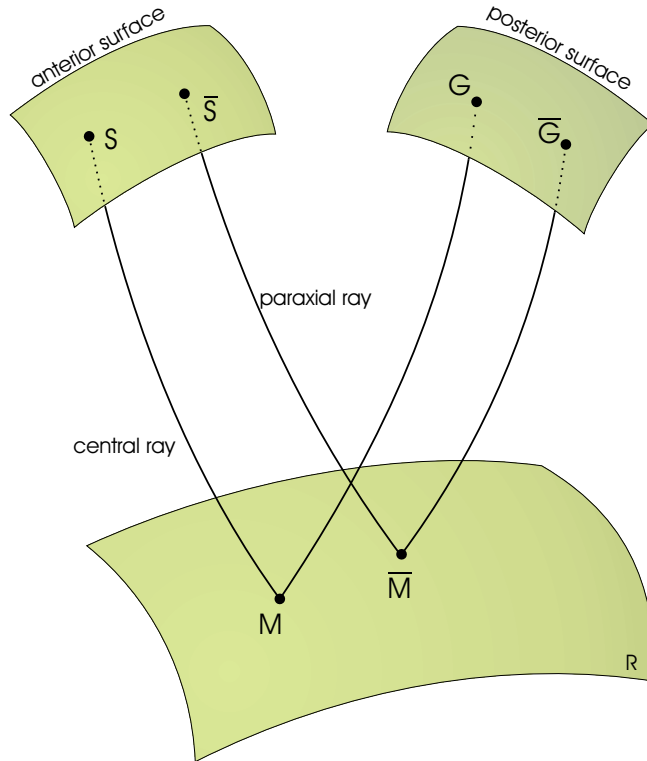


Figure 2.1: Surface-to-surface propagation of a central and paraxial ray.

---

### 2.1.3 2-D wave propagation

For the propagation of waves in two dimensions, e.g., in the  $xz$ -plane, three items have to be considered. (a) the  $y$ -component of the vector  $\mathbf{r}$  remains constant. (b) the application of the  $y$ -component of the gradient operator yields zero as no changes in the  $y$ -direction occur. (c) a point source has to be replaced by a line source with its symmetry axis parallel to the  $y$ -direction. This is required to obtain the correct dynamic properties of the propagating wavefront. In a homogenous medium, the amplitude of a point source is proportional to  $1/R$ , the amplitude of a cylindrical wave is proportional to  $1/\sqrt{R}$ , where  $R$  is the radius of the wavefront.

## 2.2 Paraxial rays and propagator matrix

A ray  $(\overline{SG})$  in the vicinity of the central ray  $(SG)$  can be described by the paraxial ray theory (Bortfeld, 1989; Červený, 2001). Two parameters are needed to describe a paraxial ray: (i) the distance vector  $\mathbf{r}$  to the central ray and (ii) the deviation of the slowness vector  $\mathbf{p}$  from the slowness vector  $\mathbf{p}_0$  of the central ray. Paraxial ray theory means that the values of the parameters at any point of a paraxial ray are linearly dependent on those at its initial point. I use the formulation of Bortfeld (1989) who employs the  $4 \times 4$  *surface-to-surface*

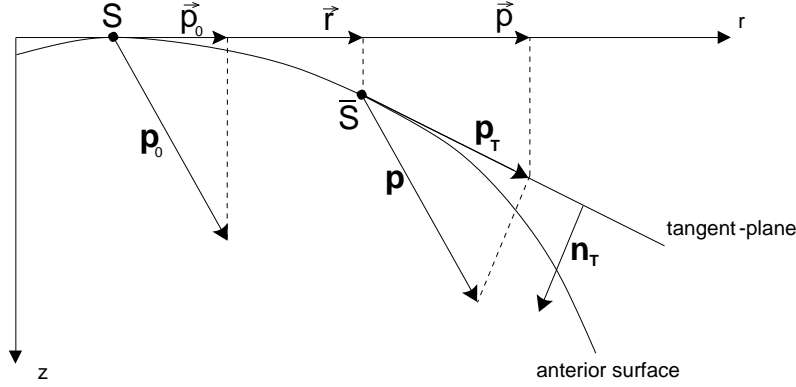


Figure 2.2: Illustration of the cascaded projection, after Bortfeld (1989).

*propagator matrix*  $\underline{\underline{\mathbf{T}}}$  in order to relate the change of the quantities  $\mathbf{p}$  and  $\mathbf{r}$  due to the wavefront propagation from the anterior to the posterior surface. The anterior and posterior surfaces are the surfaces where the ray starts and ends, respectively. Let the vectors  $\mathbf{p}$  and  $\mathbf{r}$  be associated with the anterior surface and the vectors  $\mathbf{p}'$  and  $\mathbf{r}'$  be associated with the posterior surface. In general, the surfaces do not coincide although it is often the case that sources and receivers are placed upon one and the same surface. Figure 2.1 depicts the 3-D finite-offset situation where the anterior and posterior surfaces are separate and the central and paraxial rays are reflected at the surface  $\Sigma_R$ . Bortfeld (1989) projects the three-component vectors  $\mathbf{r}$  ( $\mathbf{r}'$ ) and  $\mathbf{p}$  ( $\mathbf{p}'$ ) onto the anterior (posterior) surface to obtain the two-component vectors  $\vec{r}$  ( $\vec{r}'$ ) and  $\vec{p}$  ( $\vec{p}'$ ). This is illustrated in Figure 2.2, which depicts Bortfeld's idea in the  $xz$ -plane. The two-component vector  $\vec{r} = (x, y)^T$  is obtained by a projection along the  $z$ -axis onto the  $xy$ -plane. The  $z$ -axis is perpendicular to the  $xy$ -plane.  $\bar{S}$  denotes the starting point of a paraxial ray. In order to get the two-component vector  $\vec{p}$ , two cascaded projections are necessary. First, the three-component vector  $\mathbf{p}$  with origin at  $\bar{S}$  has to be projected along its normal onto the plane that is tangent in  $\bar{S}$ , which yields  $\mathbf{p}_T$ . Second,  $\mathbf{p}_T$  is projected onto the  $xy$ -plane, which produces  $\vec{p}$ , see Figure 2.2. Now, I can write down the equation that relates the components of the anterior  $(\vec{r}, \vec{p} - \vec{p}_0)^T$  and posterior  $(\vec{r}', \vec{p}' - \vec{p}'_0)^T$  surfaces of the paraxial rays by a linear relationship:

$$\begin{pmatrix} \vec{r}' \\ \vec{p}' - \vec{p}'_0 \end{pmatrix} = \underline{\underline{\mathbf{T}}}(G, S) \begin{pmatrix} \vec{r} \\ \vec{p} - \vec{p}_0 \end{pmatrix}. \quad (2.13)$$

The first-order approximations of  $\vec{r}'$  and  $\vec{p}' - \vec{p}'_0$  correspond to second-order approximations of the traveltime, i.e., it is in accordance with what is generally called Gaussian optics. The  $4 \times 4$  propagator matrix  $\underline{\underline{\mathbf{T}}}$  is set up by four  $2 \times 2$  submatrices  $\underline{\underline{\mathbf{A}}}$ ,  $\underline{\underline{\mathbf{B}}}$ ,  $\underline{\underline{\mathbf{C}}}$ , and  $\underline{\underline{\mathbf{D}}}$ :

$$\underline{\underline{\mathbf{T}}}(G, S) = \begin{pmatrix} \underline{\underline{\mathbf{A}}} & \underline{\underline{\mathbf{B}}} \\ \underline{\underline{\mathbf{C}}} & \underline{\underline{\mathbf{D}}} \end{pmatrix}. \quad (2.14)$$

Inserting Equation (2.14) into (2.13) yields, for example, that  $\underline{\underline{\mathbf{A}}}$  is the Jacobian matrix  $\partial(x', y')/\partial(x, y)$ , taken at  $\vec{x} = 0$  and  $\vec{p} = \vec{p}_0$ , i.e., at the central ray. Some properties of the

propagator matrix are given in Appendix A.

Another well known propagator matrix is the ray-centred  $\underline{\underline{\Pi}}$  matrix, Červený (2001). The relationship between the  $\underline{\underline{T}}$  and  $\underline{\underline{\Pi}}$  matrix has been published by Hubral et al. (1992a).

### 2.2.1 Rays in 2-D

The paraxial ray theory in two dimensions is described by the distance vector  $\vec{r} = (x, z)^T$  and the slowness vector  $\vec{p} = (p, q)^T$  at the anterior surface. Similarly,  $\vec{r}' = (x', z')^T$  and  $\vec{p}' = (p', q')^T$  describe paraxial ray theory at the posterior surface. The projection of them onto the anterior (posterior)  $x(x')$ -axis reduces them to scalars  $x(x')$  and  $p(p')$ . As a consequence, the  $4 \times 4$  propagator matrix  $\underline{\underline{T}}$  becomes a  $2 \times 2$  matrix  $\underline{\underline{T}}$ . The  $2 \times 2$  submatrices  $\underline{\underline{A}}$ ,  $\underline{\underline{B}}$ ,  $\underline{\underline{C}}$ , and  $\underline{\underline{D}}$  become  $1 \times 1$  matrices, i.e., scalars  $A$ ,  $B$ ,  $C$ , and  $D$ . In the following, I call these scalars *elements* as they are elements of the  $2 \times 2$  propagator matrix  $\underline{\underline{T}}$ .

## 2.3 Paraxial traveltimes

As mentioned in the introduction, from now on I am using all equations for the 2-D case. When I refer to previous equations of this chapter, I apply the 2-D version of that formula.

The Common-Reflection-Surface (CRS) stack, Chapter 3, makes use of the parabolic or hyperbolic traveltime approximation, respectively, for paraxial rays. Bortfeld (1989) derived the parabolic traveltime approximation for a so-called seismic system (arbitrary number of homogeneous, isotropic layers) using Hamilton's equation for transmitted rays from the initial surface to the final surface

$$dt = p' dx' - p dx. \quad (2.15)$$

The traveltime difference of the central ray and a corresponding paraxial ray is denoted by  $dt$ . Next, I have to solve Equation (2.13) for  $p$  and  $p'$ , which yields

$$p = p_0 + B^{-1}x' - B^{-1}Ax \quad (2.16)$$

$$p' = p'_0 + Cx + DB^{-1}x' - DB^{-1}Ax. \quad (2.17)$$

Inserting Equations (2.16) and (2.17) into Equation (2.15) and a subsequent integration gives the traveltime formula for paraxial rays, Bortfeld (1989):

$$\begin{aligned} t_{par}(x, x') &= t_0(x_0, x'_0) - p_0x + p'_0x' - xB^{-1}x' \\ &+ \frac{1}{2}x^2B^{-1}A + \frac{1}{2}x'^2DB^{-1}. \end{aligned} \quad (2.18)$$

Hubral et al. (1992a) showed that Equation (2.18) also holds for a seismic system that consists of laterally inhomogeneous layers. Because of the parabolic form Equation (2.18) is called *parabolic traveltime*. For many years it has been known that for a simple layered medium and near vertical reflections, a hyperbolic traveltime approximation is better than a parabolic traveltime approximation, see e.g. Ursin (1982). Therefore, Schleicher

et al. (1993) squared Equation (2.18) and retained only second-order terms in  $x$  and  $x'$  to obtain the hyperbolic equivalent

$$\begin{aligned} t_{hyp}^2(x, x') &= [t_0(x_0, x'_0) - p_0x + p'_0x']^2 \\ &+ t_0(x_0, x'_0) \left( -2xB^{-1}x' + x^2B^{-1}A + x'^2DB^{-1} \right). \end{aligned} \quad (2.19)$$

## 2.4 Fresnel zone

The (first) Fresnel zone plays an important role in imaging. The 2-D Fresnel zone is defined as a slice of the 3-D Fresnel volume perpendicular to the central ray. Only if the central ray is normal to a plane interface, the interface Fresnel zone coincides with the Fresnel zone defined in the previous sentence. In general the Fresnel zone is not circular but has an elliptic shape. The size of the first Fresnel zone is often used as a measure of lateral resolution that depends on the frequency, the velocity of the medium, and on the traveltime. From now on, I am omitting the word "first" if no ambiguities arise, as I will only consider the first Fresnel zone throughout this thesis. In 2-D, the term Fresnel zone is not correct as there exists no extension into the  $y$ -direction (perpendicular to the  $xz$ -plane), see Figure 2.3. Something like "width of the Fresnel line" could be an appropriate description for 2-D but it seems to be rather far-fetched. Thus, I stick to the term "Fresnel zone" also in 2-D.

I use the Fresnel zone to define the local minimum aperture for the CRS stack, Chapter 3, and for my parsimonious migration, Chapter 4.2. Correctly speaking, I do not use the Fresnel zone but the so-called projected Fresnel zone, (Hubral et al., 1993b; Schleicher et al., 1997) as a minimum aperture. The projection of the Fresnel zone along the normal ray up to the acquisition line results in the minimum aperture. A detailed description is given in Section 2.5.

As a result of numerous experiments, it is known that the wavefield at a receiver is affected by the structure in some vicinity of the central ray. Therefore, the ray is no longer considered as a mathematical ray, but can be interpreted as the trajectory along which the high-frequency part of the energy of the seismic wave under consideration propagates from the source to the receiver, Červený (2001). E.g., in Born and Wolf (1987) it is shown that the total disturbance at a receiver equals half the disturbance due to the first Fresnel zone. This emphasises the importance of the first Fresnel zone.

The extension of the Fresnel zone at the target reflector is limited by a traveltime difference that equals half the period,  $T/2$ , of a mono-frequent wave. The traveltime difference is given by the different paths of the reflected ray ( $SM_RG$ ) and the diffracted rays ( $S\overline{M}_1G$ ) and ( $S\overline{M}_2G$ ) and their associated traveltimes. In Figure 2.3, the point  $M_R$  is a specular reflection point whereas the points  $\overline{M}_1$  and  $\overline{M}_2$  are diffraction points.

The subsurface points are denoted by the 2-D Cartesian coordinates  $x$  and  $z$ . A point in the time domain is determined by the two-way traveltime  $t$  and the acquisition coordi-

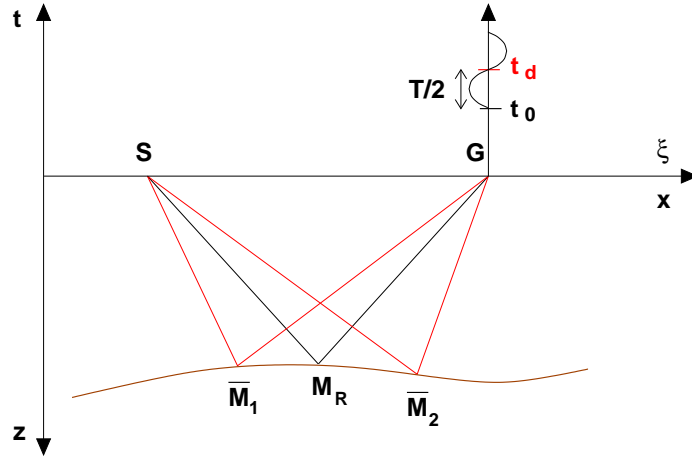


Figure 2.3: The difference of the traveltime  $t_0$  of the reflected ray ( $SM_RG$ ) and the travel-time  $t_d$  of the two diffracted rays ( $S\bar{M}_1G$ ) and ( $S\bar{M}_2G$ ) define the (first) Fresnel zone.

nate  $\xi$ . The case where source and receiver are separated, i.e., the offset case, as in Figure 2.3, is better suited for illustration than the ZO case, which I am actually interested in. The equation

$$|t(S, G) - t(S, \bar{M}) - t(\bar{M}, G)| \leq \frac{T}{2} \quad (2.20)$$

defines the size of the Fresnel zone for the 2-D case on the reflector ( $\bar{M}$  is either  $\bar{M}_1$  or  $\bar{M}_2$ ). This is the definition proposed by Kravtsov and Orlov (1980). Equation (2.20) is the definition of the size of the Fresnel zone for the mono-frequent case. Later in the synthetic and, of course, in the real examples, the propagating wave is not mono-frequent but is a transient signal with a certain frequency bandwidth. Thus, the width of the Fresnel zone is determined by the length,  $T_W$ , of the wavelet. This time-domain definition corresponds with the one used by Knapp (1991) who examined the Fresnel zone associated with broadband data.

The aim is now to express the Fresnel zone in terms of elements of the surface-to-surface propagator matrix because those elements can be determined by means of traveltimes at the surface. I start with the assumption that the source and the receiver have a certain offset. The parabolic traveltime approximations for the down-going  $t(S, \bar{M})$  and up-going  $t(\bar{M}, G)$  paraxial ray in Figure 2.3 then read in 2-D:

$$t(S, \bar{M}) = t(S, M_R) + p_{M_R} x_{\bar{M}} + \frac{1}{2} x_{\bar{M}}^2 D_1 B_1^{-1} \quad (2.21)$$

$$t(\bar{M}, G) = t(M_R, G) - p_{M_R} x_{\bar{M}} + \frac{1}{2} x_{\bar{M}}^2 B_2^{-1} A_2. \quad (2.22)$$

$x_{\bar{M}}$  denotes the 1-D coordinate of the normal projection of  $\bar{M}$  onto the line that is tangent in  $M_R$ .  $M_R$  also denotes the origin for the coordinates along this tangent line. The

slowness coordinate  $p_{M_R}$  is the projection of the 2-D slowness vector  $\vec{p}_{M_R}$  at  $M_R$  onto the tangent line. The indices at the propagator elements are due to the decomposition of the total ray. Hubral et al. (1992b) showed, actually in 3-D, that the propagator matrix  $\mathbf{T}$  can be decomposed into two propagator matrices that correspond to the up-going and down-going ray

$$\mathbf{T} = \mathbf{T}_2 \mathbf{T}_1 . \quad (2.23)$$

This equation is the *chain rule*. The index 1 denotes the down-going and the index 2 the up-going ray. Next, I insert Equations (2.21, 2.22) into Equation (2.20) which yields

$$|x_M^2 H| \leq T , \quad (2.24)$$

where  $H$  is the Fresnel zone element, Hubral et al. (1992b):

$$H = D_1 B_1^{-1} + B_2^{-1} A_2 . \quad (2.25)$$

The Fresnel zone, defined by Equation (2.24), might differ slightly from the exact one defined by Equation (2.20). This is due to the paraxial approximation. The Fresnel zone element  $H$  reduces to

$$H = 2D_1 B_1^{-1} = 2B_2^{-1} A_2 = 2D_0 B_0^{-1} , \quad (2.26)$$

which can be derived by using the symplecticity property and the equation for the ZO reverse ray as described in Appendix A. Thus, for ZO, the Fresnel zone element can be expressed by a single one-way propagator matrix  $\mathbf{T}_0$  with the elements  $A_0$ ,  $B_0$ ,  $C_0$ , and  $D_0$ .

## 2.5 Projected Fresnel zone

The seismic data that contain the information about the subsurface are acquired at the earth's surface, except for vertical seismic profiling which is performed in boreholes. In order to reconstruct the geometry and the change in impedance of the subsurface, i.e., to image the subsurface, the measured data that correspond to one diffraction point in the subsurface have to be summed up (stacked). This is demanded by Kirchhoff theory (Schneider, 1978; Born and Wolf, 1987), see Chapter 4 for more details. To yield an image without any loss, the Kirchhoff-migration integral (4.4) would extend from  $-\infty$  to  $+\infty$  with the assumption that no noise is present. All seismic data measured in the field include noise, viz. signals that do not represent the structure of the earth. Sources that produce noise are, e.g., wind, traffic, power lines etc. The image quality does not improve if the size of the aperture, which determines the integral boundaries, is larger than the so-called projected Fresnel zone. This has been shown by Schleicher et al. (1997) and Sun (1998), see also Subsection 4.1.2.

The projection of the interface Fresnel zone up to the acquisition line, which coincides with the  $\xi$ -axis, is shown in Figure 2.4. The interface Fresnel zone at depth is illustrated by a bold arc at  $M_R$ . The upper half of Figure 2.4a shows the time-domain. The dotted

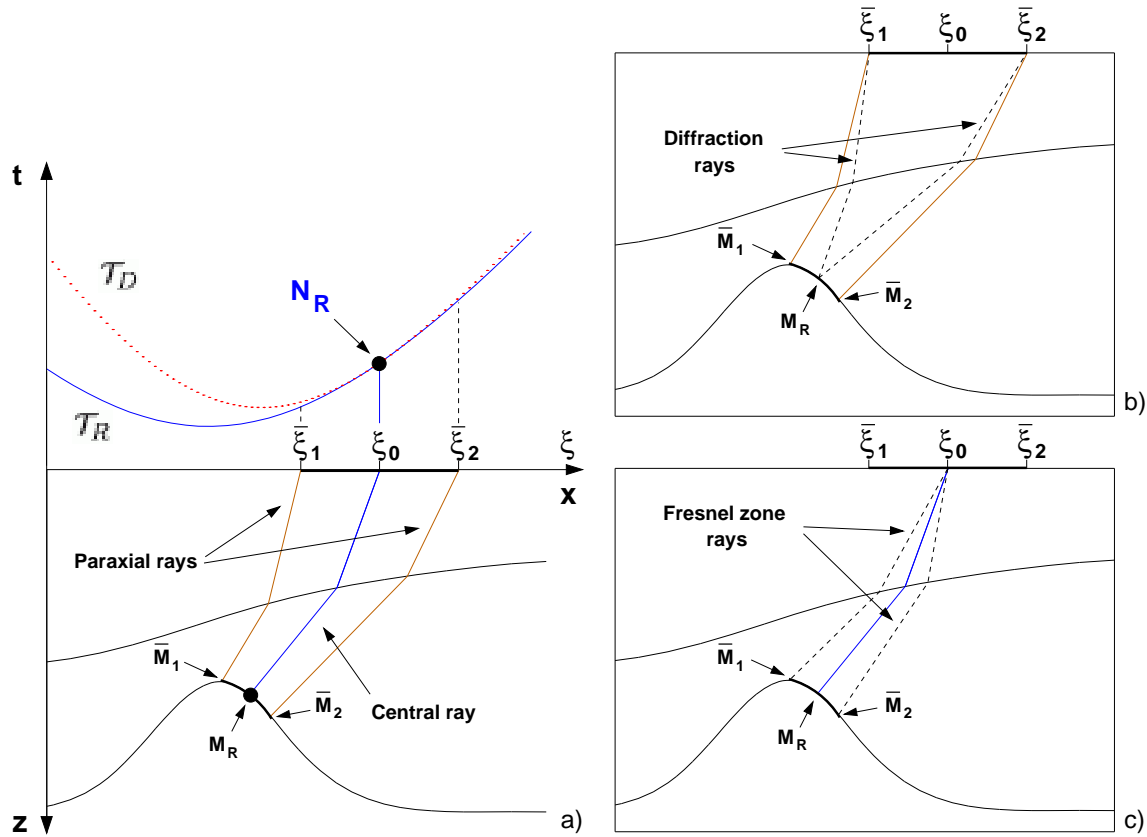


Figure 2.4: Duality points  $M_R$  and  $N_R$  are centre points of the projected and interface Fresnel zone (bold drawn), respectively.

curve, labelled  $T_D$ , is the diffraction traveltime curve, that corresponds to the depth point  $M_R(x, z)$ , i.e., it is regarded as a diffraction point. The solid curve, labelled  $T_R$ , is the primary ZO reflection traveltime curve associated with the second reflector. The point  $N_R(\xi, t)$  is a stationary point, which means that the reflection and diffraction traveltime curves are tangent at this point. The outstanding feature of the stationary point is described in Section 4.1.2. The points  $N_R$  and  $M_R$  are so-called *duality points*, Tygel et al. (1995). The depth point  $M_R$  is related to the time-domain point  $N_R$  via the normal ray that emerges at its  $\xi$ -coordinate,  $\xi_0$ .  $M_R$  is the centre point of the Fresnel zone at depth and  $\xi_0$  is the corresponding centre point of the projected Fresnel zone at the acquisition line.

The projected Fresnel zone, Hubral et al. (1993b), is defined by the upper endpoints of the bundle of normal, paraxial rays (brown lines in Figure 2.4) that leave the considered reflector perpendicularly within the interface Fresnel zone. In Figure 2.4, the projected Fresnel zone is indicated by a bold line, centred at  $\xi_0$ . Figure 2.4b shows the primary zero-offset (ZO) paraxial reflection rays  $(\xi_i \bar{M}_i \xi_i)$ , where  $i = 1, 2$ , and the correspond-

ing diffraction rays ( $\overline{\xi_i M_R \xi_i}$ ). Zero-offset means that source and receiver are coincident. If the difference of the traveltimes pertaining to the reflected and diffracted ray equals  $T/2$ , the boundary of the projected Fresnel zone is obtained.  $T$  is the period of a mono-frequent wave. The definition of the first interface Fresnel zone is illustrated by Figure 2.4c. A point  $\overline{M}_i$  belongs to it if and only if the traveltime difference of the ZO central ray ( $\xi_0 M_R \xi_0$ ) and a Fresnel zone ray ( $\xi_0 \overline{M}_i \xi_0$ ) is less than or equal to  $T/2$ . The Fresnel zone ray is in accordance with the description of Červený and Soares (1992) of rays within a Fresnel volume, see Figure 3.5. The definition of the projected Fresnel zone of Hubral et al. (1993b) is for ZO in accordance with the definitions illustrated by Figure 2.4b. For simplicity, the index  $i$  that is related to the paraxial rays is dropped from now on.

Now, I describe mathematically how to project the interface Fresnel zone around  $M_R$  in Figure 2.4 up to the acquisition line. As I consider a measurement line instead of a surface, the following equations can be reduced to scalars. Although a projection always needs vectors, the second component of the 2-D vector is set to zero due to Bortfeld's definition. The vector  $x_{\overline{M}}$  with its origin at  $M_R$  is obtained in the same way as described before. It is the normal projection of the vector onto a straight line. The vector has its origin at  $M_R$  and determines the actual point  $\overline{M}$  on the curved element. This line is tangent to the reflector at  $M_R$ . The next step is the projection of the Fresnel zone from the tangent along paraxial rays up to the measurement line, i.e., onto the  $\xi$ -axis. In terms of the corresponding scalars and as a first order approximation it can be expressed by

$$\xi = P x_{\overline{M}}. \quad (2.27)$$

The projection  $P$  has to be determined. Here, I follow the line of Hubral et al. (1993b). Inserting Equation (2.27) into Equation (2.24) yields the projected Fresnel zone for zero-offset:

$$|\xi^2 H_P| \leq T, \quad (2.28)$$

where  $H_P$  is given by

$$H_P = P^{-2} H. \quad (2.29)$$

$H_P$  is the so-called projected Fresnel zone element. Solving the system of equations for a paraxial normal ray by applying the one-way ray propagator matrix  $\underline{\mathbf{T}}_0$  yields

$$x_{\overline{M}} = (A_0 - B_0 D_0^{-1} C_0) \xi = D_0^{-1} \xi. \quad (2.30)$$

The symplecticity, see Appendix A.2, has been applied to obtain the right-hand side of Equation (2.30). Comparing Equations (2.27) and (2.30) yields  $P = D_0$ . Hence,

$$H_P = D_0^{-2} H = 2 D_0 B_0^{-1}, \quad (2.31)$$

where Equation (2.26) has been inserted to get the right-hand side. Finally, a simple expression for the projected Fresnel zone is obtained if Equation (2.31) is compared with Equation (A.2) and (A.9b) of Appendix A:

$$H_P = 4 B^{-1}. \quad (2.32)$$

Hubral et al. (1993b) showed that the propagator matrix element  $B$  can be obtained by taking the second order derivatives of the difference of two identified traveltime functions that correspond to the same event. One traveltime function is identified in the common-midpoint (CMP) section, the other in the ZO section. Obviously, and this is the particular importance, no knowledge about the reflector overburden is required to get the Fresnel projection element. In Chapter 3, I describe a model-independent stacking method which generates as a by-product attributes that are related to the propagator matrix element  $B$ .

In Figure 2.4, the projected Fresnel zone is bounded by the paraxial ray at  $\bar{\xi}$ , where the traveltime difference of the reflection traveltime  $t(\bar{\xi} \bar{M} \bar{\xi})$  and the diffraction traveltime  $t(\bar{\xi} M_R \bar{\xi})$  is equivalent to  $T/2$  or  $T_W$ , respectively. The boundary of the projected Fresnel zone can now be expressed due to paraxial ray theory in 2-D by

$$|4B^{-1}(\bar{\xi} - \xi_0)^2| \leq T. \quad (2.33)$$

Here,  $(\bar{\xi} - \xi_0)$  is the distance between the central ray and a paraxial ray on the midpoint axis.

## 2.6 Geometrical spreading

Suppose, e.g., a point source is excited, the spherically emitted wavefront propagates through a homogeneous medium and no intrinsic damping occurs. Then, in 3-D the *spherical divergence* makes the amplitude of the wave change inverse proportional to the radius of the curvature of the propagating wavefront. In other words, as a consequence of the law of conservation, the energy density changes such that the surface integral of the considered wavefront is constant. For a more general medium like an inhomogeneous layered medium where the wavefront is no sphere anymore, the term *geometrical spreading* (GS) is used instead of spherical divergence. The GS has a major impact on the change in amplitude if transmission losses are negligible. If the GS is applied to, e.g., a zero-offset section, the section would display the correct reflection coefficient for a seismic event if the source strength is known. Such a true-amplitude (TA) section is of great support for geological interpretation, e.g., to find a hydrocarbon deposit. In 2-D, the amplitude is inverse proportional to the square root of the curvature of the propagating wavefront. Because of its importance, there exists a great number of publications with respect to geometrical spreading. Here, I list some in my opinion important publications: Newman (1973), Popov and Pšenčík (1978), Ursin (1982), Hubral (1983), Bleistein (1986), Červený (2001).

### 2.6.1 Geometrical spreading in 2-D

The following considerations are valid for an inhomogeneous isotropic 2-D medium. The geometrical spreading can be determined by examining the density of the ray field which in turn can be expressed by the curve that connects a central ray and a paraxial ray, see Figure 2.5. This I call an *elementary ray section* or simply *ray section*. The ray section

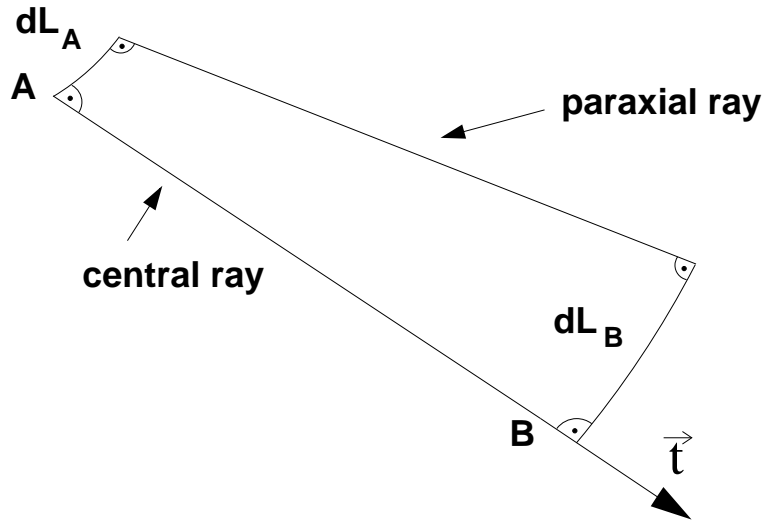


Figure 2.5: The differential curves,  $dL_A$  and  $dL_B$ , of the ray section are perpendicular to the rays.

encompasses the family of rays within the limits  $(\gamma; \gamma + d\gamma)$ , where  $\gamma$  is the ray coordinate of the central ray. As indicated in Figure 2.5, the lateral boundaries are formed by rays, whereas the front and back of the ray section is bounded by a wavefront at two different time steps. It is assumed that the energy flows within the ray section.

The ray Jacobian,  $J$ , which appears in the expression of the solution of the transport equation (2.11), is directly related to the geometrical spreading. The ray Jacobian (2.12) reduces now to

$$J = \frac{1}{c} \left| \frac{d(x, z)}{d(\gamma, \tau)} \right|. \quad (2.34)$$

The Jacobian,  $J$ , is the Jacobian of the transformation of the ray coordinates  $\gamma$  and  $\tau$  to general Cartesian coordinates  $\vec{x} = (x, z)^T$ . The ray coordinate  $\tau$  denotes the eikonal but it would also be possible to use the arc length of the ray  $s$ . Note that the unit tangent vector to the ray at  $\vec{x}(\tau)$  is defined as  $\vec{t} = d\vec{x}/d\tau$ . In an inhomogeneous isotropic medium the wavefront is always perpendicular to the rays, i.e., perpendicular to  $\vec{t}$ . The Jacobian (2.34) represents the front of the ray section normalised with respect to  $d\gamma$ . The quantity  $J$  vanishes when the curvature of the considered wavefront increases to infinity. Such points are called *caustic points*. The geometrical spreading is related to the ray Jacobian by

$$L = |J|^{\frac{1}{2}}, \quad (2.35)$$

where  $L$  is the so-called geometrical spreading factor (GSF). Let, for instance, the differential line  $dL_A$  of Figure 2.5 be a part of a wavefront where energy initially flows through. For high frequencies the same energy is subsequently distributed over a different, here

greater, differential line  $dL_B$ . Therefore, the intensity,  $I_B$ , decreases compared to  $I_A$  and the relationship of the areas and intensities can be expressed by the following equation:

$$I_A dL_A = I_B dL_B . \quad (2.36)$$

As the amplitudes are proportional to the square root of intensities, the geometrical spreading factor for point  $B$  is defined as

$$L_B = \left( \frac{dL_B}{dL_A} \right)^{1/2} . \quad (2.37)$$

For a homogeneous medium the geometrical spreading reduces to spherical spreading, i.e.,  $L = \sqrt{R} = \sqrt{v_0 t_0}$ , which has been normalised by a unit radius.  $R$  is the radius of the wavefront curvature,  $v_0$  the velocity of the homogeneous medium, and  $t_0$  is the source-receiver traveltimes. This is valid for wavefronts reflected on a planar horizontal/dipping interface. Newman (1973) showed that the GSF for a reflection from the  $N$ -th layer in a model with homogeneous horizontal layers yields:

$$L = \frac{\sum_{i=1}^N t_i v_i^2}{v_0} = t_0 \frac{v_{RMS}^2}{v_0} . \quad (2.38)$$

Take the square root of (2.38) and it is valid for 2-D. The traveltimes  $t_0 = \sum_{i=1}^N t_i$  is the vertical two-way traveltimes and  $v_{RMS}$  is the well known root-mean-square (RMS) velocity. Now, I introduce the *normalised geometrical spreading*, where  $Q_2$  is an element of the propagator matrix  $\underline{\Pi}$ :

$$L = \frac{1}{\sqrt{v_G v_S}} |Q_2|^{\frac{1}{2}} e^{-i\frac{\pi}{2}\kappa} . \quad (2.39)$$

Here, the definition of the square root of the ray Jacobian has been taken into account. The phase shift is given due to the number of caustics counted along the ray from the source,  $S$ , to the receiver,  $G$ .  $\kappa$  is the so-called KMAH index, see Červený (2001). The relationship of the submatrices of  $\underline{\Pi}$  and  $\underline{\mathbf{T}}$ , described in Hubral et al. (1992a), leads to

$$L = \frac{\sqrt{\cos \alpha_G \cos \alpha_S}}{\sqrt{v_G v_S}} |B|^{\frac{1}{2}} e^{-i\frac{\pi}{2}\kappa} . \quad (2.40)$$

For the ZO case the emergence angles  $\alpha_G$  and  $\alpha_S$  as well as the velocities  $v_G$  and  $v_S$  of the first layer are identical, hence

$$L = \frac{\cos \alpha}{v_0} |B|^{\frac{1}{2}} e^{-i\frac{\pi}{2}\kappa} . \quad (2.41)$$

A nice and comprehensive derivation of the 3-D version of Equation (2.40) can be found in Schleicher (1993).

### 2.6.2 Geometrical spreading in 2.5-D

In seismics the term “2.5-D” is defined by taking into account 3-D wave propagation in a 3-D laterally inhomogeneous earth. The parameters of the medium are not supposed to vary in the out-of-plane  $y$ -direction. The geometrical spreading for 2.5-D wave propagation can be decomposed into an *in-plane* and *out-of-plane* component (Bleistein, 1986). The 3-D point-source geometrical spreading factor in the 2.5-D model is expressed for ZO in accordance to Tygel et al. (1998)

$$L_3 = L_2 \sqrt{\sigma}. \quad (2.42)$$

$L_2$  denotes the in-plane, whereas  $\sqrt{\sigma}$  denotes the out-of-plane component of the 3-D geometrical spreading. The in-plane factor is identical to the 2-D (line-source) GSF (2.41). From now on, I will not consider the phase of the geometrical spreading because the method described in the next chapter is not able to supply it. Nonetheless, if the signal is recovered correctly it is at least possible to recognise whether the number of caustics the ray has gone through is even or odd. If the number is even and provided the reflection coefficient is positive, the shape of the wavelet is identical with the source wavelet, otherwise the wavelet has got the shape of its Hilbert transform. For more details see Hubral et al. (1993a). Please note the relationship of the in-line geometrical spreading and the projected Fresnel zone:

$$L_2 \propto H_p^{-1/2}. \quad (2.43)$$

Sun (1996) investigated the relationship between the Fresnel zone and the geometrical spreading in 3-D in detail.

The out-of-plane geometrical spreading  $\sqrt{\sigma}$  is given by

$$\sigma = \int v(s) ds = \int v^2(t) dt. \quad (2.44)$$

Here,  $s$  is the arc length and  $t$  is the traveltime along the normal ray. A comparison of Equation (2.44) with Equation (2.38) shows that for a horizontally layered medium  $\sqrt{\sigma} = v_{RMS} \sqrt{t_0}$ . In Section 3.2.4 it is described how the in-plane and the out-of-plane geometrical spreading is computed for an arbitrarily curved inhomogeneous medium.



## Chapter 3

# Common-Reflection-Surface Stack

The Common-Reflection-Surface (CRS) Stack (Hubral et al., 1999; Mann et al., 1999; Jäger et al., 2001) is a macro model independent stacking method to simulate a zero-offset section. It is most desirable to work with a model independent stacking method because deviations from the real subsurface are obviously causally related to wrong assumptions and are thus eliminated by not taking them into account. “Data-driven stacking method” might be a more appropriate terminology because it emphasises that the results depend on the data which in turn have to depend on the subsurface. It is important to realise that no initial model serves as a basis for the simulation of the ZO section. Here, I stick to the term “model independent”. In order to generate a CRS stack, three attributes have to be found, viz., one emergence angle and two radii of wavefront curvatures. These attributes are related to characteristic properties of wave propagation. I will focus on the *normal moveout* (NMO) velocity, the projected Fresnel zone and the geometrical spreading factor. As well as the CRS Stack, other model independent stacking methods exist. A comprehensive overview is given by the publications in the special issue of the Journal of Applied Geophysics (Hubral, 1999).

The basics of the CRS Stack are shortly reviewed in the following section. Afterwards, the relationship of the attributes and the listed wavefield properties are derived and the improvements that have been achieved by applying them is presented by a real example in this chapter and by a synthetic example in the next chapter.

### 3.1 Basics

#### 3.1.1 Conventional stacking

In order to obtain an image of the subsurface, a multi-coverage data set is acquired. In off-shore seismics, i.e., marine seismics, it means that a vessel tows arrays of receivers, called streamers, while periodically acoustic sources, called air guns, are fired. The effect is that the same region in the subsurface is multiply illuminated. For a horizontally layered earth the effect can be easily illustrated. In Figure 3.1 a common-shot (CS) and a common-midpoint (CMP) configuration is depicted. While the CS configuration illuminates a region of an interface the CMP configuration multiply illuminates a point of the

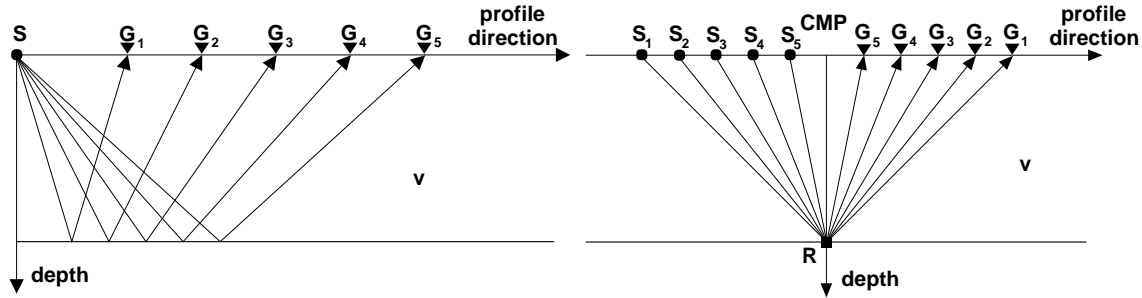


Figure 3.1: Common-shot and common-midpoint configuration.

reflector. Strictly speaking, the region of influence is not a point but mainly the first Fresnel zone as described in Section 2.4. In reality, the data always contain noise due to wind, traffic etc. The signal-to-noise (S/N) ratio can be increased if the data that illuminated the same point (the same first Fresnel zone) are summed, i.e., stacked. The improvement of the S/N ratio gained by stacking is theoretically  $\sqrt{N}$  (Yilmaz, 1987) with the assumption that the signal on the traces of the CMP gather is identical and the random noise is mutually uncorrelated from trace to trace.

Here, I outline the simulation of a ZO section for a simple model as sketched in Figure 3.1. The intention is, of showing how the conventional processing works in principle. During the parameter search (Subsection 3.1.5), the CRS Stack uses to some extent the conventional method.

For processing, the data of many common-shot experiments are resorted into CMP gathers with midpoint coordinate  $\xi = (\xi_G + \xi_S)/2$  and half-offset coordinate  $h = (\xi_G - \xi_S)/2$ , where  $\xi_S$  and  $\xi_G$  denote the source and receiver coordinates. In the next step, a velocity analysis is performed on selected CMP gathers. The parameters  $t_0$  and  $v_{NMO}$  of the traveltime curve, that is best aligned to the data, are used for stacking.  $t_0$  is the reflection traveltime for ZO and  $v_{NMO}$  is the NMO velocity. For a single horizontal interface and a CMP configuration the traveltime curve is a hyperbola:

$$t^2(h) = t_0^2 + \frac{4h^2}{v_{NMO}^2}, \quad (3.1)$$

The moveout of the hyperbola can be compensated with a correct NMO velocity, thus the reflection event is flattened and can be horizontally summed. The stacking result is placed into the ZO trace. If the reflector is inclined, the rays of a CMP configuration are not reflected at the same point anymore. This reflection point dispersal is corrected by a *dip moveout* (DMO) correction, Deregowski (1986) and Hale (1991).

More details on sophisticated velocity analysis are presented by Yilmaz (1987) and the derivation of traveltime formulae for models with arbitrary plane layers or curved interfaces are described, e.g., in Hubral and Krey (1980).

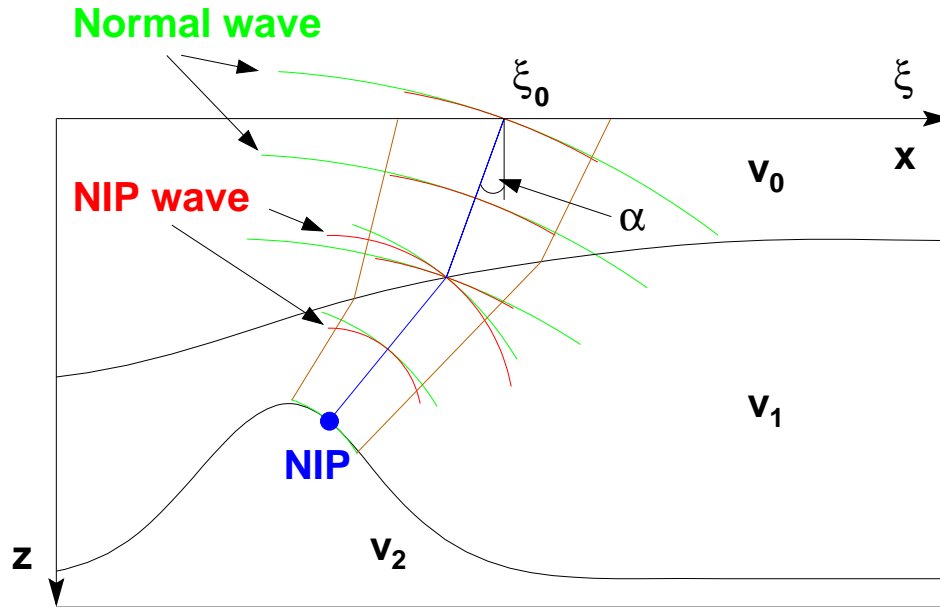


Figure 3.2: Illustration of the two eigenwaves, viz., the NIP-wave and normal wave.

### 3.1.2 Eigenwaves

The CRS Stack is based on paraxial ray theory which has been summarised in Section 2.2. To obtain the traveltimes for a 2-D inhomogeneous model with arbitrarily curved interfaces, two theoretical experiments are performed, which yield two different so-called *eigenwaves*, Hubral (1983). In principle, these eigenwaves are associated with an exploding diffractor, denoted *NIP* in Figure 3.2, which produces the NIP-wave with radius  $R_{NIP}$  at the surface and an exploding reflector which yields the normal-wave (N-wave) with radius  $R_N$  at the surface. Here, NIP stands for normal incidence point, i.e., the endpoint at depth of the central ray that is normal to the considered reflector (blue ray in Figure 3.2). The central ray is refracted at the interfaces due to Snell's law, whereas the wavefront curvatures of the NIP- and N-wave change due to the *refraction* and *transmission law of curvature*, Hubral and Krey (1980). The exploding reflector is locally approximated by an arc segment around *NIP* and is shown in green in Figure 3.2. The NIP- and N-wave are eigenwaves because a wave that originates with the radius of curvature  $R_S = \pm(R_{NIP}R_N)^{1/2}$  emerges with an identical radius of curvature at the receiver  $R_G = R_S$ . The reason for this identity is that the waves are eigenvalues of the propagator matrix  $\underline{T}$  for a normal ray.

### 3.1.3 CRS traveltimes

Schleicher et al. (1993) followed Ursin (1982) in order to express the parabolic and hyperbolic paraxial traveltimes Equations (2.18) and (2.19) in terms of midpoint and half-offset coordinates. Then Tygel et al. (1997) combined that result with the formulation of the



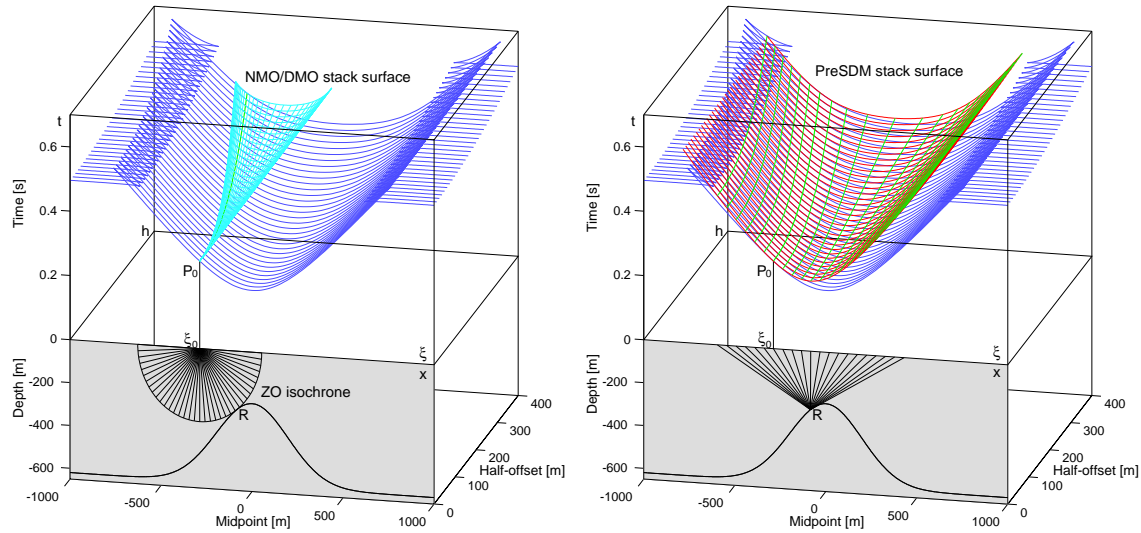


Figure 3.4: The fan-shaped NMO/DMO operator is the reflection response of the circular reflector with the shape of the ZO isochrone. The red Huygens' surface in the time domain is the multi-coverage data set of the point diffractor at  $R$ .

with constant layer velocity as displayed in the lower part of Figure 3.3. The traveltime surface is embedded in the midpoint–half-offset–time ( $\xi$ - $h$ - $t$ ) domain. The red circular element has got the same curvature at  $R$  as the interface. All the rays shown are normal to this element and the traveltimes associated with these rays lie on the green traveltime curve at zero-offset which is the curve at the very front. The traveltimes that correspond to one and the same reflection point  $R$  for rays with a finite-offset, describe a common-reflection-point (CRP) trajectory which is emphasised by the bold green curve in Figure 3.3. The complete green surface, which is built up of CRP trajectories for each point on the red circular element, is the CRS operator in time. The green surface is the stacking surface to simulate the zero-offset point  $P_0$ .

### 3.1.4 Comparison of traveltime equations

Müller (1999) and Jäger (1999) compared the traveltime Equations (3.2), (3.3), and three variations of the *multifocus formula*, (Gelchinsky et al., 1997; Tygel et al., 1997), which is also a model independent stacking method. They showed that the hyperbolic CRS Stack traveltime formula is the most robust and has got the best balance between accuracy and computational cost.

The advantage of the CRS Stack becomes obvious in comparison with conventional stacking methods. Therefore, I will compare the summation operators of the NMO/DMO process and of the prestack depth migration (PreSDM) process with the CRS stacking operator. The cyan, fan-shaped stack surface, Figure 3.4, obviously takes a much smaller part of the multi-coverage dataset into account than the CRS does. The cyan stack sur-

face can be regarded as the primary reflection response for a reflector that is, with respect to geometry, identical to the circular ZO isochrone and tangent to the actual reflector in  $R$ . Hence, the NMO/DMO stack can be looked upon as the envelope of zero-offset isochrones. In contrast to this, the CRS can be regarded as the envelope of arc segments which possess locally at  $R$  the same curvature as the reflector. The fan-shaped surface is tangent to the blue traveltime surface along the green CRP trajectory that is associated with the NIP  $R$ .

The other well-known conventional stacking surface belongs to the prestack depth migration (PreSDM) which is displayed in red in Figure 3.4. Again, the summation surface is tangent to the blue surface along the green CRP trajectory but now, it is assumed that the reflector is build up by diffractors which is in agreement with Huygens' principle. Therefore, the PreSDM operator is a collection of Huygens' traveltime curves, which are in general described by a double square root expression and for ZO by hyperbolas for a reflector with a homogeneous overburden. For a time migration, the stacking result would be assigned to the apex of the red ZO traveltime curve. Compared to the PreSDM, the CRS Stack operator better matches the blue surface.

The NMO/DMO operator and the PreSDM operator are special cases of the CRS operator. This can be understood if one conceives the red arc in Figure 3.3 to be a mirror which changes its shape such that it coincides with the ZO isochrone that corresponds to the NMO/DMO stack process or such that it reduces to a point diffractor as required for the PreSDM operator. The mirror can be changed by means of three parameters: The distance from the surface point  $\xi_0$  to the reflector point  $R$  which is for a simple two layer model equivalent to  $R_{NIP}$ , the radius of curvature of the mirror, i.e.,  $R_N$  at point  $R$ , and the direction of the mirror determined by the angle  $\alpha$ . All three attributes are integral quantities.  $R_{NIP}$  determined at the surface is, for example, the integral quantity of all transmissions and refractions along the central ray from NIP to  $\xi_0$ .

### 3.1.5 Parameter search

The values of the CRS Stack attributes which build up the best traveltime surface to simulate the point  $P_0$  have to be found. No initial guess is used in order to have no restrictions. The only restriction is, to search for each attribute within a user-defined range and determine the best value with a coherence analysis. To be on the safe side, this range is chosen rather to large than to small. The three CRS Stack attributes are not found at once because it would be computationally much too expensive. Müller (1999) and Jäger (1999) describe the complete CRS Stack computation routine which involves three one-parameter searches. Optionally, a local optimisation can be done where the initially found parameters are the starting point in the three-dimensional attribute domain. The optimised three parameters are determined in one step. The optimisation routine, which is very time consuming, uses the flexible polyhedron search according to Nelder and Mead (1965). Of course, the following steps are the same for the parabolic traveltime Equation (3.2).

**First step:** A combined parameter is searched for in the CMP gather, thus,  $\xi = \xi_0$  and Equation (3.3) reads:

$$t_{hyp}^2(\xi, h) |_{(\xi=\xi_0)} = t_0^2 + 2 \frac{t_0}{v_0} \cos^2 \alpha \frac{h^2}{R_{NIP}}. \quad (3.4)$$

The dependency on  $\alpha$  and  $R_{NIP}$  can be combined to one parameter  $q$ :

$$q = \cos^2 \alpha R_{NIP}^{-1}, \quad (3.5)$$

which can be related to the NMO-velocity (Hubral and Krey, 1980, see Equation 6.9 with different notation):

$$v_{NMO}^2 = \frac{2v_0 R_{NIP}}{t_0 \cos^2 \alpha} = \frac{2v_0}{t_0} q^{-1}. \quad (3.6)$$

This step is called *Automatic CMP Stack* and corresponds in principle to a velocity analysis as performed on selected CMP gathers in standard processing. Here, the optimal stacking hyperbola is found for each single point to be simulated in the ZO section.

**Second step:** In the ZO section, made available by the Automatic CMP Stack, Equation (3.3) can be reduced to:

$$t_{hyp}(\xi, h) |_{(h=0, R_N=\infty)} = t_0 + \frac{2}{v_0} (\xi - \xi_0) \sin \alpha, \quad (3.7)$$

where the second-order term in  $(\xi - \xi_0)$  has been neglected. This first-order approximation is equivalent to a plane wave approximation as  $R_N = \infty$  and one obtains, with this *Plane Wave Stack*, the emergence angle  $\alpha$ . The angle can be inserted into Equation (3.5) and then be solved for  $R_{NIP}$ .

**Third step:** While  $\alpha$  is already known, the third parameter  $R_N$  is searched for by the usage of

$$t_{hyp}^2(\xi, h) |_{h=0} = \left[ t_0 + \frac{2}{v_0} (\xi - \xi_0) \sin \alpha \right]^2 + \frac{2}{v_0} t_0 \cos^2 \alpha \frac{(\xi - \xi_0)^2}{R_N}. \quad (3.8)$$

$R_N$  associated with the maximum coherency is chosen to simulate the corresponding ZO point in step four.

**Fourth step:** All three parameters are found for a certain ZO point, thus, they can be inserted into Equation (3.3). The subsequent stack along the traveltime curve is called *Initial CRS Stack*. The word 'initial' is used because the CRS Stack attributes used for this stack serve as initial values for the optional optimisation process which yields the *Optimised Stack*.

## 3.2 Application of attributes

The attributes of the CRS Stack characterise the emerging wavefront. Consequently, the attributes are related to the physical process of wave propagation through the examined medium which in turn determines the kinematical and dynamical behaviour of the wave. Thus, it should be possible to develop applications which describe the kinematic and dynamic properties of the wave by means of CRS Stack attributes. In the next subsections, I show applications of the attributes which will be used in combination with various methods and seismic processing steps in the following chapters.

### 3.2.1 Projected Fresnel zone

The derivation of the projected Fresnel zone was presented in Section 2.5. There, I mentioned that Hubral et al. (1993b) were able to compute the projected Fresnel zone if the event in a CMP and ZO section has been identified as one and the same and the traveltimes of this event had been picked. The disadvantage of that method is the identification because it requires interactive picking which is quite time consuming. The minimum aperture is evaluated non-interactively, i.e., automatically, with the subsequent equations. The element  $B$  of the propagator matrix  $\underline{\mathbf{T}}$  can be expressed in terms of the 2-D zero-offset CRS Stack attributes, Müller (1999):

$$B = \frac{2v_0}{\cos^2 \alpha} \left( \frac{1}{R_{NIP}} - \frac{1}{R_N} \right)^{-1}. \quad (3.9)$$

Inserting Equation (3.9) into Equation (2.33), the projected Fresnel zone is obtained by:

$$\left| 2 \frac{(\xi - \xi_0)^2 \cos^2 \alpha}{v_0} \left( \frac{1}{R_{NIP}} - \frac{1}{R_N} \right) \right| \leq T. \quad (3.10)$$

Taking only the boundary of Inequation (3.10) into account and solving it for  $(\xi - \xi_0)$  gives half the size of the minimum aperture. Equation (3.10) can also be derived by subtracting the parabolic reflection traveltime (3.2) from its corresponding diffraction traveltime which is obtained if  $R_{NIP} = R_N$ . Thus, for half the size of the projected Fresnel zone, considering parabolic traveltime curves, I obtain

$$r_p = |\xi - \xi_0| = \frac{1}{\cos \alpha} \sqrt{\frac{v_0 T}{2 \left| \frac{1}{R_{NIP}} - \frac{1}{R_N} \right|}}. \quad (3.11)$$

Please note that Equation (3.11) does not depend on the half-offset  $h$ . Thus, with the parabolic 2nd order CRS traveltime approximation it is not possible to determine the minimum aperture in offset direction. In Section 3.2.2, I performed some examinations regarding the size of the projected Fresnel zone for a finite-offset configuration.

In order to compute the size of the projected Fresnel zone with the hyperbolic traveltime I need Equation (3.3). Setting again  $R_{NIP} = R_N$  and subtracting the reflection time  $t_{hyp}$

from the diffraction time  $t_{hyp,d}$  the traveltim difference for the ZO case ( $h = 0$ ) yields

$$\begin{aligned} \frac{T}{2} = |t_{hyp,d} - t_{hyp}| = & \left| \sqrt{\left[ t_0 + \frac{2}{v_0}(\xi - \xi_0) \sin \alpha \right]^2 + \frac{2}{v_0} t_0 \cos^2 \alpha \frac{(\xi - \xi_0)^2}{R_{NIP}}} \right. \\ & \left. - \sqrt{\left[ t_0 + \frac{2}{v_0}(\xi - \xi_0) \sin \alpha \right]^2 + \frac{2}{v_0} t_0 \cos^2 \alpha \frac{(\xi - \xi_0)^2}{R_N}} \right|. \end{aligned} \quad (3.12)$$

Equation (3.12) cannot be solved analytically for the requested minimum aperture. Thus, the equation has to be solved numerically, i.e., it has to be searched for  $(\xi - \xi_0)$  so that the traveltim difference equals half the period of the mono-frequent wave.

### 3.2.2 Projected Fresnel zone for finite-offset configuration

The size of the minimum aperture is known for ZO in order to simulate the ZO section. But nothing is known about the change of the aperture if the stack includes finite offsets, which is always the case as long as the ZO section is simulated. In the program of the CRS Stack the user chooses the size of the maximum offset that should be taken into account. The size of the aperture decreases in midpoint direction with increasing offset such that the aperture is of elliptical shape, Mann (2000). Kvasnička and Červený (1996) present exact analytical expressions of interface Fresnel zones for direct and unconverted seismic body waves. Their equations are valid for laterally homogeneous one-layer models with either a horizontal or dipping interface. I computed the associated projected Fresnel zones and expressed their equations in terms of the CRS Stack attributes. This enabled me to compare it with the projected Fresnel zone computed by means of the hyperbolic traveltim approximation (3.3) with  $h \neq 0$ .

Figure 3.5 shows a *Fresnel section*, which is an ellipse as long as the layer is homogeneous. This is a 2-D slice of a 3-D *Fresnel volume* for a point source at  $S$  and a receiver at  $G$ . It is an idealised picture of the extent of the region that contributes to a primary reflected signal. The penetration of the section into the reflector is not considered. The image source  $S^*$  and the corresponding Fresnel section, using the velocity  $v$  of the first layer, is depicted in order to make the up-coming descriptions more clear. The Fresnel section is given by all Fresnel rays from the image source  $S^*$  via an arbitrary point  $F$  to the receiver  $G$  that needs no more than  $T/2$  compared to the traveltim of the straight raypath ( $S^*G$ ). Here,  $T$  is again the period of a mono-frequent wave.  $z_S$  ( $z_G$ ) is the distance of the reflector normal to the source (receiver). The semi-axes are denoted by  $a$  and  $b$ , the reflection point on the reflector  $\Sigma$  is  $Q$  and the radius of the interface Fresnel zone is  $r$ . The exact analytical expression for the radius of the interface Fresnel zone for a dipping interface in a two-layer model with constant layer velocities is given by Kvasnička and Červený (1996):

$$r = b \frac{\sqrt{1 + g^2}}{1 + g^2 \nu^2} \sqrt{1 - \frac{m^2}{a^2} + g^2 \nu^2}, \quad (3.13)$$

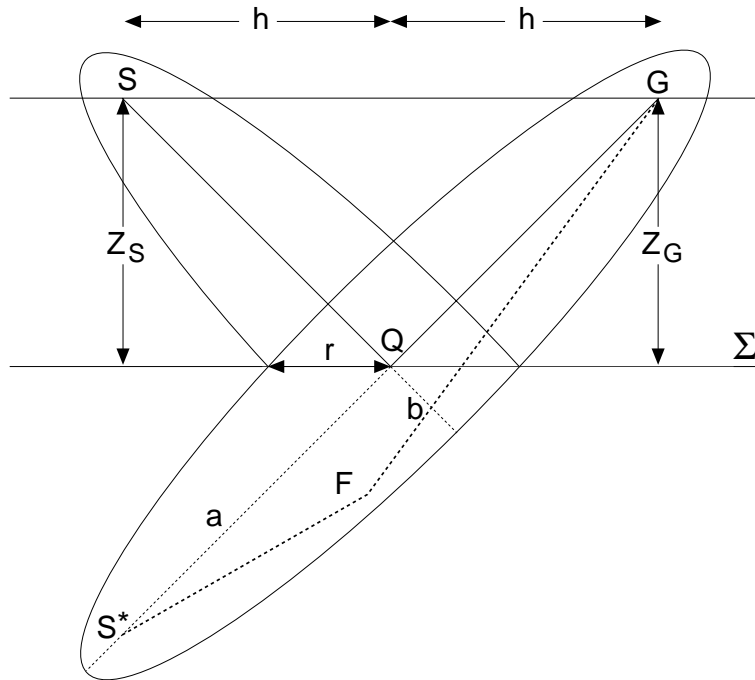


Figure 3.5: 2-D slice of a 3-D Fresnel volume. As the offset  $h$  increases, the interface Fresnel zone radius  $r$  also increases. The interface Fresnel zone is no longer symmetrical to point  $Q$  if the interface  $\Sigma$  dips.

where  $g = 2h/(z_S + z_G)$ ,  $\nu = b/a$  and  $m$  is given by Equation (3.15). The semi-axes are expressed by:

$$a = \frac{l}{2} \left( 1 + \frac{\nu T}{4} \right), \quad b = \frac{\sqrt{\nu T l}}{2} \left( 1 + \frac{\nu T}{4l} \right)^{1/2}. \quad (3.14)$$

Here,  $l$  is the length of the distance  $\overline{SQG}$  in Figure 3.5. The second terms in the brackets in Equation (3.14) is neglected for a high-frequency approximation as it is the case for the CRS Stack. The variable  $m$  of Equation (3.13) and  $l$  of Equation (3.14) can be obtained by

$$m = \frac{1}{2}(z_S - z_G)\sqrt{1 + g^2}, \quad l = (z_S + z_G)\sqrt{1 + g^2}. \quad (3.15)$$

In Figure 3.5 it is obvious that  $z_S \neq z_G$  in case of a dipping layer. The shown ellipse is the boundary of the Fresnel volume in the in-plane, i.e., the plane in which the reflection ray is embedded. In Appendix B, I put down the calculations how to project the Fresnel zone with radius  $r$ , Equation (3.13), expressed in terms of the CRS Stack attributes  $\alpha$ ,  $R_{NIP}$ , and  $R_N$ .

Figure 3.6 shows the ratio of the projected Fresnel zone radii computed with the hyperbolic and parabolic traveltime formulae described above and divided by the exact

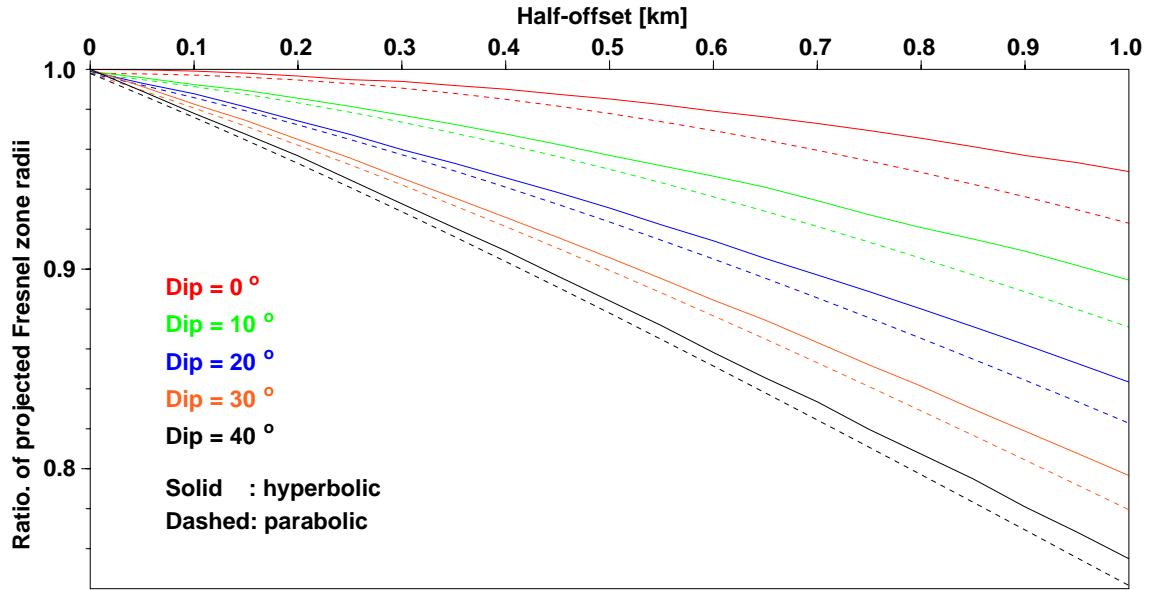


Figure 3.6: The ratio of the approximated and exact projected Fresnel zones for finite offset decreases with increasing half-offset. Thus, the projected Fresnel zone using the CRS Stack traveltimes (3.2) and (3.3) becomes smaller with increasing half-offset.

analytical expression (B.17) in Appendix B. The following parameters have been used:  $R_{NIP} = 3$  km,  $R_N = \infty$ ,  $v_0 = 2.5$  km/s, and  $T = 0.04$  s. The solid curves depict the ratio using the hyperbolic traveltime approximation, whereas the dashed curves correspond to the calculations with the parabolic equivalent. The projected Fresnel zones coincide if the ratio equals 1, which is always the case for zero-offset. Looking at Figure 3.6, three facts can be stated: First, the deviation from the exact solution increases with increasing offset. Second, the ratio decreases with increasing dip. Third, the parabolic approximation is always not as accurate as the hyperbolic approximation but their curves come closer as the dip is incremented and the offset is held constant. Here, a 10 % deviation for the hyperbolic case is reached for a half-offset of 1000 m and a dip of  $10^\circ$  or a half-offset of 450 m and a dip of  $40^\circ$ . Because, the ratio is always smaller than 1, except for ZO, it means that the exact projected Fresnel zone is bigger than the approximated one. It is not shown here, but the deeper the reflector the smaller the deviation. The same is valid for increasing frequencies. If, for instance,  $R_{NIP} = 6$  km instead of 3 km, the projected Fresnel zone for the hyperbolic approximation deviates only 12 % from the exact one at 1 km half-offset and a dip of  $40^\circ$ .

The conclusion is that, in principle, the projected Fresnel zone can be estimated quite well with the hyperbolic ZO traveltime approximation for small offsets and a simple subsurface.

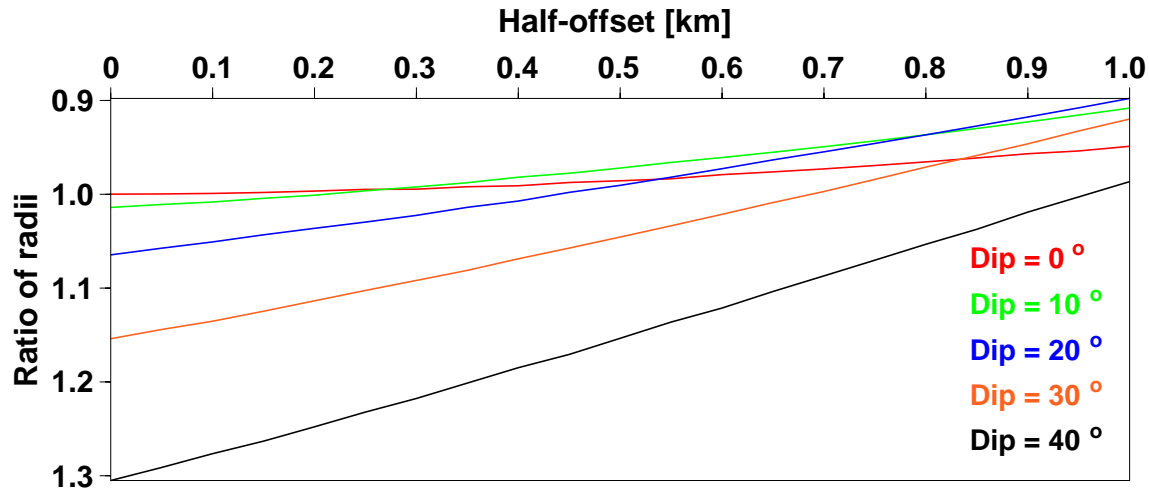


Figure 3.7: Ratio of the approximated and exact projected Fresnel zone radii computed with the hyperbolic approximations of Figure 3.6, but with a proposal to use the NMO-velocity and to divide the results of Figure 3.6 by the Cosine of the emergence angle.

### 3.2.3 Proposal for an aperture in offset-direction

The S/N ratio of a stacked section is the best if the stacking operator uses the minimum aperture that is equivalent to the projected Fresnel zone. Thus, I would propose three changes of the projected Fresnel zone using the CRS Stack traveltime: First, use the NMO-velocity (3.6) instead of the velocity of the first layer. Second, assume flat horizons,  $R_N = \infty$ . Third, divide the resulting projected Fresnel zone by  $\cos \alpha$ . The result of these changes is depicted in Figure 3.7. The hyperbolic traveltime approximation and all the parameters, which had been previously used for producing Figure 3.6, have been taken. In contrast to Figure 3.6, the ratio of the radii is most times greater than 1. This is due to the  $\cos \alpha$  in the denominator of the NMO-velocity and the factor of the third change  $1/\cos \alpha$ . Except for a horizontal layer, the deviation from 1 starts at ZO, decreases at first continuously with offset and increases again at large offsets. A ratio greater than 1 is to be preferred as it encompasses at least the first projected Fresnel zone which ensures the recovery of the signal, Schleicher et al. (1997) and Sun (1998).

#### 3.2.3.1 Implementation

In the latest version of the CRS Stack, Mann (2000), the aperture is of elliptical shape, see Figure 3.8. The aperture in midpoint direction for ZO, meanwhile, equals the projected Fresnel zone. The maximum offset to be considered has to be determined by the user. This parameter, obviously, has to be always set manually. It is implemented in a time-variant manner and corresponds to the great semi-axis of the half-ellipse of the aperture in Figure 3.8. Although it has been proven to be successful in practice, a discrepancy regarding theory exists.

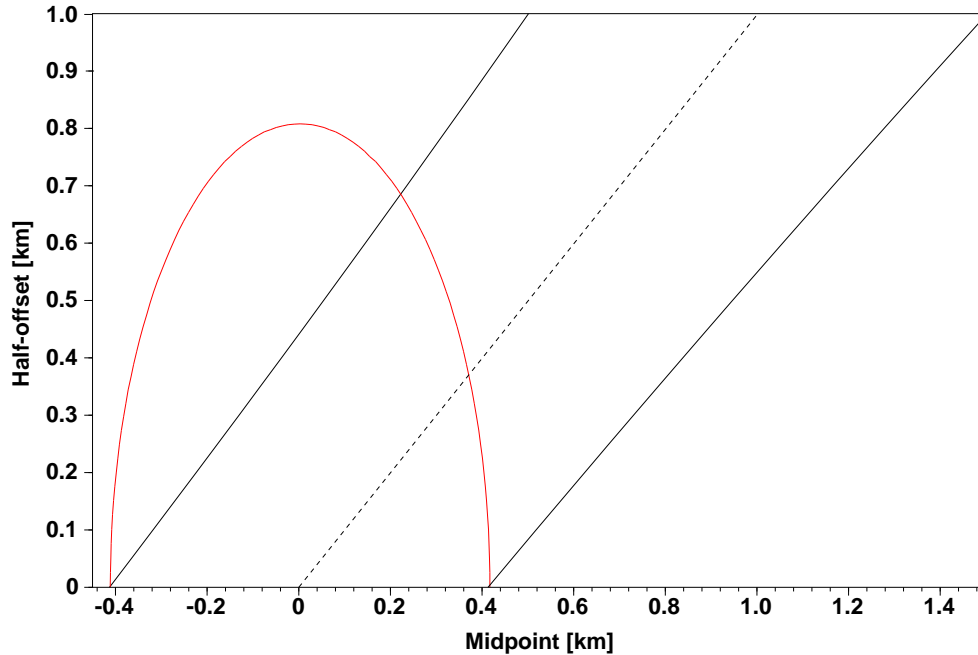


Figure 3.8: The elliptically-shaped aperture is the one that is implemented in the CRS Stack. The black lines mark the boundary of the exact projected Fresnel zone, see Appendix B.

The facts are that in general

- the aperture should increase in midpoint direction with increasing offset and
- the boundary of the aperture is not parallel to a constant midpoint but runs diagonally in the half-offset-midpoint domain.

Several items justify the application of an elliptically shaped aperture:

- The CRS Stack is based on paraxial ray theory,
- the hyperbolic traveltime Equation (3.3) is a part of a Taylor expansion, thus, it is an approximation, and
- the S/N ratio decreases with increasing distance from the ZO central ray.

The black lines in Figure 3.8 are associated with the exact boundary of the aperture, where the same parameters as before have been used and a dip of  $20^\circ$  was assumed. The ellipse that depicts the aperture as it is actually implemented in the CRS Stack is only exact for ZO but not for any finite offset. From Figure 3.8 it can be deduced that the stack result should change compared to the conventional result if the exact aperture were applied. This is due to the fact that a non-negligible amount of traces of the considered apertures

differs from each other. Thus, I recommend changing the aperture so that the great semi-axis of the ellipse is parallel to the family of centres of the projected Fresnel zones for finite offsets (dashed line in Figure 3.8).

I propose to use a rotated ellipse as an aperture instead of using the complete midpoint range at a certain offset because the distance to the central ray increases such that the paraxial ray theory might be violated and the S/N ratio might be too poor. These are suggestions for examinations in future time.

At present, I use a non-rotated ellipse as shown in Figure 3.8 for the *Fresnel CRS Stack*. The small semi-axis in CMP direction at ZO has got the size of the projected Fresnel zone. The large semi-axis is twice as large as the small semi-axis which is a good empirical value.

### 3.2.4 Geometrical spreading in terms of CRS Stack attributes

In Section 2.6, I described the theory of the GS, i.e., its relation to the ray Jacobian as well as its connection to paraxial rays. I still have to put down the equation of the GS in terms of the CRS Stack attributes. Because the in-line GS and the projected Fresnel zone are related to each other, Expression (2.43), the in-line GS is similar to Equation (3.11):

$$|L_2| = \frac{\cos \alpha}{v_0} |B|^{1/2} = \sqrt{\frac{2}{v_0} \left| \frac{1}{R_{NIP}} - \frac{1}{R_N} \right|^{-1}}. \quad (3.16)$$

Thus, by multiplying the projected Fresnel zone (3.11) by a factor of  $2v_0 T^{1/2} \cos \alpha$ , I arrive at the GS.

The out-of-plane geometrical spreading,  $\sqrt{\sigma}$ , of Equation (2.44) can be approximated by the CRS Stack attributes. For plane horizontal iso-velocity layers the following relationship between the RMS velocity and the quantity  $\sigma$  of Equation (2.44) exists:

$$v_{RMS} = \sqrt{\frac{\sigma}{t_0}}. \quad (3.17)$$

For parallel plane dipping iso-velocity layers, the RMS velocity equals  $v_{NMO} \cos \alpha$ , where  $\alpha$  is the dip and emergence angle for ZO, respectively. Since a relation between  $v_{NMO}$  and the CRS Stack attributes exists (Hubral and Krey, 1980, see Equation (6.9) with different notation), I approximate the quantity  $\sigma$  for arbitrary media with:

$$\sigma \approx t_0 v_{NMO}^2 = 2v_0 R_{NIP}. \quad (3.18)$$

### 3.2.5 Discussion

In Section 3.2 I presented two applications of the CRS Stack attributes: (i) the projected Fresnel zone and (ii) the geometrical spreading. It is new that they are expressed in terms of model independent attributes, which are found automatically due to coherency analysis. Therefore, their values do not depend on the picking and interpretation of the user

anymore. Such a conventional method is described by Schleicher et al. (1997).

The determination of the projected Fresnel zone has two positive aspects: First, the number of traces to be stacked to simulate a ZO section becomes a minimum. Second, stacking within the projected Fresnel zone produces the best S/N ratio. Unfortunately, the projected Fresnel zone is only exact in the ZO section. This problem can be solved exactly with the common-offset CRS Stack Zhang et al. (2001) or approximately with the proposal I made in Subsection 3.2.3.

I also produced, what I would call, a recursive Fresnel CRS Stack. It is obtained with the following steps: (i) search for the three CRS Stack attributes, compute the projected Fresnel zone and produce a Fresnel CRS Stack. (ii) go to the beginning of the program and search again for the three CRS Stack attributes but now use the projected Fresnel zone as the aperture in midpoint direction and twice the projected Fresnel zone as the aperture in offset direction. (iii) compute the projected Fresnel zone and the recursive Fresnel CRS Stack with the recursively computed CRS Stack attributes. In comparison, the quality of the recursive Fresnel CRS Stack decreased. The events became more rugged and more discontinuous. The size of the projected Fresnel zone decreased. If the recursive computation of the CRS Stack attributes is performed several times each of the attributes does not approach asymptotically a value. Therefore, the recursive Fresnel CRS Stack does not converge to a final ZO section.

The simulated ZO section does not display correctly the ratio of amplitudes of events. The multiplication of the ZO section with the in-plane and out-of-plane GS remedies the discrepancy. The disadvantage is that the out-of-plane GS, which cannot be neglected in the real world, assumes a horizontally layered earth. But it is known that a simplification like the horizontally layered earth is often used by the oil industry to obtain successful initial results. The validity for true-amplitude processing is checked in Section 4.3.

Multiplying the simulated ZO section with the in-plane and out-of-plane GS has another advantage. It serves as a “natural” gain function. Usually, some gain function, which can be a quite sophisticated time and space varying gain function, is applied to seismograms in order to enhance amplitudes at large traveltimes, often without physical background.

### **3.3 Real data example**

In cooperation with the oil and gas company BEB, I was supplied with a real data set in order to apply the CRS Stack to it. Therefore, I had the chance of testing the new features on a real data set. On the one hand the results are compared to the NMO/DMO stack supplied by Geco-Prakla and on the other hand the conventional CRS stacks are compared with the new implementations. These involve the projected Fresnel zone and the geometrical spreading. The new applications were also tested on synthetic data. The results are shown in connection with true-amplitude migration in Section 4.3.

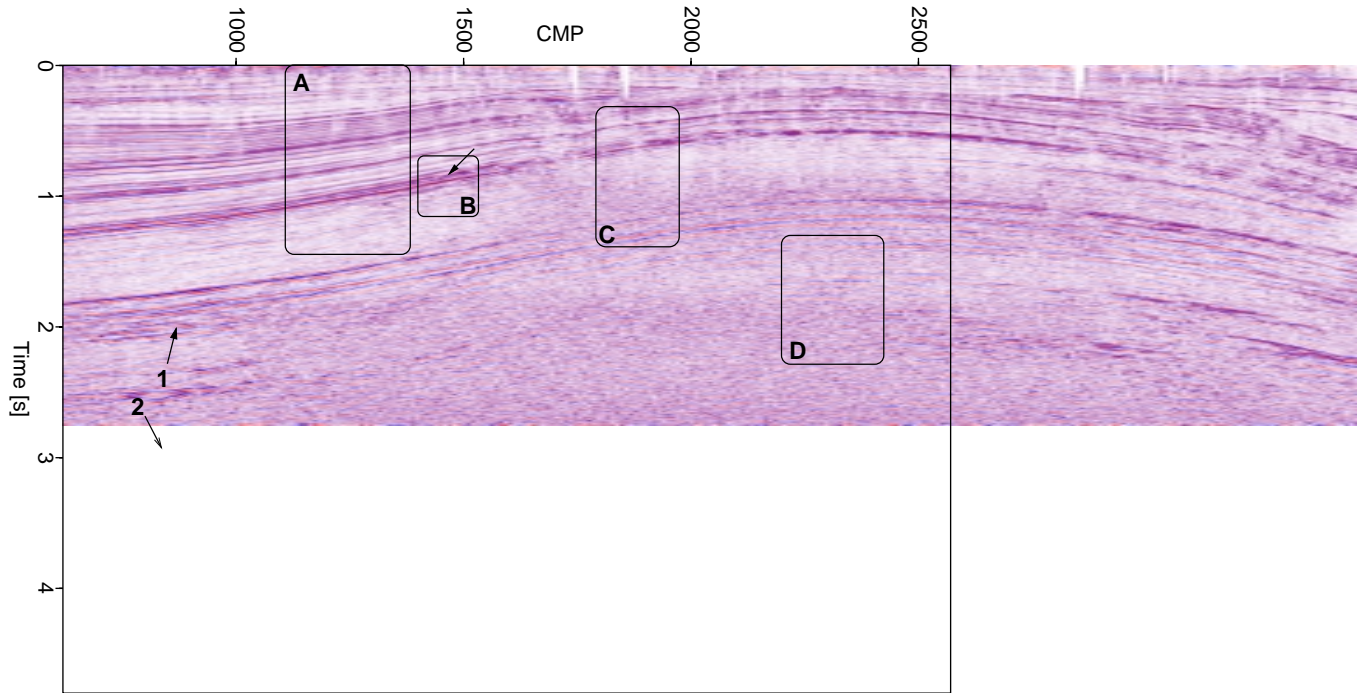


Figure 3.9: NMO/DMO stack produced by Geco-Prakla.

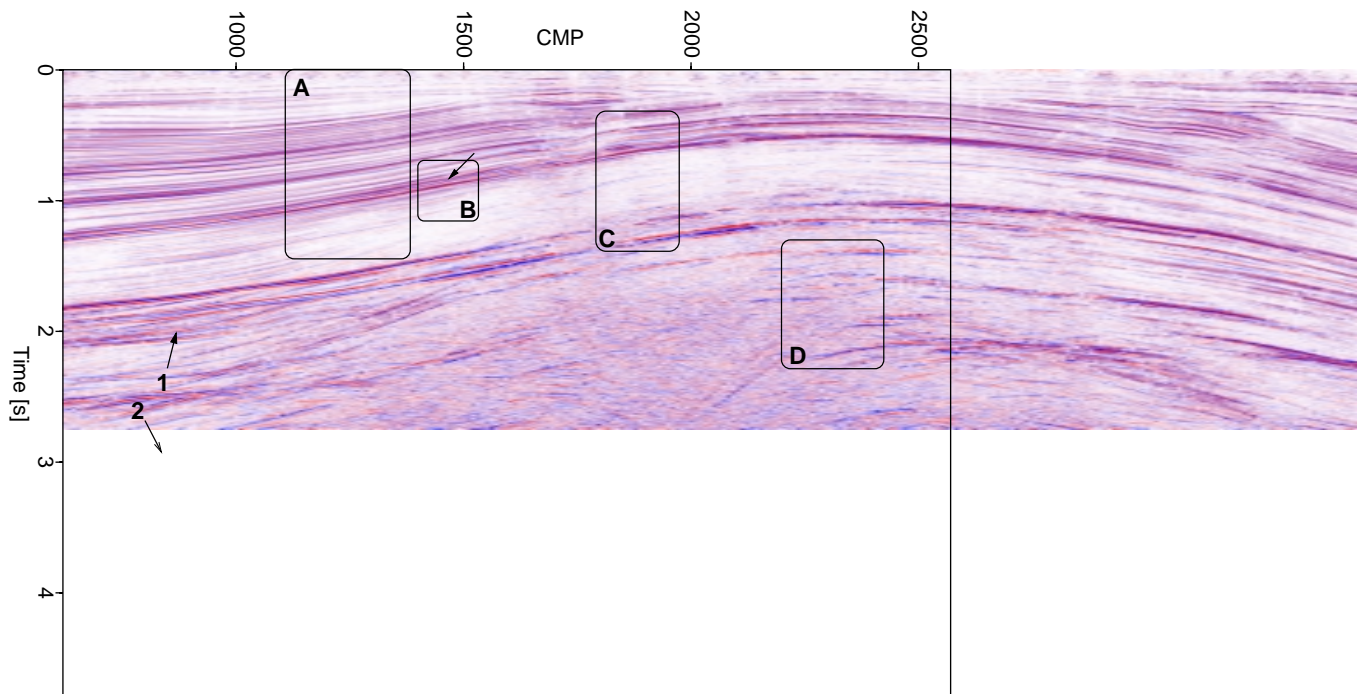


Figure 3.10: Optimised CRS Stack.

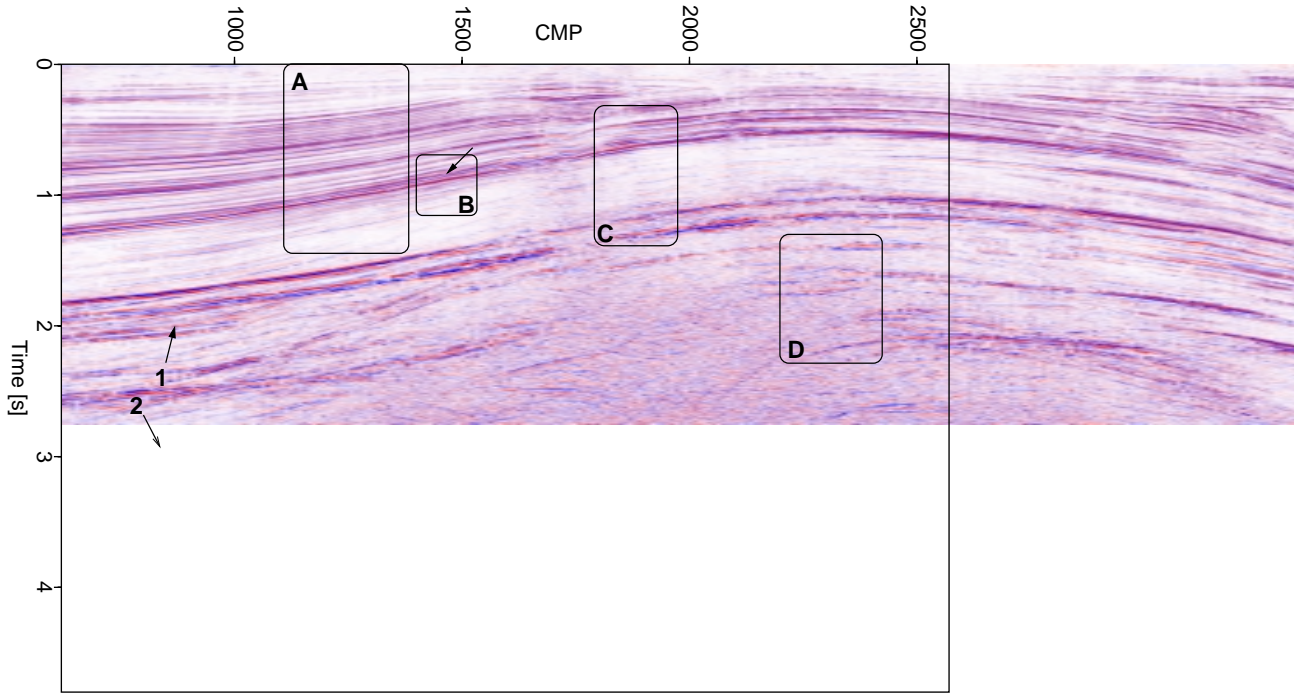


Figure 3.11: Initial CRS Stack.

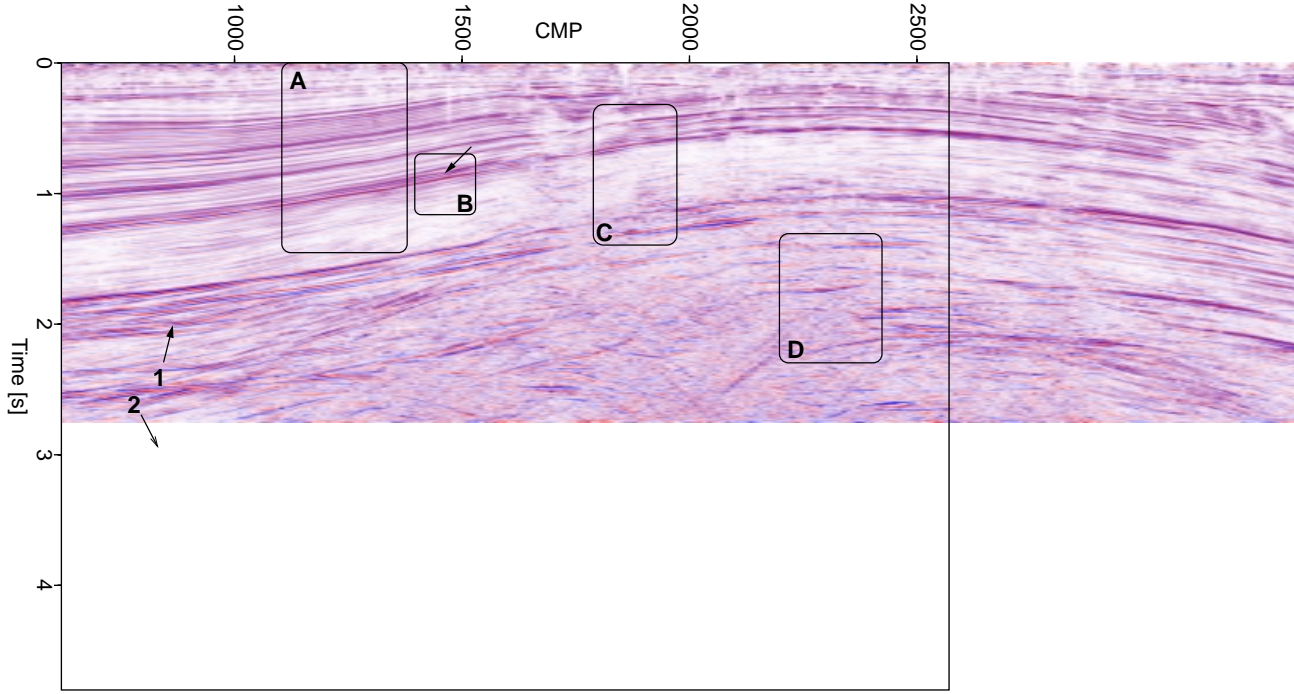


Figure 3.12: Fresnel CRS Stack.

The axes of all sections are not the original ones, as I had to falsify them for publication. The falsification was done after the complete processing chain. Before I received the multi-coverage data set, the data were processed with the following processing chain: manual trace editing, spherical divergence correction using a time and space variant velocity function, minimum delay transformation, surface-consistent deconvolution, various static corrections, muting of the direct wave.

### 3.3.1 The new Fresnel CRS Stack compared with the old CRS stacks

Figures 3.9 to 3.12 show four different simulated ZO sections of the same multi-coverage data set. In the seismograms, blue (red) denotes a positive (negative) amplitude and white corresponds to the zero-crossing of the signal. Figure 3.9 displays the conventional NMO/DMO stack of Geco-Prakla, Figure 3.10 is the Optimised CRS Stack, Figure 3.11 is the Initial CRS Stack, and Figure 3.12 is the Fresnel CRS Stack. The Initial and Optimised CRS Stack were introduced by Müller (1999). The Fresnel CRS Stack is new. In order to see events at late times, the seismograms were multiplied by  $e^{t_0}$ , where  $t_0$  is the ZO two-way-traveltime. Afterwards, an automatic gain control (AGC) with a window length of 1 s was applied.

At first glance, the difference of the S/N ratio of the conventionally processed data and the CRS Stack results are most obvious. The basic, large scale events are easily detected in each section: the dome-like events, the wedge on the upper right, the collapse of the structures in box A, and the deeper event at the lower right. The dome-like events denoted 1 and 2 can be followed, with some interruptions, from the left to the right. The events from the top up to about 0.4 s are not imaged well, because of the muting within the CMP gather which has been done during pre-processing.

The events of the Optimised CRS Stack are the smoothest ones and the events have nearly everywhere the best continuity. An exception can be seen in box A. The short events in the middle of this collapsing structure are most continuous in the Fresnel CRS Stack. To my opinion all CRS Stack sections are better than the conventional NMO/DMO stack. Thus, I compare the different CRS Stack results with each other and will focus on the events enclosed by the boxes.

For the Fresnel CRS Stack, the stacking aperture was two to three times smaller than for the Initial or Optimised CRS Stack. The Fresnel CRS Stack shows two major improvements: First, the resolution is higher than in the Initial and Optimised CRS Stack. Second, the events are more continuous than in the Initial CRS Stack. It is not as good as in the Optimised CRS Stack because it is not possible to have on the one hand maximal continuity and on the other hand maximal resolution. Thus, I suppose that the Fresnel CRS Stack combines optimal continuity with optimal resolution.

The best example for this is depicted in box A. The boundary of the collapse is well resolved and the continuity of the events is preserved. In the middle of box B are two little events which are only separated by the Fresnel CRS Stack (see arrow). The separation

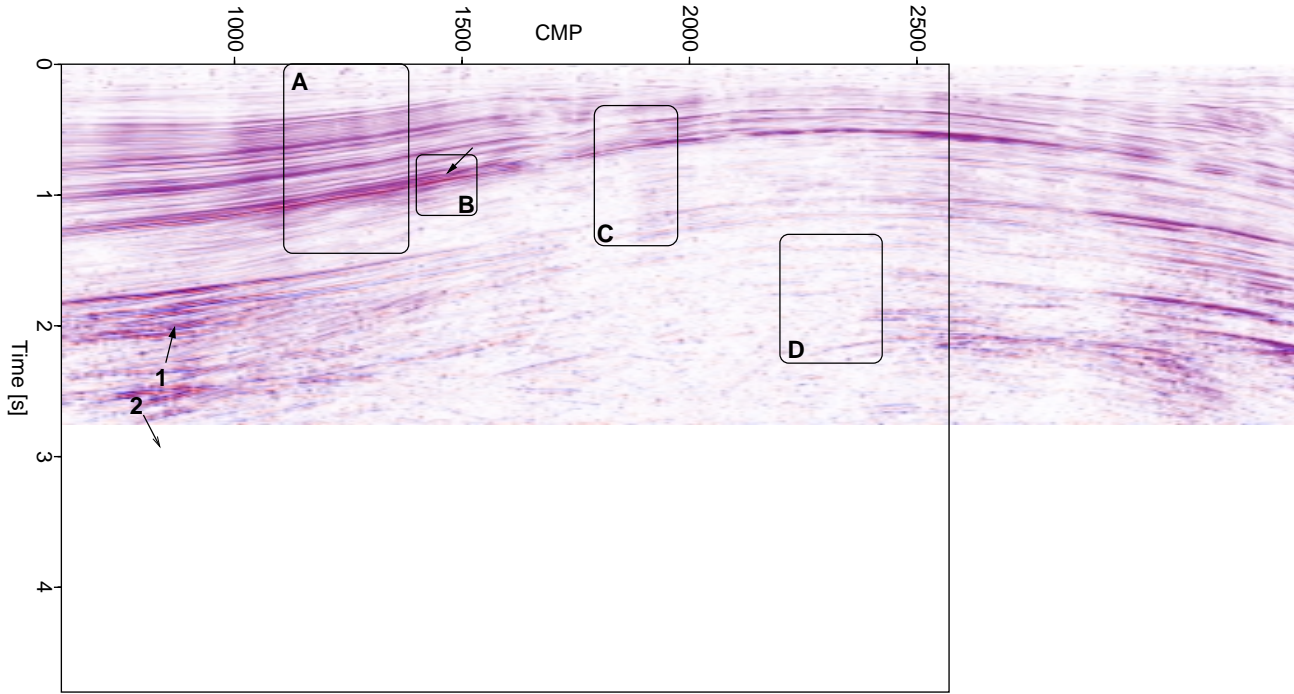


Figure 3.13: Fresnel CRS Stack multiplied by the GSF.

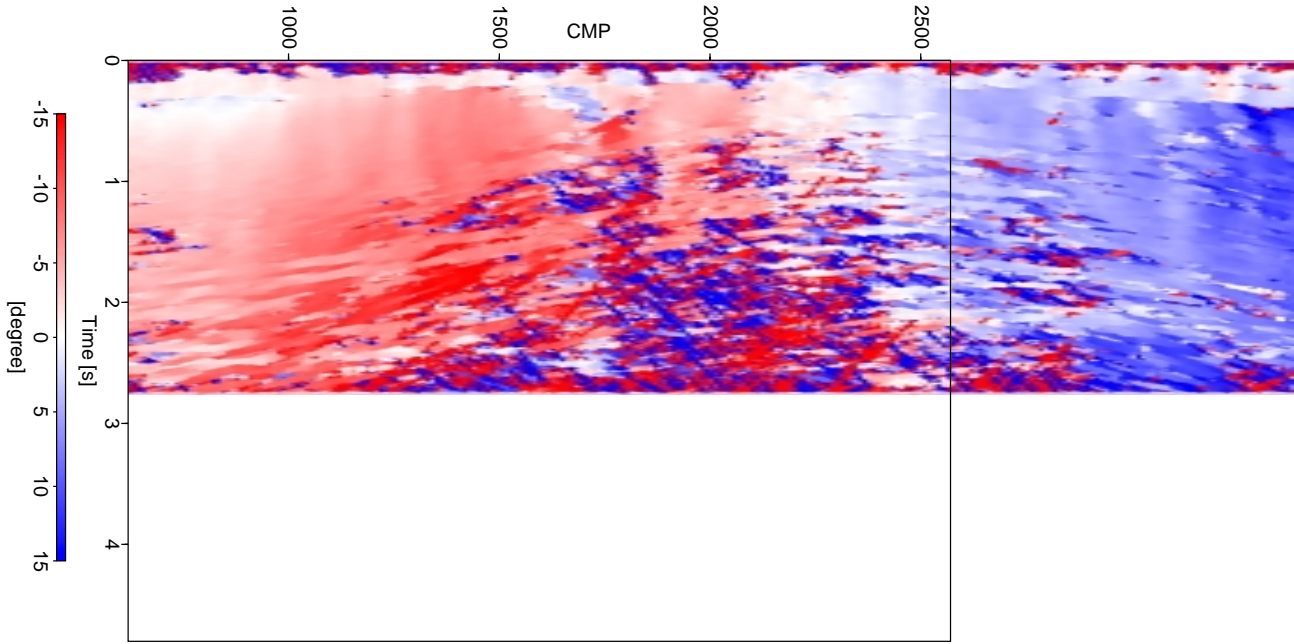


Figure 3.14: Section of the emergence angle.

is indicated in the Initial CRS Stack but in the Optimised CRS Stack it appears as one continuous event. The event in the middle of box C is interrupted over a length of about 450 m. This can be seen again very clear in the Fresnel CRS Stack and it is slightly visible in the NMO/DMO stack. Without the comparison it would hardly be detectable in the Initial and Optimised CRS Stack. A stack of narrow events is visible in the Fresnel CRS Stack in the middle of box D. The boundaries are well resolved compared to the other CRS Stacks.

A disadvantage of the Fresnel CRS Stack can be seen in the large region in the lower part of the section which contains a lot of noise. Because the stacking operator is smaller compared to the one of the Initial and Optimised CRS Stack, coherent noise (snakes) appears more enhanced. Therefore, it is in those regions of the Fresnel CRS Stack more difficult to differ between event and noise than in the other CRS stacks.

Whereas I applied an arbitrary gain function to Figures 3.9 to 3.12, I multiplied Figure 3.13 with the 2.5-D GSF (in-plane GSF times out-of-plane GSF). The GSF in terms of CRS Stack attributes can be regarded as a new “natural” gain function. The pre-processing chain contained a time and space variant spherical divergence correction. If I assume that the transmission loss in this real data set is negligible, the parameters of the correction were not chosen properly, otherwise I would not have to apply the AGC and  $e^{t_0}$  as a gain function. Because the spherical divergence correction did its job not well, I suppose that Figure 3.13 shows the quality of the GSF. Events at all times are made visible without an additional AGC or any other gain function. In Subsection 4.3.2 it becomes evident on synthetic data that the 2-D GSF is correctly determined by the CRS Stack attributes. For the synthetic example, the 2.5-D GSF is approximated quite well, too. If the pre-processing was performed carefully with respect to amplitudes, the application of the GSF to the Fresnel CRS Stack could display correct relative amplitudes, i.e., correct relative reflection coefficients. This could be used for geological interpretation.

### 3.3.2 CRS Stack attribute sections and new applications

The three CRS Stack attribute sections are depicted in Figures 3.14 to 3.16. As the curvature of the anticlinal structure is moderate, the emergence angles encompass a range of about 15 degree, Figure 3.14. The stripe-pattern in the upper left part of Figure 3.14 correlates with the slightly wavy appearance of the package of events. The wavy shape of the events is most obvious in the Fresnel CRS Stack, Figure 3.12. The radius of the NIP wave is shown in Figure 3.15. As expected, the NIP wave radius principally increases with increasing traveltime - the radius of the NIP wave is linear proportional to the traveltime in a homogeneous medium. The lateral change of the NIP wave radius can be traced along some outstanding events. The section of the curvature of the normal wave, Figure 3.16, shows fluctuations of an event more pronounced than the two previous sections. I decided to show the inverse of the radius of the normal wave because if the emerging normal wave is nearly planar, it has either a slight positive or negative curvature. Thus, a planar normal wave with a huge positive or negative radius is represented practically by the same colour, i.e., white. High frequent fluctuations of the values

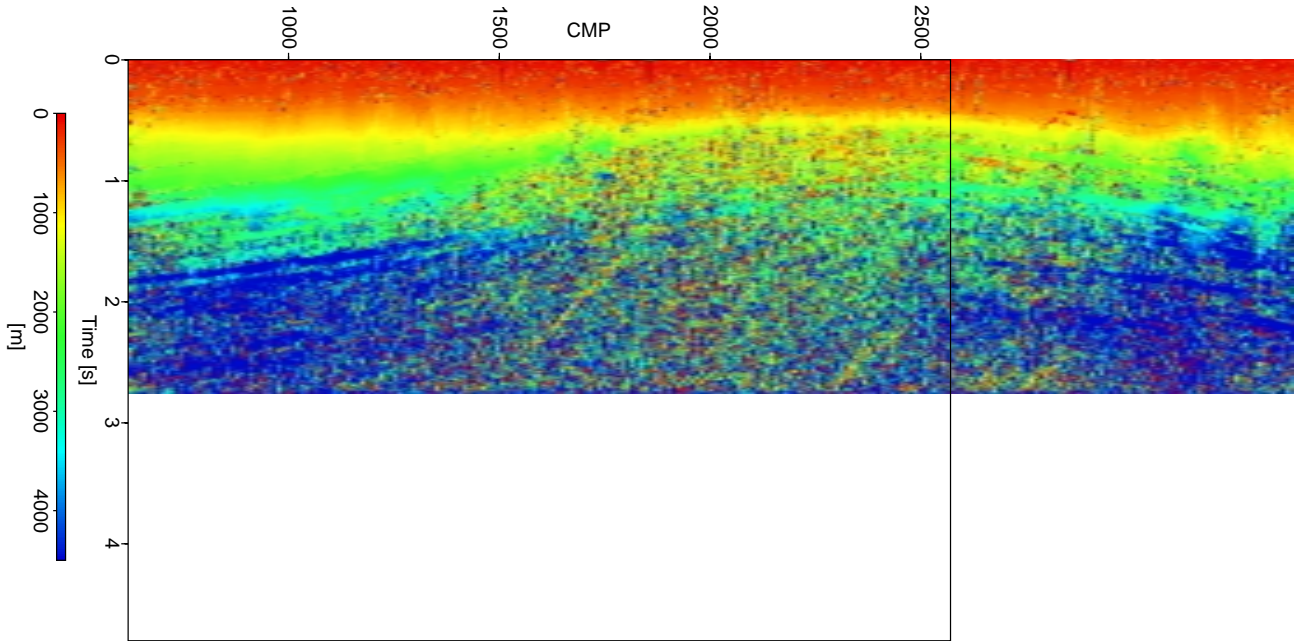


Figure 3.15: Section of the radius of the NIP wave.

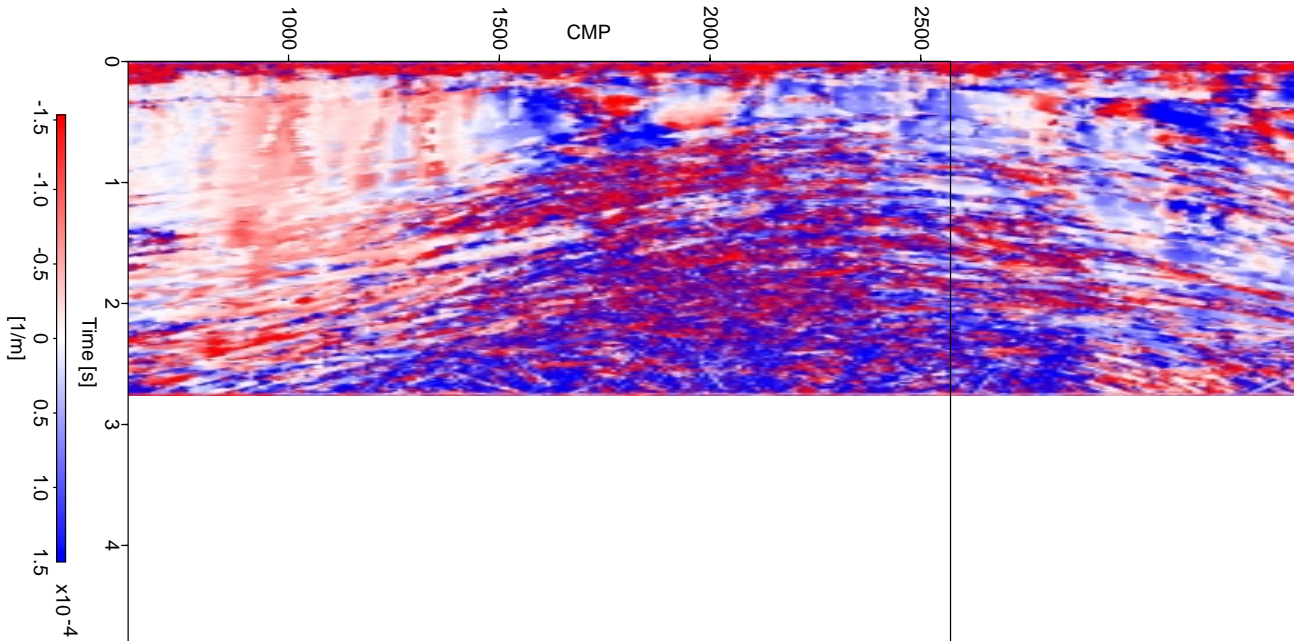


Figure 3.16: Section of the curvature of normal wave.

within the attribute sections correspond to regions with low S/N ratio. The boundary of these low S/N ratio regions are not coincident for the three attribute sections. Compare the areas of short period changes of the emergence angle section with the NIP wave and normal wave section. Because the area of strong fluctuations is the smallest in the emergence angle section and lateral changes are long periodic compared to the other attribute sections, it can be deduced that the emergence angle is the most robust CRS Stack attribute.

The section of the radius of the projected Fresnel zone, Figure 3.17, was obtained with Equation (3.12). This section is very similar to the NIP wave section, because the range of the emergence angle is moderate and the absolute radius of the normal wave is in general quite large compared to the radius of the NIP wave. Thus,  $R_{NIP}$  is for this real data example the dominant parameter for Equation (3.12). For the computation of the projected Fresnel zone, I assumed a wavelet length of 50 ms. This section could be improved by taking into account a time varying wavelet. During wave propagation, the high frequencies are attenuated stronger than the low frequencies. Hence, the time duration of the wavelet increases with increasing traveltime.

Figure 3.18 depicts the 2.5-D GS. It was calculated with equations (2.44), (3.16), and (3.18). Again, some dominant events can be seen and the GS, as expected, increases with increasing traveltime. The close relationship between the projected Fresnel zone and the GS, mentioned in subsection 3.2.4, is also mirrored by the corresponding sections 3.17 and 3.18. The GS can be regarded as a “natural” gain function. Applying it to the associated ZO section makes events visible at small traveltimes as well as at large traveltimes. The GS section of Figure 3.18 was multiplied with the Fresnel CRS Stack of Figure 3.12 in order to obtain Figure 3.13.

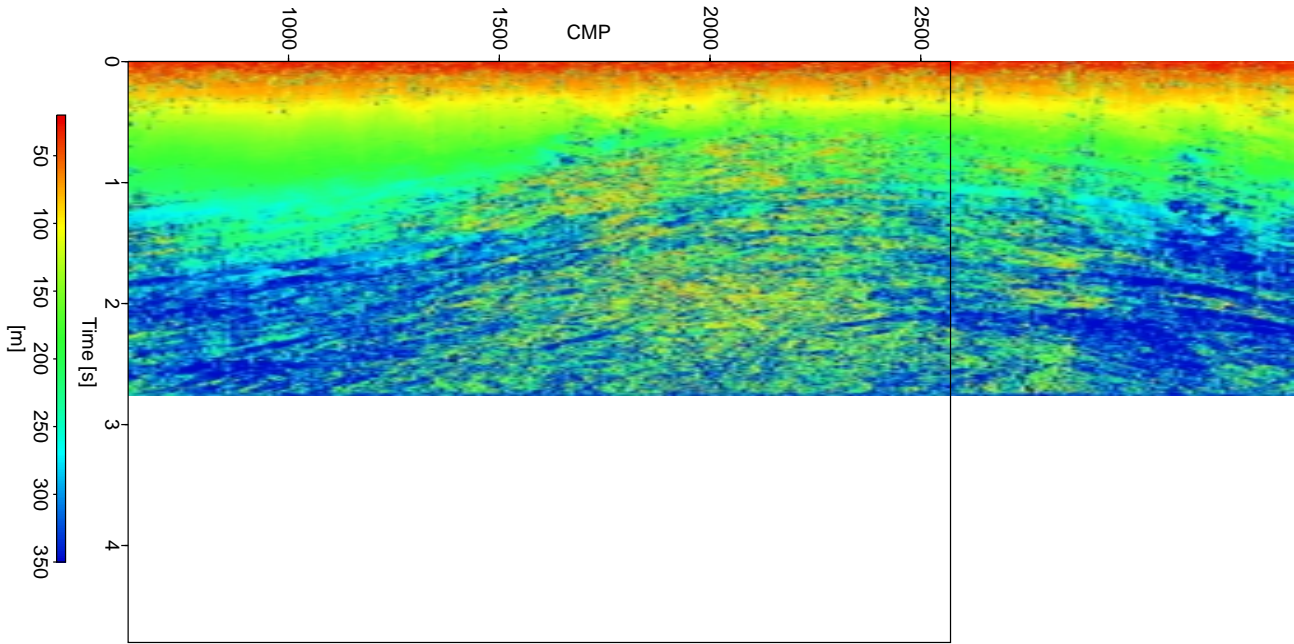


Figure 3.17: Section of the radius of the projected Fresnel zone.

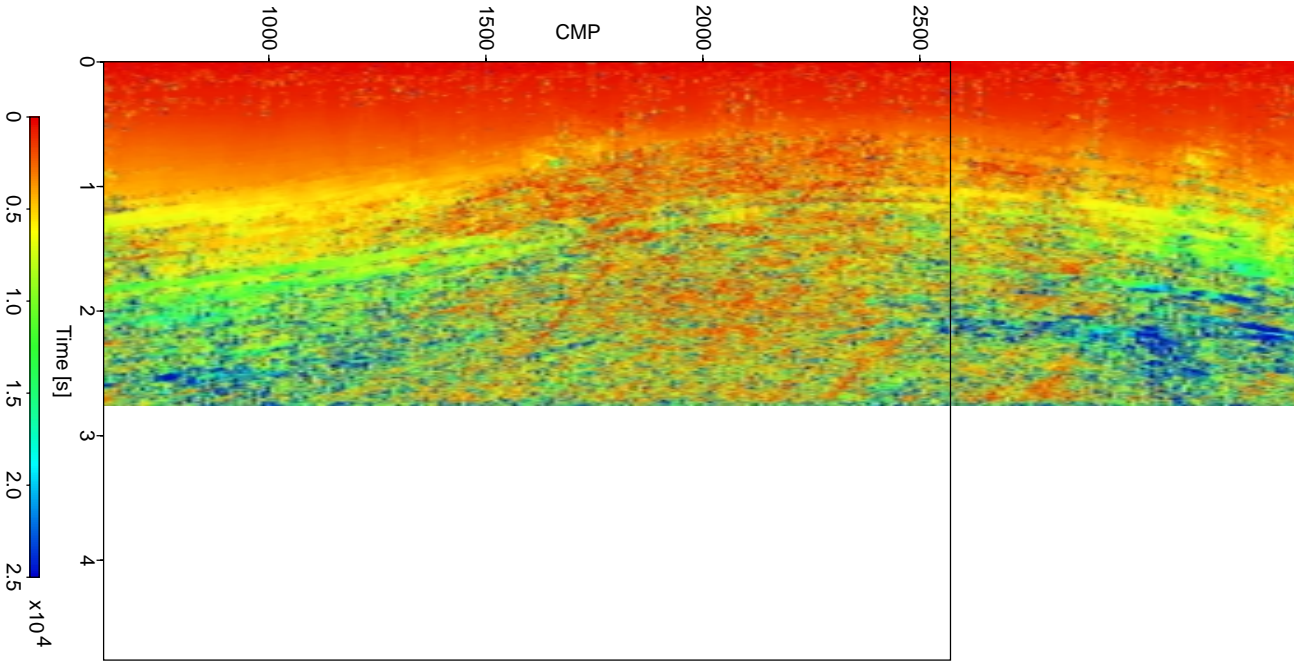


Figure 3.18: Section of the in-plane times out-of-plane GS.



## Chapter 4

# True-amplitude migration with CRS Stack attributes

In reflection seismics, migration is a key method to obtain an image of the subsurface. The immense number of publications at present and over the last few decades reflects the importance of and demand for this topic. Instead of citing many references, I want to focus the reader's attention on a few publications that I reckon are fundamental for the basics and for some widely used modern specialisations.

The statement that Hagedoorn (1954) formed the foundations of migration has found wide acceptance.<sup>1</sup> He described how to perform migration of time sections in 2-D and 3-D based upon the application of wavefront charts and diffraction curves. In the early days of migration, the aim was mainly to transform the data from time to depth, i.e., it was reduced to kinematics. Schneider (1978) gave an integral formulation for migration. He included boundary value problems and thus considered amplitude and waveform reconstruction in addition to diffraction summation. The first algorithm of a finite-difference migration based upon the scalar wave equation was proposed by Claerbout and Doherty (1972). The concept of time-to-depth migration along the image ray was introduced by Hubral (1977). A least-squares method for migration was given by Tarantola (1984). The interested reader gains comprehensive information and an enormous number of references on (true-amplitude) migration by reading Berkhout (1985), Bleistein et al. (2001), and Schleicher et al. (2001). For the more practical aspects of migration and a huge number of examples, I recommend the excellent books of Yilmaz (1987) and Claerbout (1993), where the latter book also offers many source codes for pre-processing and migration.

The data recorded in the field are exposed to “environmental influences” like wind, traffic, source- and receiver-coupling, etc. and to “ray path-bounded” influences like geometrical spreading, transmission loss, intrinsic absorption, attenuation due to thin layers, etc. (Sheriff, 1975). With various filters and deconvolution methods during pre-

---

<sup>1</sup>His work will be honoured with a special issue on migration in *Geophysical Prospecting*. Date of publication is planned to be at the end of 2001.

processing, the effect of environmental noise on the data can be minimised. To account for the change of the amplitude, dynamic migration methods are required. For a layered, laterally inhomogeneous earth where the layers are well separated compared to the dominant wavelength of the propagating wave, the geometrical spreading has got the largest effect on the ZO primary reflections. In the literature, the terminology true-amplitude (TA) migration usually means to compensate for the GS factor and to neglect all other amplitude factors. A comparison of three TA migration approaches associated with the names *Berkhout*, *Bleistein/Hubral*, and *Tarantola* was presented by Gray (1997). That comparison reflects that none of the methods is in every respect superior to the others. It depends on the model, the acquisition geometry and on the considered wave types which method is suited best. Below, I use the TA migration theory of Bleistein and Hubral. Their extensive work on migration and wave propagation is summarised in the books of Bleistein et al. (2001) and Schleicher et al. (2001). In this chapter, I combine the TA migration with the attributes of the CRS Stack, to perform a parsimonious true-amplitude post-stack migration.

## 4.1 2-D true-amplitude Kirchhoff migration

For the signal to be true-amplitude migrated, I use an expression which is the result of zero-order ray approximation. Speaking in terms of 2-D, the signal  $U(\xi, t)$  denotes the principal component of the particle displacement of a primary reflection, i.e., the particle displacement in the direction of the emerging ray, see blue arrows in Figure 4.1:

$$U(\xi, t) = R_c \frac{A}{L} F[t - T_R]. \quad (4.1)$$

$T_R$  denotes the travelttime of the primary reflection.  $R_c$  is the plane wave reflection coefficient (RC) at the reflection point  $M_R$ . The transmission loss along the reflection ray path is given by  $A$  and the geometrical spreading by  $L$ . The analytic point-source wavelet is represented by  $F[t]$ , which consists of the real source wavelet (as real part) and its Hilbert transform (as imaginary part). A reproducible source is assumed, hence,  $F[t]$  does not depend on  $\xi$ . In this work I assume that the transmission loss is negligible, that means  $A = 1$ . Taking those prerequisites into account, Equation (4.1) can be approximated by

$$U(\xi, t) \approx U_0(\xi) F[t - T_R], \quad \text{where} \quad U_0(\xi) = \frac{R_c}{L}. \quad (4.2)$$

This leads to the definition of the analytic true-amplitude signal (Schleicher et al., 1993), i.e., the source wavelet  $F[t]$  is multiplied by the angle-dependent reflectivity. Due to the imaging principle, I have to shift the event to  $t = 0$ . This represents an exploding reflector which yields

$$U(t)_{TA} = R_c F[t] \approx L U(\xi, t + T_R). \quad (4.3)$$

For the TA migration, I use a weighted modified diffraction stack as described by Schlei-

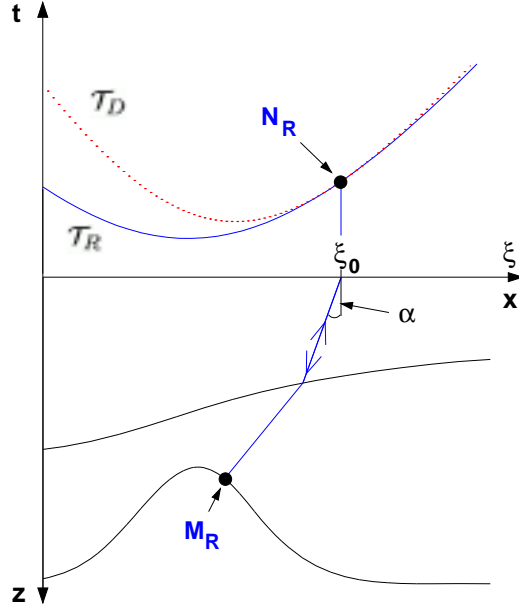


Figure 4.1: The output of the summation along the diffraction traveltime curve  $T_D$  is assigned to the corresponding diffraction point  $M_R$ .

cher et al. (1993). The summation along the diffraction traveltime curve  $T_D$  is mathematically expressed as

$$V(M, t) = \frac{1}{\sqrt{2\pi}} \int_A d\xi W_{DS}(\xi, M) \partial_{t^-}^{1/2} U(\xi, t) \Big|_{t=T_D(\xi, M)}, \quad (4.4)$$

where  $\partial_{t^-}^{1/2} U(\xi, t)$  denotes the anti-causal time half-derivative of the input traces. The partial differentiation has to be performed in order to correctly recover the source pulse. In the absence of noise, the region of integration  $A$  would be ideally the whole  $\xi$ -axis. When noise is present the integral boundaries are given by the projected Fresnel zone as mentioned in Section 2.5 and 3.2.1. Actually, the diffraction stack result does not depend on the time  $t$ . The time-dependency is introduced in order to apply a Fourier transform and to subsequently use the method of stationary phase, Bleistein (1984). The application of this method is possible as  $\omega \gg 1$ , which has already been assumed in the framework of ray theory. Now, the TA weight function  $W_{DS}(\xi, M)$  is going to be determined.

Inserting Equations (4.2) into Equation (4.4) and transforming it into the frequency domain reads

$$\hat{V}(M_R, \omega) = \sqrt{\frac{i\omega}{2\pi}} \hat{F}[\omega] \int_A d\xi W_{DS}(\xi, M_R) \frac{R_c}{L} e^{i\omega T_{dif}}. \quad (4.5)$$

$\hat{F}[\omega]$  and  $\hat{V}(M_R, \omega)$  are the Fourier transforms of  $F[t]$  and  $V(M_R, t)$ , respectively. In Equation (4.5) it is assumed that  $M$  is an actual reflection point, i.e.,  $M = M_R$ . As stated above, the Fourier transform is followed by the method of stationary phase by expanding the phase function  $T_{dif} = T_D - T_R$  into a Taylor series up to second order with respect to  $\xi_0$ , otherwise integral (4.5) cannot be solved analytically:

$$T_{dif}(\xi, M_R) = T_{dif}(\xi_0, M_R) + \frac{1}{2}(\xi - \xi_0)^2 H_{dif}. \quad (4.6)$$

As the diffraction and reflection traveltime curves are tangent at the stationary point  $N_R$ , their gradients are identical. Thus, the first order term of the Taylor expansion is zero. I assume that  $H_{dif}$  is nonsingular. Hence, I do not take any points into account where  $H_{dif} = 0$ . The application of the method of stationary phase in the high-frequency approximation yields

$$\hat{V}(M_R, \omega) \simeq \hat{F}(\omega) W_{DS}(\xi_0, M_R) \frac{R_c}{L} e^{i\omega T_{dif}} \frac{1}{\sqrt{|H_{dif}|}} \cdot e^{-i\frac{\pi}{2}\kappa}, \quad (4.7)$$

where  $\kappa$  is again the KMAH index, Červený (2001). Now, I define

$$W_{DS}(\xi_0, M_R) = L \sqrt{|H_{dif}|} e^{i\frac{\pi}{2}\kappa} \quad (4.8)$$

and insert it into Equation (4.7). It reduces the approximation (4.7) to the spectrum of the TA source wavelet  $R_c \hat{F}[\omega]$  multiplied with a phase shift factor  $e^{i\omega T_{dif}}$  that accounts for the difference between the reflection and diffraction traveltime curve at the stationary point. Going back to the time domain, a comparison with the TA definition (4.3) yields that the geometrical spreading effect is removed, Schleicher et al. (1993). Using equations of Tygel et al. (1995) that describe the relationship of the so-called dual points  $N_R$  and  $M_R$  in Figure 4.1, it can be stated that

$$H_{dif} = \left. \frac{\partial^2 T_{dif}}{\partial \xi^2} \right|_{\xi=\xi_0} = H_P. \quad (4.9)$$

The projected Fresnel zone element  $H_P$  is related to the propagator element  $B$ , Equation (2.32). Insert Equation (2.32) and (2.41) into (4.8) finally yields for the weight function of the 2-D ZO migration

$$W_{DS}(\xi_0, M_R) = \frac{2 \cos \alpha}{v_0}. \quad (4.10)$$

The factor  $\cos \alpha$  vanishes if the vertical component is measured at a non-free surface instead of the principle component. In case of a free surface, the weight function has to be multiplied with a conversion coefficient, Červený (2001). The weight function (4.10) can be used not only for points  $M_R$  but for any arbitrary depth point  $M$  because  $W_{DS}$  does not depend on any reflector properties. Provided the source signal is a function of finite duration,  $F[t]$  vanishes outside an interval  $-T_W < t < T_W$ . If the point  $M$  is close to the reflector, it corresponds to a small traveltime difference  $t = T_{dif}(\xi_0, M)$  inside the interval

$-T_W < t < T_W$ . The value  $R_C F[t]$  is then given by the TA migration. If the point  $M$  moves further away from the reflector, the traveltime difference  $T_{dif}(\xi_0, M)$  moves out of the interval  $-T_W < t < T_W$  and the result of the TA stack practically vanishes, Schleicher et al. (1993).

#### 4.1.1 2.5-D true-amplitude Kirchhoff migration

In the real world, wave propagation always takes place in 3-D. To apply my parsimonious TA migration in Section 4.2 in 3-D, it would require a 3-D CRS Stack with its associated attributes. At present, the 3-D CRS Stack is still under development (at the Geophysical Institute at Karlsruhe University, Germany). Often, geological situations exist which allow to consider 3-D wave propagation in a medium that does not vary in the horizontal direction perpendicular to the seismic line. The stack involved in Kirchhoff migration needs to be performed only along a curve instead of a 3-D data volume. Thus, the diffraction stack integral (4.4) remains the same but the weight function  $W_{DS}$  (4.10) has to be multiplied by the out-of-plane GSF  $\sqrt{\sigma}$  provided by Equation (2.44) or approximated by CRS Stack attributes as in Equation (3.18).

#### 4.1.2 Stationary point

Let me point out a problem that has been mentioned by Schleicher et al. (1997). They wrote: “...there is still the fundamental and unsolved problem of finding a technically feasible method for the determination of the tangency point  $\xi_0$  where the minimum aperture is to be centred”.

The point dual to the tangency point  $N_R$  is the diffractor  $M_R$  located at the normal incidence point (NIP) on the target reflector, Figure 4.1. The  $\xi$ -component of the tangency point is the so-called *stationary point* where the gradients of the reflection and diffraction traveltime curves are identical. A stationary phase analysis concludes that a finite migration aperture results in a migrated image with three components: One comes from the tangency point and gives the migrated signal. The other two components come from the boundaries of the migration aperture and result in migration noise. To obtain a TA migrated section and to suppress migration noise, the migration aperture has to be centred around the stationary point and the input data have to be tapered at the boundary of the migration aperture. The effect of the location of the stationary point, i.e., whether it is within the migration aperture, at the boundary, or outside the migration aperture was extensively examined by Sun (1998) in 2-D and by Sun (2000) in 3-D. The results of Sun (1998) state that the stationary point  $\xi_0$  should lie within the central part of the migration aperture. The central part is determined by

$$|T_{dif}(\xi) - t(\xi_0)| = T_W/2, \quad (4.11)$$

where  $T_W$  denotes the duration length of the seismic pulse and  $\xi_0$  is the stationary point. The traveltime at the stationary point is  $t(\xi_0)$  and  $T_{dif}(\xi) = T_D(\xi) - T_R(\xi)$  is the traveltime difference of the diffracted and reflected signal. The boundary of the migration aperture,

which is equivalent to the boundary of the projected Fresnel zone, is obtained if the right-hand side of Equation (4.11) is multiplied by 2.

Conventional migration methods, post-stack or pre-stack Kirchhoff migration, are based upon a model that consists of point diffractors. Thus, these methods neither contain a specular reflection nor a normal ray. But it is this normal ray in a ZO section that determines the stationary point. By definition, each sample in the simulated ZO section of the CRS Stack is associated with a normal ray. It means, if a sample in the time-domain really corresponds to a reflection event, the stationary point is automatically determined. This not only solves the problem raised by Schleicher et al. (1997). With the CRS Stack attributes it can also be checked whether the stationary point lies within the central part of the migration aperture or beyond it.

For the parsimonious TA migration as well as for the Fresnel CRS Stack, the minimum aperture is centred at the stationary point in order to produce an image with optimal S/N ratio. Katz and Henyey (1992) proposed a method to estimate the stationary point and the minimum aperture. Their approach improved the S/N ratio of the image but relied on a velocity model.

### 4.1.3 Steps of conventional 2-D TA Kirchhoff migration

Conventional 2-D post-stack Kirchhoff migration is performed in the following way, see also Figure 4.2: It is assumed that each point  $M$  at depth is a diffraction point which serves as a secondary Huygens' point source. From each diffraction point  $M$  many rays are traced up to the coincident source and receiver locations along the seismic line. E.g., the traveltime  $t(\xi_A)$  associated with the ray  $(\xi_A M_R \xi_A)$  yields the diffraction traveltime at the ZO coordinate  $\xi_A$ . The diffraction traveltime  $T_D$  is obtained if ray tracing is performed for all ZO locations. Before stacking, the anti-causal time half-derivative of the input traces is computed. The signals aligned along the diffraction traveltime curve  $T_D$  are multiplied by the weight function  $W_{DS}$ , summed, multiplied by  $\Delta\xi/\sqrt{2\pi}$ , and assigned to the point  $M_R$ . Here,  $\Delta\xi$  is the trace spacing which corresponds to  $d\xi$  in the diffraction stack integral (4.4). All points on a depth grid are going to be assigned with stacked signals, which prevents the presence of gaps.

## 4.2 Parsimonious 2-D true-amplitude migration

Before I describe my parsimonious TA migration, I want to point out that recently Hua and McMechan (1999) published another kind of parsimonious 2-D migration. They use local slant stacking to find the emergence angle for an amplitude associated with a plane wave. Afterwards, they shoot the ray down with the known initial angle and distribute the amplitude along the local wavefront which has a radius of curvature proportional to the ray length. Their imaged interfaces look smeared and frayed.

Now, my parsimonious 2-D TA migration is explained by means of Figure 4.3. A simulated ZO section produced by the CRS Stack serves as the input for the migration. The

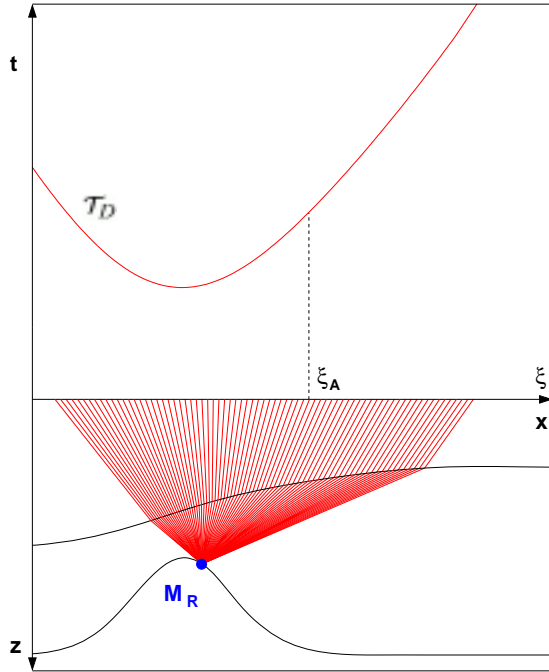


Figure 4.2: Many rays have to be traced in conventional Kirchhoff migration.

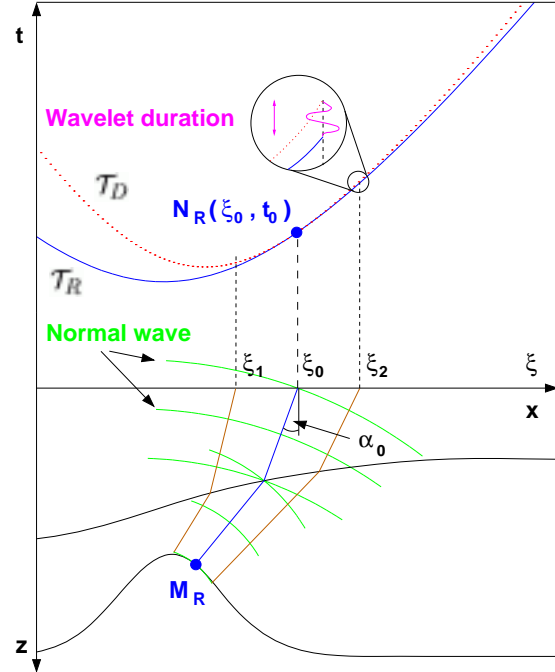


Figure 4.3: A maximum of three rays are traced employing the parsimonious TA migration.

corresponding CRS Stack attributes are used to perform the migration either by stacking or by mapping. A parsimonious 2.5-D TA migration is obtained if the input data set is multiplied by  $\sqrt{\sigma}$  as mentioned in Subsection 4.1.1. The quality of the resulting depth sections is examined using a synthetic data set in Section 4.3. The application to a real data set is shown in Subsection 5.3.4, where the model needed for migration is inverted by means of CRS Stack attributes.

### 4.2.1 Stacking

The diffraction traveltimes curve is computed for each ZO sample with the hyperbolic paraxial traveltimes formula (3.3) by setting  $R_N = R_{NIP}$ . Therefore, no ray tracing is needed to obtain the stacking curve. Because I assume smoothly varying media where paraxial ray theory is valid, the deviations between the analytical diffraction traveltimes curve and the one obtained via ray tracing should be small within the projected Fresnel zone. As described in Subsection 4.1.2, the  $\xi$ -coordinate of a ZO sample in a CRS Stack section is the stationary point. The projected Fresnel zone computed with CRS Stack attributes, Equation (3.12), is centred at the stationary point  $\xi_0$ . The outer vertical dashed lines in Figure 4.3 depict the boundary of the projected Fresnel zone, where the traveltimes difference of the diffracted and reflected traveltimes equals the duration of the wavelet.

The operator  $\partial_{t^-}^{1/2} U(\xi, t)$  is applied to the input traces which are then multiplied by  $W_{DS}$ , stacked within the projected Fresnel zone and multiplied by  $\Delta\xi/\sqrt{2\pi}$ . The ZO data are tapered at the edges of the projected Fresnel zone.

So far, no velocity model was needed. In the next step, one ray is traced through a given macro-velocity model. It starts at the stationary point  $\xi_0$  with a take-off angle  $\alpha_0$ , which is the emergence angle that corresponds to the ZO sample  $N_R(\xi_0, t_0)$ . This (central) ray ends at  $M_R$ , where  $M_R$  coincides with *NIP*. The depth image is somehow discretised. In general,  $M_R$  does not fall onto a grid point. Hence, bilinear interpolation is performed and the stacked signal is distributed to the four nearest grid points, weighted by the distance to the individual grid point. In standard Kirchhoff migration, the interpolation is done, e.g., in the  $(\xi, t)$ -domain. When the rays are traced from  $M_R$  to the ZO locations, the endpoints of the rays do not coincide in general with the ZO locations.

In principle, the parsimonious TA migration is identical to a TA Kirchhoff migration. **The main difference is that the ray tracing is performed for each time sample and not for each depth sample.** Consequently, it is not assured that stacked signals are assigned to each depth sample. This is because rays focus at anticline structures and defocus at syncline structures, which then appear discontinuous in the migrated section. This problem can be overcome by tracing two more rays, namely the paraxial ZO rays which emerge at the boundaries  $\xi_1$  and  $\xi_2$  of the projected Fresnel zone, Figure 4.3. The emergence angles of the paraxial rays differ with respect to  $\alpha$ . Assuming a circular normal wavefront emerging at time  $t_0$  at  $\xi_0$ , the emergence angle  $\alpha_p$  and the traveltimes  $t_p$  for a paraxial point  $\xi$  can be expressed as, Höcht et al. (1999):

$$\sin \alpha_p(\xi) = \frac{\xi - \xi_0 + R_N \sin \alpha_0}{R_N A(\xi)}, \quad (4.12)$$

$$t_p(\xi) = \frac{2}{v_0} R_N [A(\xi) - 1] + t_0, \quad (4.13)$$

where

$$A(\xi) = \sqrt{\frac{(\xi - \xi_0)^2}{R_N^2} + 2 \frac{(\xi - \xi_0) \sin \alpha_0}{R_N} + 1}. \quad (4.14)$$

The normal wave with radius  $R_N$  is propagated along the central ray to *NIP* where it has locally the same curvature as the interface. The intersections of the normal wave at *NIP* with the paraxial rays yield the boundaries of the Fresnel zone at the interface. The latter Fresnel zone differs slightly from the exact interface Fresnel zone because of the approximations made for computing the traveltimes and the emergence angles of the paraxial rays.

The stacked signal is assigned to each point on the interface Fresnel zone, which involves again bilinear interpolation as explained above. When this procedure is done for a whole section, depth points are multiply assigned. This is considered by normalising the value at each depth sample by the number of assignments. Distributing the stacked signal

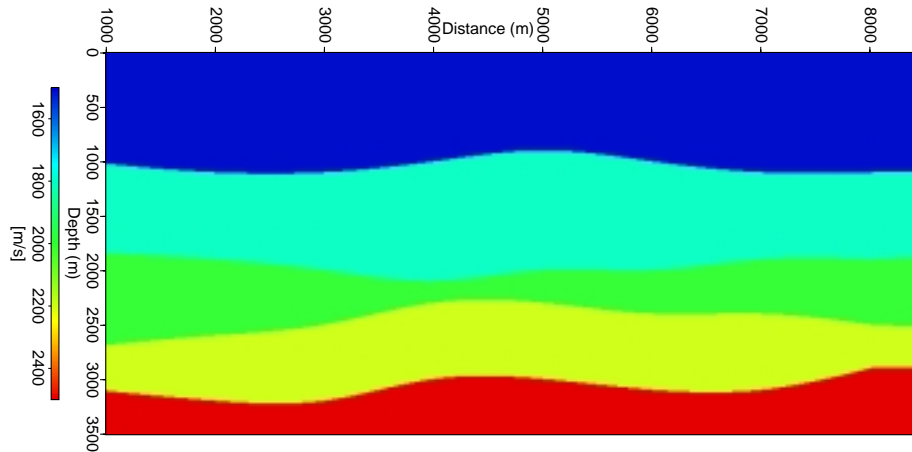


Figure 4.4: Synthetic model made up by five homogeneous layers.

along the interface Fresnel zone fills the gaps. Because the conventional Kirchhoff migration is the basis for the parsimonious TA migration, it belongs to the Kirchhoff-type migration methods.

#### 4.2.2 Mapping

Another approach to produce a TA image is obtained if the stacking is replaced by a multiplication of the ZO traces with the geometrical spreading (3.16). This operation gives the TA signal (4.3), i.e., no additional factor or half-derivative has to be applied. Therefore, the GS corrected signal can be immediately mapped from  $N_R$  to  $M_R$  or assigned along the interface Fresnel zone as described in the previous subsection.

With the term *stack-migrated* section, I refer to the procedure where the data were stacked and then assigned to depth. When the ZO samples are multiplied by the GSF before the depth point assignment, I call it *map-migrated* section.

#### 4.2.3 Data selection via CRS Stack coherence section

For each CRS Stack exists a coherence section. The semblance (see Section 6.3.2) is used for coherence analysis. This section can be used to decrease the amount of data to be migrated. If the ZO sample  $N_R$  in Figure 4.3 was selected, it means that its corresponding CRS Stack attributes are used for migration as described above. Let me emphasise that all samples aligned along the diffraction traveltime curve within the projected Fresnel zone are used for stacking. These samples are used for the stack even if their associated coherence coefficient is smaller than the applied threshold.

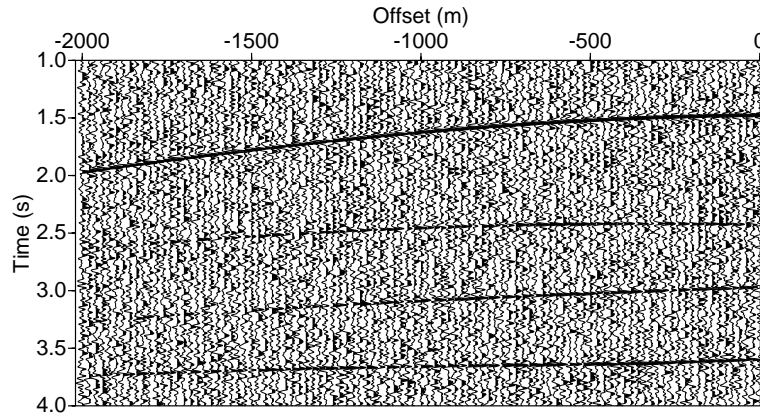


Figure 4.5: Shot gather generated with the NORSAR ray tracer and added noise.

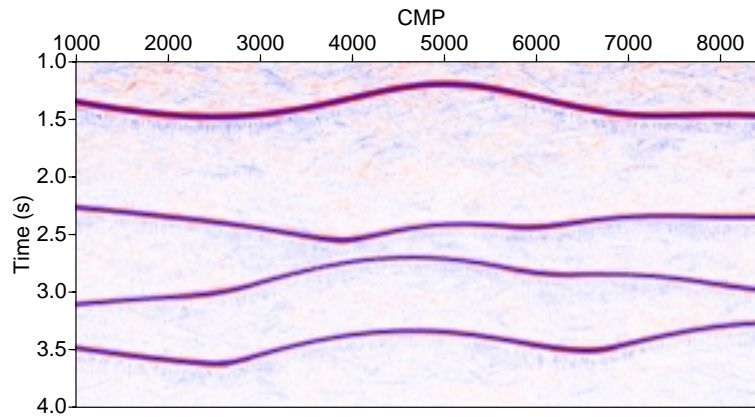


Figure 4.6: Fresnel CRS Stack of the noisy input data set.

### 4.3 Synthetic example

The parsimonious TA migration was tested with a model consisting of five layers with curved interfaces, see Figure 4.4. The layers have from top to bottom a constant P-wave velocity of 1500 m/s, 1800 m/s, 2000 m/s, 2200 m/s, and 2500 m/s. The whole model extends from 0 to 10000 m. The maximum depth of the model is 3500 m. The results are always shown between 1000 and 8500 m. The single-spread data acquisition was as follows: The first shot location was at 1000 m. 142 shot gather were generated each having 101 receivers. The source spacing was 60 m, the receiver spacing 20 m. The receivers were located to the left of the source, i.e., their horizontal  $\xi$ -coordinates were smaller than the  $\xi$ -coordinate of the source. The source moved to the right, thus, the largest offset of 2000 m was first gained when the source was also at the  $\xi$ -coordinate 2000 m. The synthetic data were produced with the NORSAR ray tracer. The source wavelet was a zero-phase Ricker wavelet, i.e., it was the second derivative of the Gaussian distribution curve with

dominant frequency of 20 Hz. The time sampling of the ZO section was 2 ms, the spatial sampling 10 m. In the migrated section the sampling was 5 m in vertical direction and 10 m in horizontal direction. The migration was tested on noise free data and on data where noise was added. A shot gather with noise is shown in Figure 4.5.

### 4.3.1 True-amplitude CRS Stack

The CRS Stack was applied to the synthetic multi-coverage data set in order to produce a simulated ZO section. Before I used this ZO section as the input for the parsimonious TA migration, it has to be ensured, that the CRS Stack did not destroy the amplitudes. Therefore, I compared the amplitudes pertaining to the correct NORSAR ZO rays with the amplitudes of the CRS Stack simulated ZO sections. The Fresnel CRS Stack of the noisy input data set is depicted in Figure 4.6. Each of the four events is clearly visible but from that Figure it cannot be deduced that the dynamics were preserved.

In all the following figures that compare the amplitudes or the RCs, black curves correspond to the first event (interface), red curves to the second, green curves to the third and blue to the fourth event (interface). Figures 4.7 and 4.8 compare the amplitudes of the NORSAR ZO section (solid curves) with the amplitudes of the Initial CRS Stack and Fresnel CRS Stack (dashed curves), respectively. Here, no noise was added to the input data of the CRS stacks. Figures 4.9 and 4.10 are the noisy equivalents to Figures 4.7 and 4.8. It is obvious that the Fresnel CRS Stack recovers the signal better than the Initial CRS Stack. The picked amplitudes of the CRS stacks are always smaller than the NORSAR ZO amplitudes. This is because the amplitude decreases with offset and the reflectivity is angle dependent. As long as the reflection angle is small, the reflectivity decreases with increasing reflection angle. The peaks and troughs in the Figures 4.7 to 4.10 are due to the synclines and anticlines of the interfaces. A syncline (anticline) focuses (defocuses) the reflected wavefield. Thus, the GSF decreases (increases) compared to a GSF associated with a wavefield reflected at a plane interface. Especially, where the influence of the interface curvature is large, the Fresnel CRS Stack recovers the amplitude better than the Initial CRS Stack.

It can be concluded that the deviations of the Initial CRS Stack from the NORSAR ZO section rapidly increase where interface curvatures increase. The deviations are much smaller in the Fresnel CRS Stack. Thus, it should be preferred for a TA migration in comparison to the Initial CRS Stack. From these results it can be deduced that the amplitude of the Fresnel CRS Stack does not change significantly in the paraxial vicinity of the central ray. So far, no explanation could be found for the fact that the deviation of the first interface is larger than for the deeper interfaces.

### 4.3.2 True-amplitude migration

The parsimonious TA migration was applied to the Initial and Fresnel CRS Stack. The parameters associated with the ZO samples within a black strip around the reflection events of Figure 4.11 served as the input for the migration algorithm. Figure 4.12 displays the

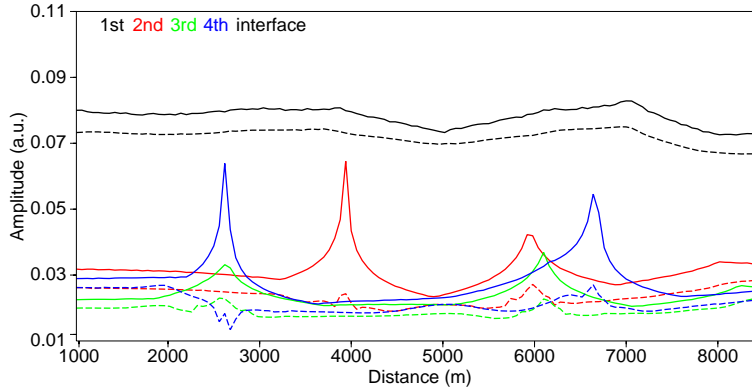


Figure 4.7: Amplitudes of the ZO ray (solid) compared with the amplitudes of the Initial CRS Stack (dashed).

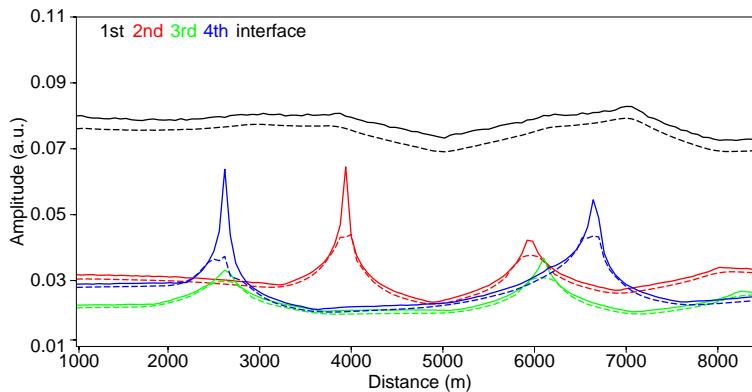


Figure 4.8: Amplitudes of the ZO ray (solid) compared with the amplitudes of the Fresnel CRS Stack (dashed).

migrated section where the noisy data were stacked within the projected Fresnel zone along the diffraction traveltime curve and subsequently assigned to NIP. As described above, due to this special kind of migration, it happens that not all depth points are covered with a migrated signal. These gaps close if the stacked signal is assigned to all depth points along the interface Fresnel zone. This shows Figure 4.13. Here, the input data were noisy, too. Compare the migrated sections with the model 4.4, which was also used for ray tracing. It can be stated that the positions of the reflectors are correct.

Next, I want to check the dynamics of the parsimonious TA migration. The picked amplitudes of the migrated sections are displayed with the same colour code as in the previous subsection. As the reflection coefficients are constant along the interfaces, they appear as straight lines in Figures 4.14 to 4.21. The RCs are computed by  $R = (v_{i+1}\rho_{i+1} - v_i\rho_i) / (v_{i+1}\rho_{i+1} + v_i\rho_i)$ , where  $v$  is the velocity,  $\rho$  is the density of the  $i$ th and  $(i + 1)$ th layer.

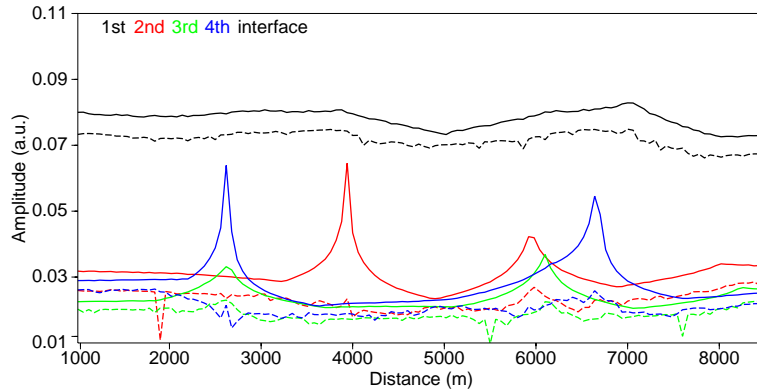


Figure 4.9: Amplitudes of the ZO ray (solid) compared with the amplitudes of the noisy Initial CRS Stack (dashed).

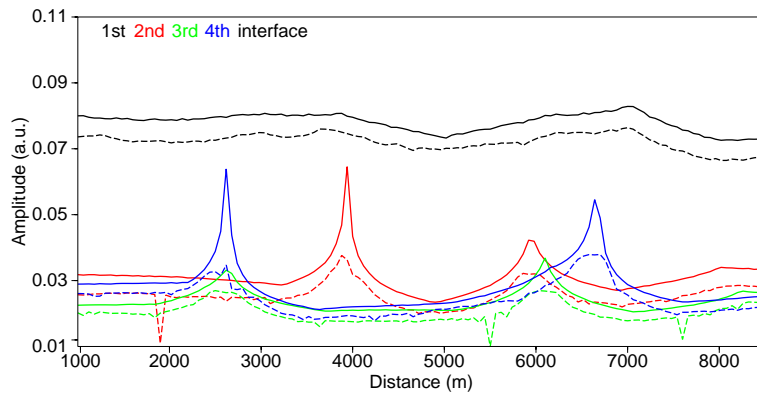


Figure 4.10: Amplitudes of the ZO ray (solid) compared with the amplitudes of the noisy Fresnel CRS Stack (dashed).

I only consider P-waves, thus,  $v$  is the P-wave velocity. The RCs are from top to bottom: 0.091, 0.053, 0.048, and 0.064. For this TA analysis, the data were always assigned to all points along the interface Fresnel zone.

Instead of describing each single figure, I focus on characteristics visible in several figures:

- Amplitudes of the Fresnel CRS Stacks are always closer to the RCs than the amplitudes of the Initial CRS Stacks.
- The amplitude deviations from the RC associated with the first, second, and third interface are always small compared to the fourth interface.
- The fluctuations of the amplitudes along an interface are smaller in the map-migrated

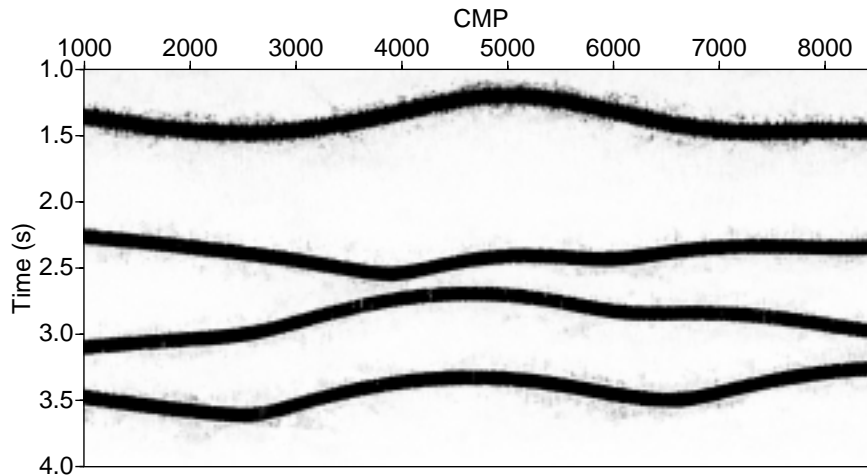


Figure 4.11: Data selection for parsimonious TA migration.

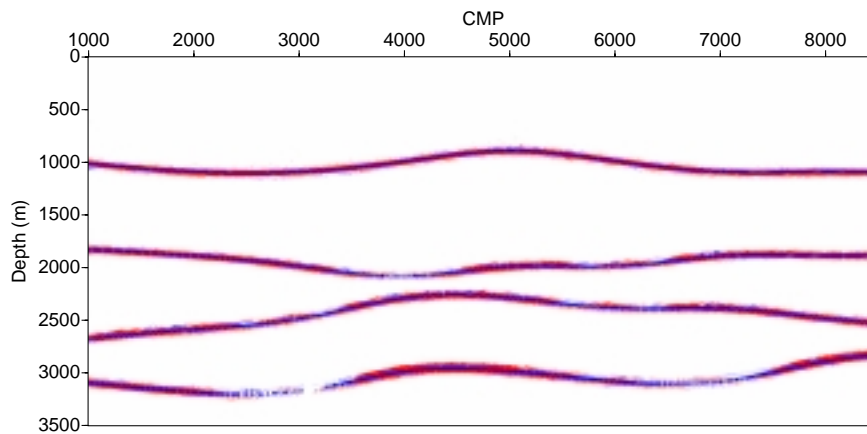


Figure 4.12: Migrated data were merely assigned to NIP.

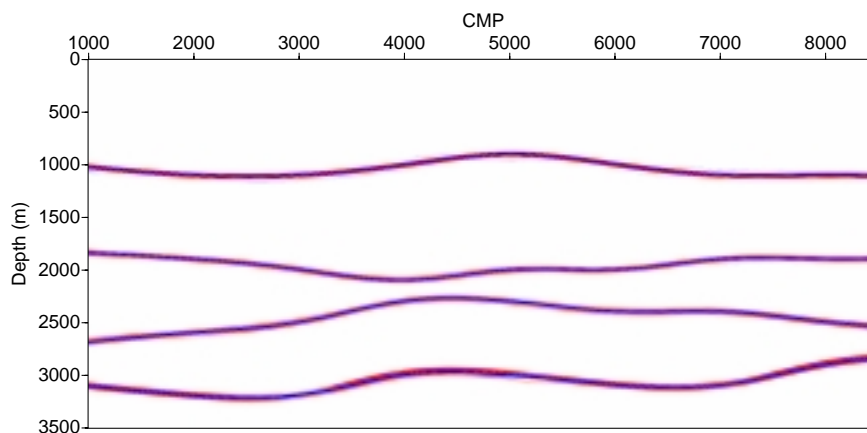


Figure 4.13: Migrated data were assigned to all points along the interface Fresnel zone.

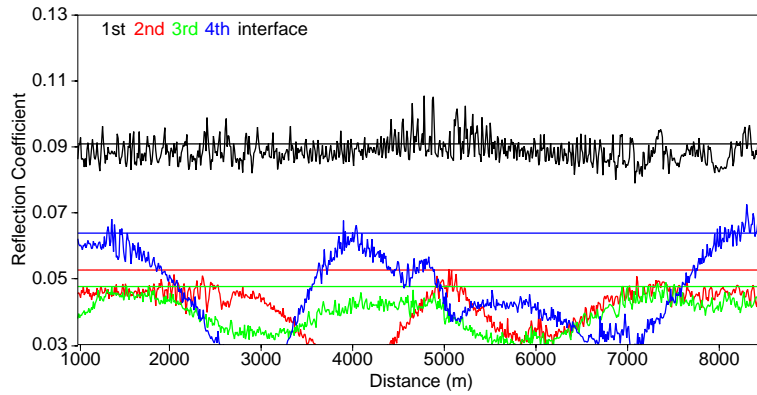


Figure 4.14: Comparison of exact RCs and amplitudes of stack-migrated Initial CRS Stack (noise free).

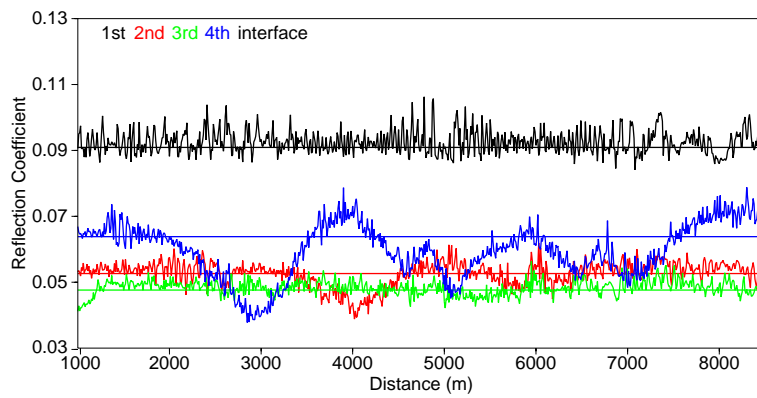


Figure 4.15: Comparison of exact RCs and amplitudes of stack-migrated Fresnel CRS Stack (noise free).

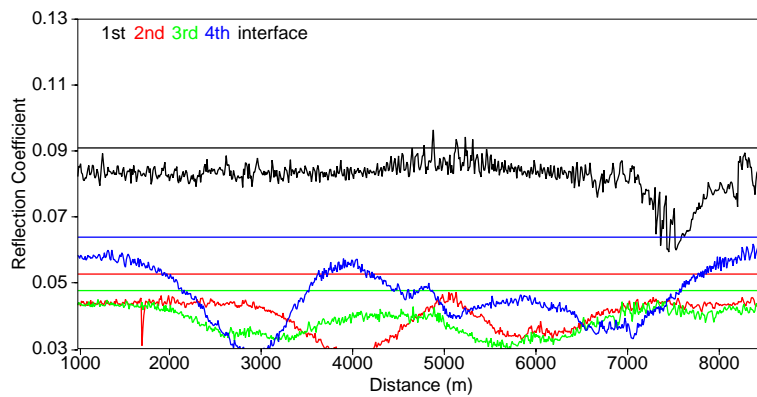


Figure 4.16: Comparison of exact RCs and amplitudes of map-migrated Initial CRS Stack (noise free).

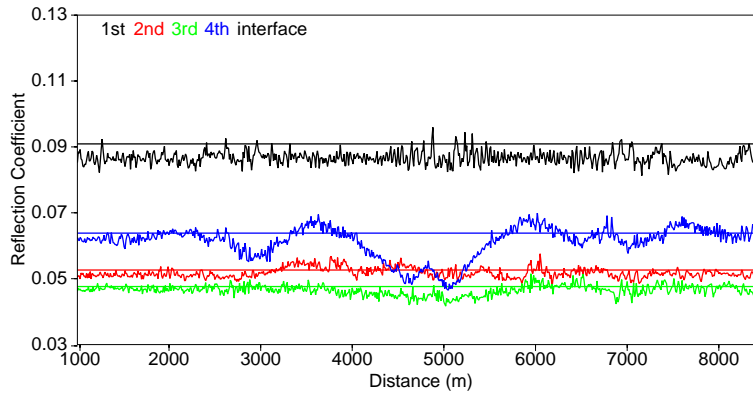


Figure 4.17: Comparison of exact RCs and amplitudes of map-migrated Fresnel CRS Stack (noise free).

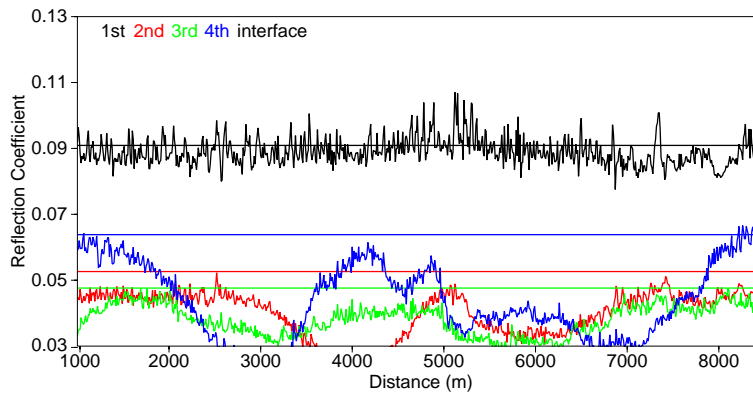


Figure 4.18: Comparison of exact RCs and amplitudes of stack-migrated Initial CRS Stack (with noise).

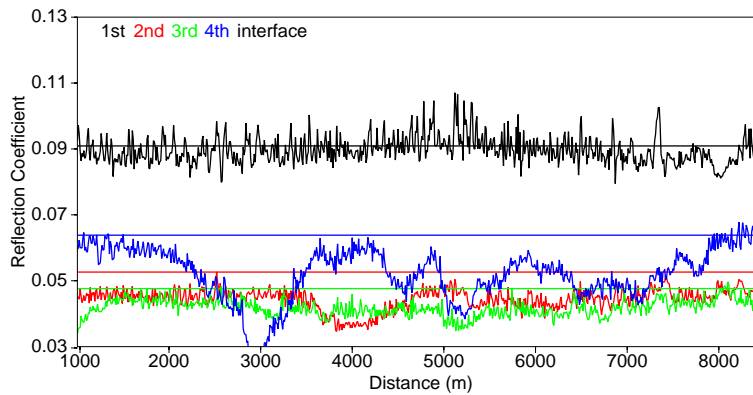


Figure 4.19: Comparison of exact RCs and amplitudes of stack-migrated Fresnel CRS Stack (with noise).

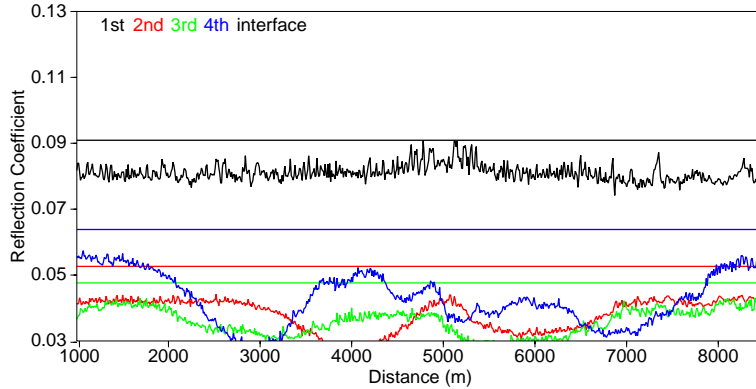


Figure 4.20: Comparison of exact RCs and amplitudes of map-migrated Initial CRS Stack (with noise).

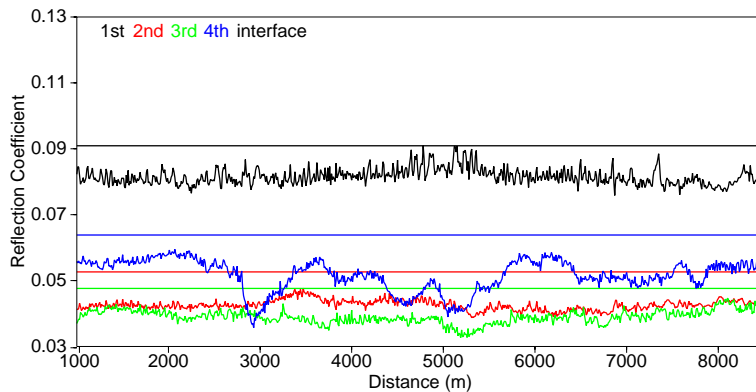


Figure 4.21: Comparison of exact RCs and amplitudes of map-migrated Fresnel CRS Stack (with noise).

sections than in the stack-migrated sections.

- The amplitudes of the map-migrated sections are always smaller than the stack-migrated sections.
- The deviations increase where the interfaces become curved. This was already observable in Figures 4.7 to 4.10.
- The quality of the map-migrated sections is higher than the quality of the stack-migrated sections.

If all data are used for migration instead of the subset selected by a threshold in the semblance section, the results hardly change. In general the deviations slightly increase.

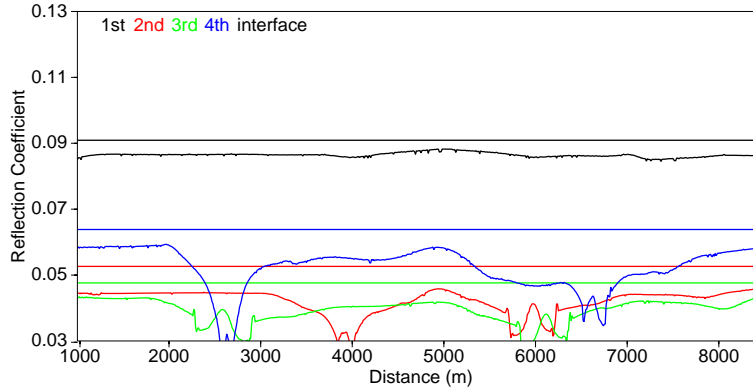


Figure 4.22: Reflection coefficients compared with the GS corrected Initial CRS Stack (no noise).

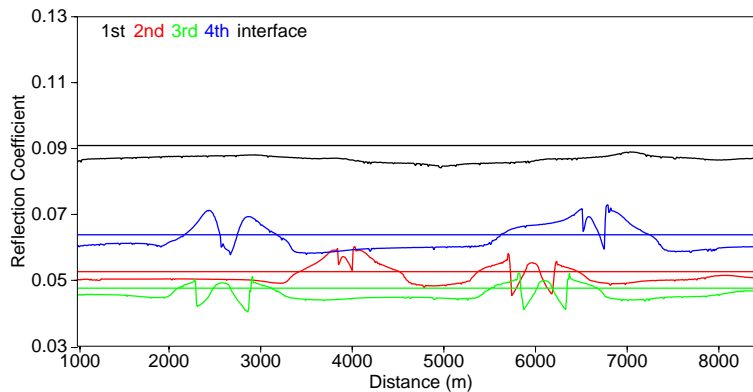


Figure 4.23: Reflection coefficients compared with the GS corrected Fresnel CRS Stack (no noise).

---

### 4.3.3 Geometrical spreading for map migration and as a “natural” gain function

When a simulated ZO section is multiplied by the GSF the data can be map-migrated. It can also serve as a “natural” gain function which displays the reflection coefficients. If the source strength is not known, the section does not show the absolute RC but correct relative amplitudes. Figures 4.22 to 4.25 depict the reflection coefficients as straight lines and the GSF corrected or naturally gained ZO sections. The Fresnel CRS Stacks yield results which are closer to the exact values than the Initial CRS Stacks. The noise introduces high-frequent fluctuations to the curves.

Two phenomena are observable if Figures 4.22 to 4.25 are compared to their migrated equivalents 4.16, 4.17, 4.20, and 4.21: First, there exists virtually no difference in the high-frequent fluctuations of the migrated data with noise and without noise. Second, the

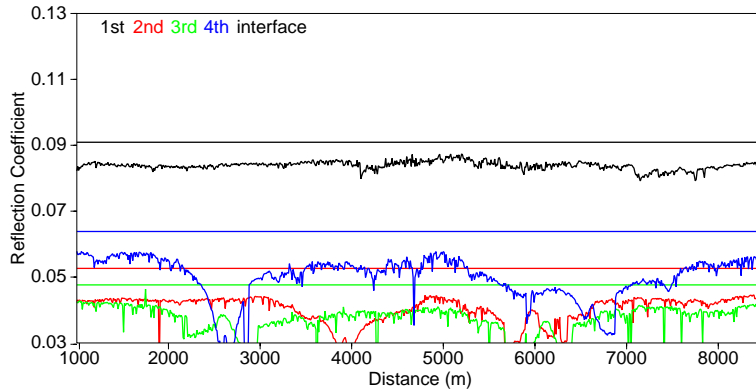


Figure 4.24: Reflection coefficients compared with the GS corrected noisy Initial CRS Stack.

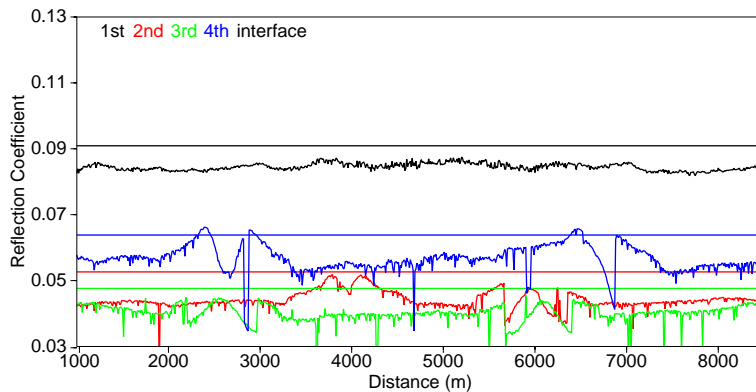


Figure 4.25: Reflection coefficients compared with the GS corrected noisy Fresnel CRS Stack.

W-shaped parts, especially of the second and third event, are flattened in the migrated equivalents. The high-frequent fluctuations were not present in the noise free data in the time domain, hence, they were produced due to the migration process. In addition, the rearrangement of the data due to the transformation from time to depth removes the W-shaped parts.

#### 4.3.4 2.5-D migration

The NORSAR ray tracer also computed the out-of-plane GS. Therefore, all the computations I did for 2-D, were performed for 2.5-D, too. The only difference to the 2-D migration was the computation of the out-of-plane GS using Equation (3.17) and a subsequent multiplication with the ZO sections. For this model the differences are so small that they are not recognisable compared to the 2-D results and are therefore not shown.



## Chapter 5

# Velocity model derived by CRS Stack attributes

The CRS Stack attributes can be employed for the velocity inversion. Various inversion algorithms are described by Majer (2000). He tested the algorithms on synthetic data. My aim was to apply the algorithm also on real data because then the CRS Stack attributes can also be applied to real data to obtain

- a data-driven ZO section,
- a data-driven velocity model, and
- a data-driven parsimonious TA migration.

This means that for the whole cycle of transforming a multi-coverage data set into a depth image, no initial velocity information is required. The inversion process is quite sensitive to fluctuations of the input data. Thus, a smoothing algorithm had to be found which makes the inversion process of real data robust. A short review of the applied inversion algorithm, the sophisticated smoothing algorithm I found, and a real data example is presented in the following sections.

### 5.1 Horizon inversion

From the analysis performed by Majer (2000) it can be deduced that the well-known Dix inversion algorithm (Dix, 1955) is sufficient for gently dipping interfaces but does not yield the best results, especially when the model is complex. The Dix inversion algorithm was translated into a trace by trace inversion, i.e., all information used from several events of one and the same trace is inverted to depth before the next trace enters into the inversion procedure. Thus, the CRS Stack attributes of neighbouring traces have no influence on the inversion process of individual traces. In addition, the Dix inversion algorithm merely requires the NMO velocity of the CRS Stack (Equation 3.6) and does not make use of the full potential of the CRS Stack attributes. This is different in the horizon inversion which I shortly review.

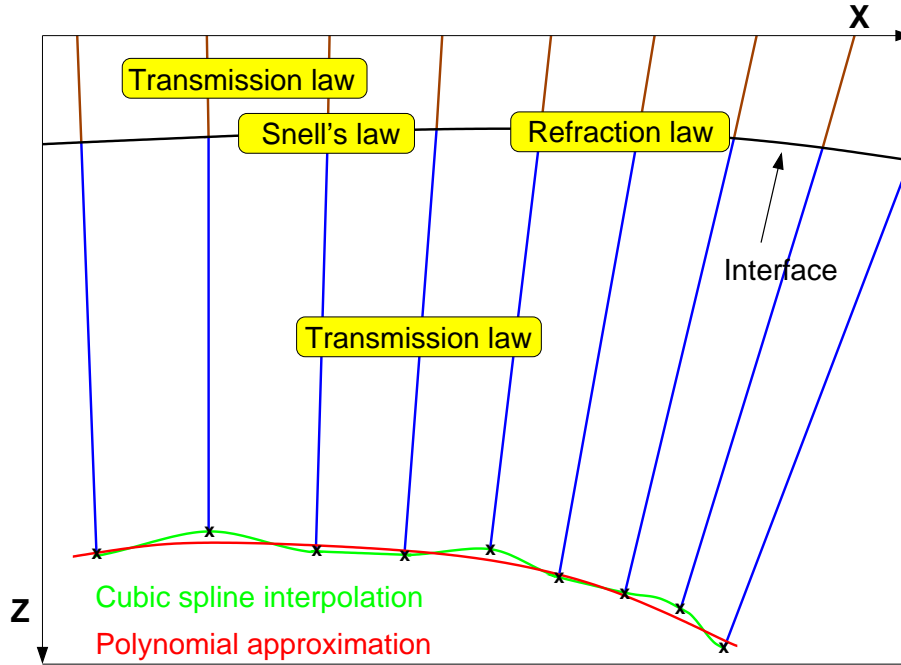


Figure 5.1: The transmission law, Snell's law, and refraction law is required to obtain the refraction angle, the velocity on the refracted side, and the radius of curvature of the refracted wavefront (modified after Majer (2000)).

Three laws are needed for the inversion process. In the following three equations, the index  $I$  is attached to the parameters pertaining to the wavefront or ray incident on the interface, whereas the index  $T$  corresponds to the parameter of the wavefront or ray on the refracted side of the interface, respectively. The *transmission law*

$$R_1 = R_0 + v\Delta t \quad (5.1)$$

describes the change of the wavefront radius  $R_0$  due to the propagation of the wavefront through a homogeneous layer with velocity  $v$ .  $\Delta t$  is the propagation traveltime. The *refraction law*

$$\frac{1}{R_T} = \frac{v_T \cos^2 \gamma_I}{v_I R_I \cos^2 \gamma_T} + \frac{1}{R_F \cos^2 \gamma_T} \left( \frac{v_T}{v_I} \cos \gamma_I - \cos \gamma_T \right). \quad (5.2)$$

yields the radius of the wavefront refracted at the interface with local interface curvature  $1/R_F$ , Hubral and Krey (1980). Here,  $v$  is the layer velocity and  $\gamma$  is the angle measured versus the interface normal at the refraction point. The well-known *Snell's law* is given by

$$\frac{\sin \gamma_I}{v_I} = \frac{\sin \gamma_T}{v_T}. \quad (5.3)$$

Equations (5.3) to (5.2) can be solved for the parameters  $\gamma_T$ ,  $R_T$ , and  $v_T$ . The three parameters on the refracted side are needed for a horizon inversion in a layer-stripping method, i.e., the homogeneous layers are calculated recursively from top to bottom.

Suppose, the ZO traveltimes, the emergence angles, and the radii  $R_{NIP}$  were picked along several events. The horizon inversion starts with the picked data of the first event (smallest traveltimes). The take-off angles of the traced rays are the emergence angles obtained by the CRS Stack. As indicated in Figure 5.1, only the transmission law is needed to obtain the first layer. The endpoints of the rays pertaining to the first layer are connected by a curve which is computed using cubic spline interpolation or polynomial approximation. The difference of how to connect the endpoints, i.e., constructing the interface, is shown at the second interface in Figure 5.1. The cubic spline interpolation passes through all endpoints which produces a strongly fluctuating interface (green). This is not suitable for the inversion of the subsequent interfaces. The polynomial approximation generates a smooth interface with long periodic fluctuations (red).

Next, the rays and NIP-wavefronts of the second event are propagated through the first layer and are refracted at the first constructed interface. At the interface, Snell's law and the refraction law is applied to the rays and NIP-wavefronts. Then the parameters  $\gamma_T$ ,  $R_T$ , and  $v_T$  are computed. Applying again the transmission law yields the blue rays where the endpoints are connected as described above. This procedure is applied to as many events as possible, as long as the fluctuations of the associated attributes can be brought under control.

## 5.2 Robust locally weighted regression

At first, I smoothed the data by means of simple statistical methods, like arithmetic mean, median filtering, triangular weight function combined with the arithmetic mean etc. The outputs were not satisfying in the sense that the algorithm of the horizon inversion either collapsed or produced layered models which were far from being realistic. The robust locally weighted regression of Cleveland (1979) supplied smoothed CRS Stack attributes which ensured a stable horizon inversion.

The first step is to choose a weight function with the following properties:

- $W(x) > 0$  for  $|x| < 1$ ,
- $W(-x) = W(x)$ ,
- $W(x)$  is a non-increasing function for  $x \geq 0$ , and
- $W(x) = 0$  for  $|x| \geq 1$ .

Examples of such a weight function are a boxcar, a triangle or the cosine function (within the boundaries from  $-\pi$  to  $+\pi$ ). The second step is to fit a polynomial of  $d$ th order to the points  $(x_i, y_i)$  within the window using weighted least squares with weights  $w_k(x_i)$ . Specifically, the index  $i = 1, \dots, n$  denotes the sample points of an event where  $n$  is the

number of picked samples. For each  $x_i$ , weights  $w_k(x_i)$  are defined for all  $x_k$ ,  $k = 1, \dots, r$ , using the weight function  $W$ . This is done by centring  $W$  at  $x_i$  and scaling it so that the point at which  $W$  first becomes zero is at the  $r$ th nearest neighbour of  $x_i$ . This yields the initial fitted  $\hat{y}_i$  at each  $x_i$ , which is the locally weighted regression.

In the third step, a different set of weights  $\delta_i$  is defined for each  $(x_i, y_i)$  based on the size of the residual  $(y_i - \hat{y}_i)$ . The robustness weights are defined as

$$\delta_k = B(e_k/6s), \quad (5.4)$$

where  $s$  is the median of  $e_i = |y_i - \hat{y}_i|$  and  $B$  is the bisquare weight function given by

$$\begin{aligned} B(x) &= (1 - x^2)^2, & \text{for } |x| < 1, \\ &= 0, & \text{for } |x| \geq 1. \end{aligned} \quad (5.5)$$

Large residuals result in small weights and small residuals result in large weights. The fitted values are calculated again with a new set of weights  $\delta_i w_k(x_i)$  which are multiplied with the original data. The last step is repeated several times and the result is the robust locally weighted regression.

The number of iterations can be determined. The length of the smoothing window is obtained by  $r = fn$ , where  $r$  is rounded to the nearest integer and  $f$  is a factor between zero and one. If  $f$  is close to zero, the window length for smoothing is short. Thus, the curve of fitted points is characterised by short period fluctuations. In the extreme, if  $f = 1$  all input samples are used for the fit. The robust locally weighted regression was designed to gain the best fit for data for which  $y_i = g(x_i) + \epsilon_i$ , where  $g$  is a smooth function and  $\epsilon_i$  is a random variable with mean zero and constant scale.

## 5.3 Real data example

A subset of the Fresnel CRS Stack of the BEB data set from Chapter 3 served as the input for the picking, smoothing and horizon inversion. The subset is the layered structure on the left side of Figure 3.12, which is displayed enlarged in Figure 5.2.

### 5.3.1 Data picking

The data were picked with a semi-automatic picker which follows the maximum amplitude of an event. If the time increment from one trace to the next exceeds a given threshold, the picker stops. This happens because of the discontinuity of events as, e.g., in box A in Figure 3.12.

The traveltimes of seven events were picked (some are indicated by the arrows in Figure 5.2) which were in a range between 0.3 and 3.2 s. At earlier traveltimes continuous picking was not possible because of the muting in the multi-coverage data set. At later traveltimes the S/N ratio was too small for the continuous picking. With these traveltimes as a reference, the emergence angles and the radius of the NIP-wavefront were extracted from the CRS Stack attribute sections.

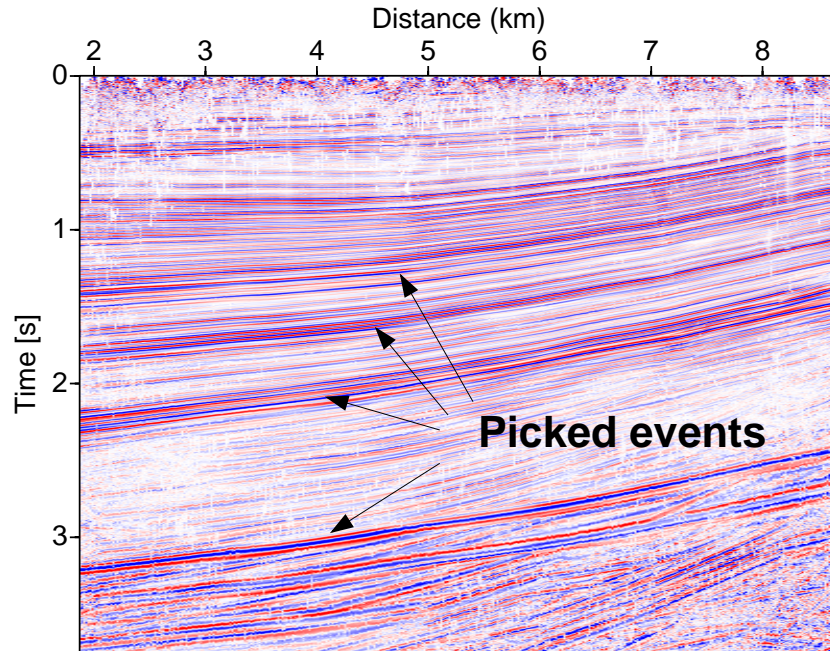


Figure 5.2: The ZO traveltimes were picked along several events in order to extract the associated emergence angle and radius  $R_{NIP}$  which are required to perform the horizon inversion.

### 5.3.2 Data smoothing

The emergence angle and the radius of the NIP-wavefront had to be smoothed for the horizon inversion. For the robust locally weighted regression, the window length was determined by  $f = 0.1$ , the number of iterations was 2. Figures 5.3 and 5.4 depict in red the original emergence angles and radii of the NIP-wavefront, respectively. The blue curve is the output of the arithmetic mean, and the green curve is the smoothed output of the robust locally weighted regression. The original curve of the emergence angles is already quite smooth in the middle of the event, which is different with  $R_{NIP}$ . There the fluctuations at the sides are also larger than in the middle, but in general the values change much more from trace to trace than the emergence angles do. Up to 80% does  $R_{NIP}$  change by moving to the next trace in the middle of the event. The blue curve follows the red curve such that it does not compensate for outliers. If these outliers are not suppressed, the inversion algorithm either breaks down or yields unacceptable results. The green curve is smooth along the whole event in both graphs. Therefore, the robust locally weighted regression eliminates on the one hand outliers and is on the other hand still smooth if the original function strongly fluctuates over many input samples.

### 5.3.3 Velocity model

The horizon inversion was performed as described in Section 5.1. In Figure 5.5, seven interfaces were generated. The layer velocities are in a range of 1.8 and 4 km/s. The

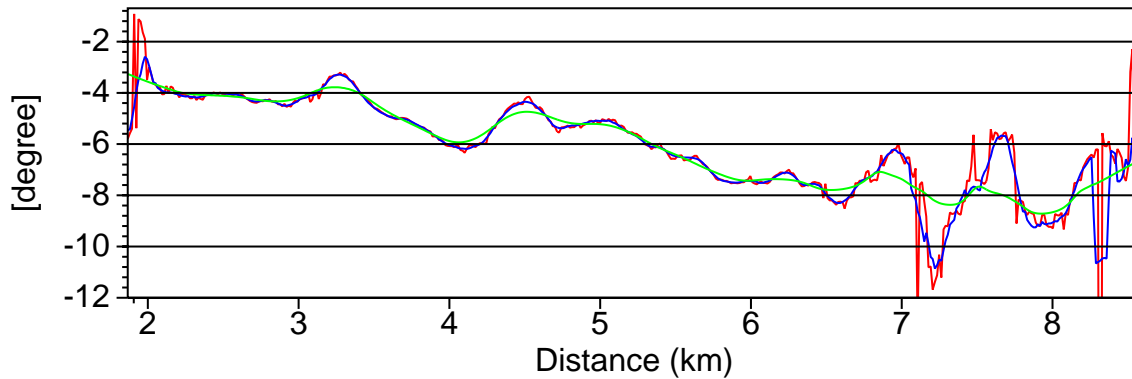


Figure 5.3: Original emergence angles of an event (red), output of the arithmetic mean (blue), and of the robust locally weighted regression (green).

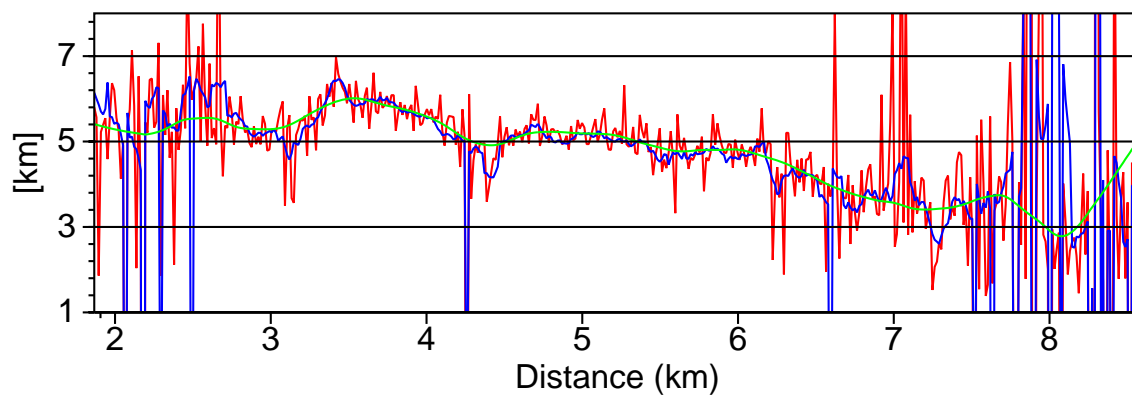


Figure 5.4: Original radius of NIP-wavefront of an event (red), output of the arithmetic mean (blue), and of the robust locally weighted regression (green).

---

velocity model in Figure 5.6 was produced by Geco-Prakla with a NMO/DMO velocity analysis. Their velocities occupy the same range. The velocity distribution in Figure 5.6 is quite similar to the output of the horizon inversion up to about 2.8 km depth. Both types of inversion recover the high velocity zone which is displayed in light blue and light to dark blue, respectively.

I suppose that the amount of time spent for interactive working to produce the velocity model with the horizon inversion is much smaller than during a conventional NMO/DMO analysis. In the horizon inversion the data only have to be picked in the ZO section and smoothed afterwards. In a NMO/DMO velocity analysis one has to select many CMP gathers. Then for a range of velocities, semblance plots are generated. With these semblance plots one has to decide interactively which velocities yield the best alignment of the NMO/DMO operator for the events of the associated CMP gather. This is a time consuming process.

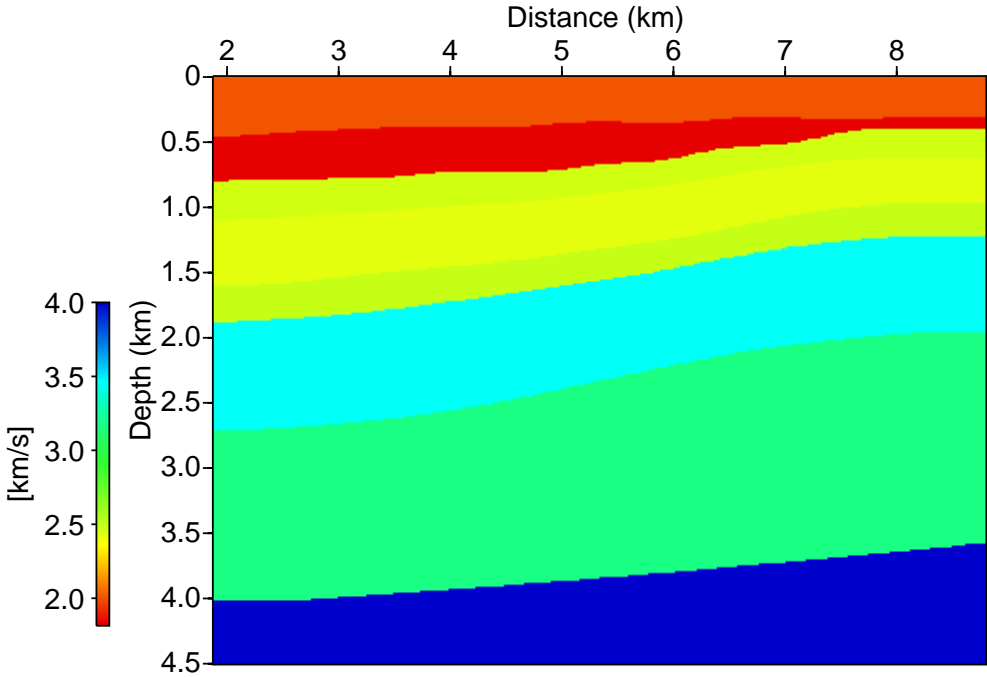


Figure 5.5: Velocity model obtained by means of the horizon inversion.

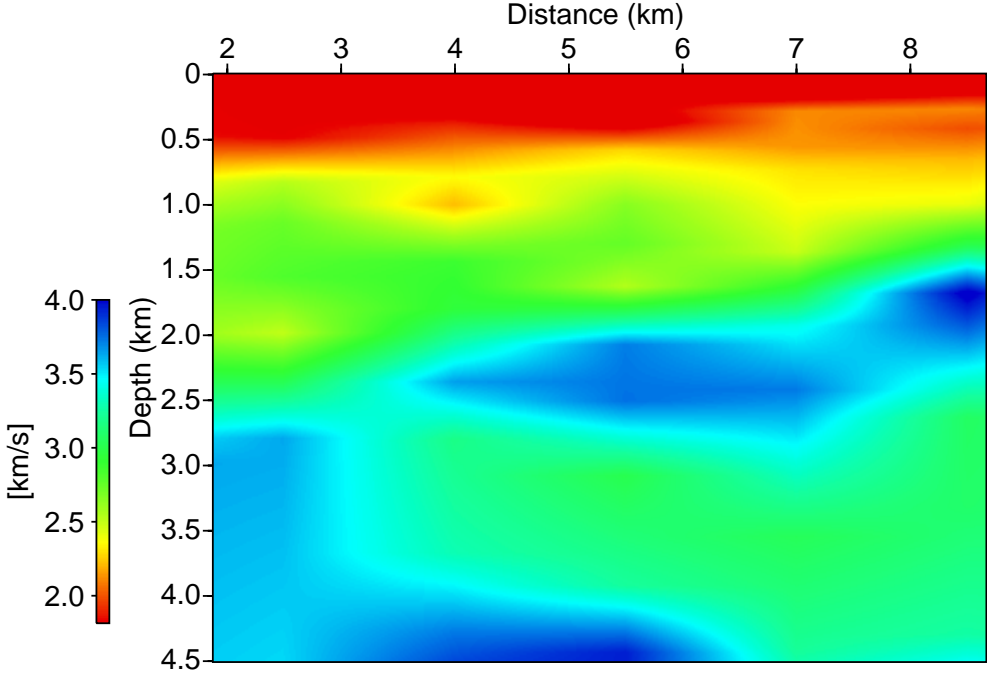


Figure 5.6: Velocity model of Geco-Prakla.

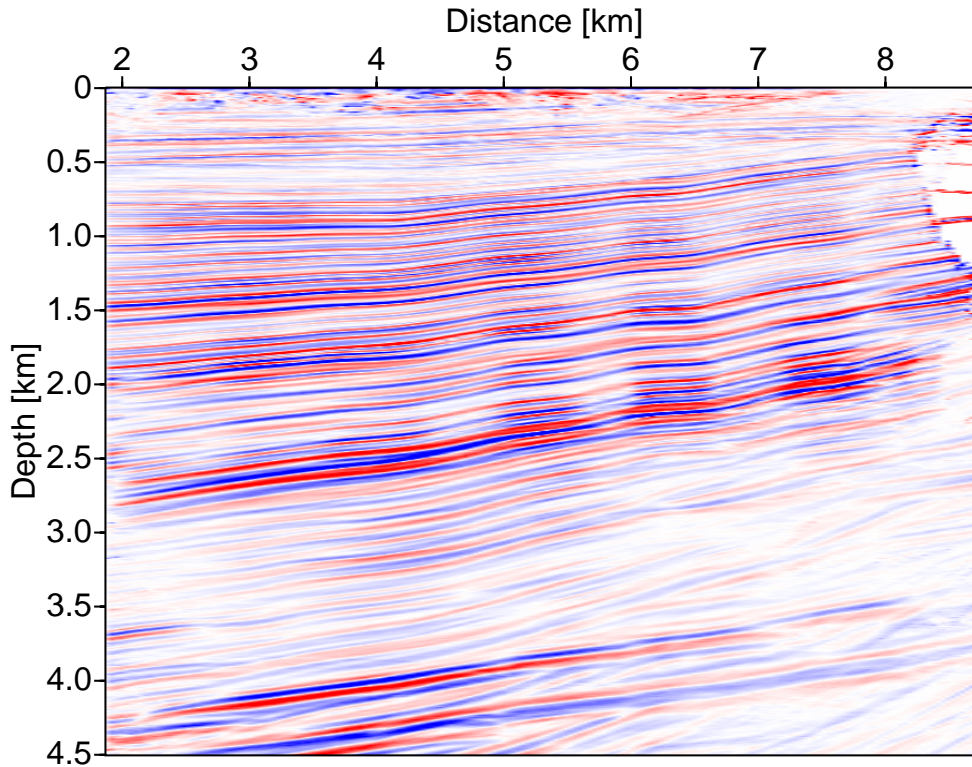


Figure 5.7: Parsimonious 2.5-D TA migration using the layered velocity model.

### 5.3.4 Parsimonious 2.5-D TA migration

The parsimonious TA migration was applied to the subset of the Fresnel CRS Stack depicted in Figure 5.2. First, I multiplied the ZO section with the 2.5-D geometrical spreading factor. Second, the true-amplitude weighted ZO samples were map-migrated to the corresponding interface Fresnel zones. All ZO samples entered the parsimonious TA migration. Hence, no selection by means of the CRS Stack coherence section was done.

The migrated section and the ZO section look similar because the subsurface is a stack of gently dipping layers and gently changing velocities. Therefore, the reflection events do not migrate much. The slightly wavy form of the events in the ZO section appears enhanced in the migrated section. This wavy character can also be observed in the section of the emergence angle 3.14 and in the section of the curvature of the normal wave 3.16. As this effect is visible in the CRS Stack attribute sections, it does not surprise that the amplitude changes along the events. In Section 3.3, I mentioned that a spherical divergence correction using a time and space variant velocity function was applied to the multi-coverage data set. Because of this pre-processing, no matter whether the spherical divergence correction was done properly or not, it is difficult to interpret this kind of amplitude change. Very recently, Herkenhoff et al. (2001) presented data with a simi-

lar amplitude behaviour. His idea was that lense shaped structures focus the wavefield and consequently change the amplitudes. Although, I cannot proof this suggestion on the data from BEB, I reckon it is an idea which one can keep in mind as an option for interpretation. If a ray tracer, like the NORSAR ray tracer, would be available where the CRS Stack attributes could be given as input, the parsimonious TA migration could also be applied to smooth macro-velocity models.

With this example, I presented the applicability of the horizon inversion and the parsimonious TA migration to real data. Of course, improvements are required to apply the algorithms to more complex data. E.g., create blocky velocity models to allow for lateral velocity changes and find solutions to handle gaps in the picked events.



## Chapter 6

# Application of CRS Stack and migration in non-destructive testing

The collaborative research centre (CRC) 381 (*Sonderforschungsbereich 381*) was an opportunity to test the CRS Stack and coherence analysis during migration in non-destructive testing (NDT). The aim of the CRC 381 is to characterise the development of failures. For this, methods are required for the detection of damages, failures, foreign bodies, or cracks within a variety of materials. The sub-project C4 focused at the simulation and mathematical description of wave propagation in random media and at the imaging of cracks in random media. I mainly worked on the latter task but also on the simulation of the wave propagation in random media in order to obtain synthetic data for testing imaging methods (Vieth et al., 1999; Vieth and Shapiro, 1999; Burr et al., 1998).

Kirchhoff migration is also known in non-destructive testing, Langenberg et al. (1993). To my knowledge, the integration of a coherence analysis into migration is a new concept for both NDT and geophysics. For velocity analysis the semblance, see Section 6.3.2, is a common coherence measure in geophysics, but has not been integrated in the process of migration, so far. Up to now, the application of the semblance and the  $\sigma$ -correlation, see Section 6.3.3, was not reported in NDT.

### 6.1 Random media

Concrete is a typical example of an existing random material investigated by an engineering group (sub-project A6) of the CRC 381. Concrete samples were examined with NDT methods for locating cracks or little foreign bodies like polystyrene or metal. Figure 6.1 depicts a synthetic concrete model. The background material shown in light blue is cement, the stuffing material, i.e., gravel of different size is dark blue, and the air inclusions are white. A crack was modelled as an accumulation of many small air inclusions. The physical characteristics of the gravel, cement and air inclusions were determined by their compressional and shear wave velocities  $v_P$ ,  $v_S$  and by the density  $\rho$ . This concrete model was created with the program Medium2D of Burr (1996). The crack can have a certain length and direction but is restricted to the area where cement is present because

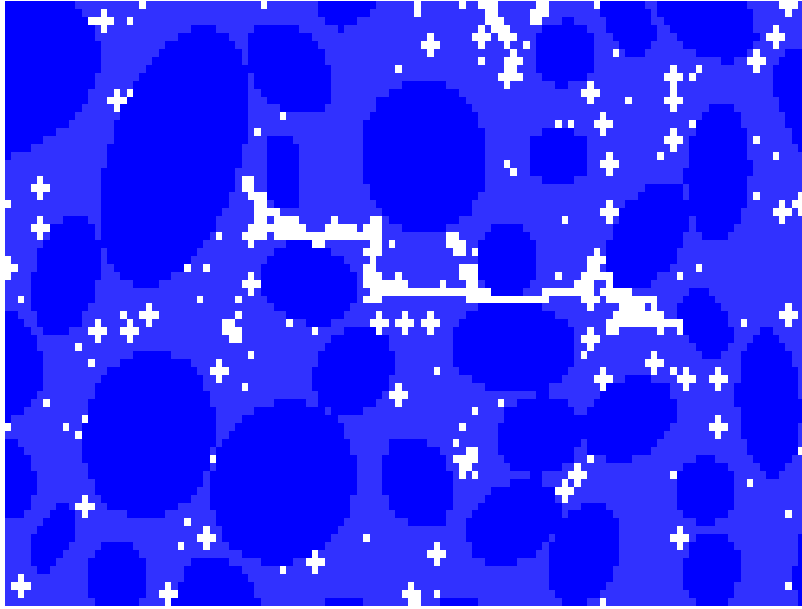


Figure 6.1: Concrete model as a random medium. Dark blue: gravel, light blue: cement, white: air inclusions and crack, respectively.

---

a crack does not go through gravel but stays within the cement.

In Chapter 3 to 5, a layered medium was assumed. The geological equivalent would be homogeneous layers of different sediments. The fine details of the medium were of no interest, thus, the velocity of a subsurface layer is regarded as an effective or homogeneous velocity. Shapiro et al. (1996) describe the effect of random isotropic inhomogeneities on the phase velocity of seismic waves. The effective velocity (average of the phase velocity using a large data basis) depends on the frequency of the source wavelet, the correlation length of velocity and density fluctuations, and on the travelttime distance.

## 6.2 Data acquisition in non-destructive testing

Ultrasonic transducers are used to examine concrete. These piezoelectric transducers are the most common mechanism for converting electrical pulses into elastic waves. The piezoelectric material expands or contracts depending on the polarity of the electric field. Because this mechanism works vice versa, the piezoelectric transducers can be employed as a source and as a receiver.

The coupling of the transducer and the concrete is a big problem for the engineers. Therefore, they prefer to use transducers with large diameters (5 cm and more) in order to make sure that enough energy can be transferred into the concrete. Often, only one or two transducers are used for the data acquisition, i.e., a ZO trace and one offset trace is obtained.

Conventional transducers have to be glued onto the object to be examined which makes the acquisition very time consuming. The “air propagation transducer” is known for a number of years, but only recently began finding useful applications for crack detection. The energy loss due to the large impedance mismatch between air and the solid being inspected can be overcome by increasing the available power. According to Hauffer (2000), this type of transducer is very efficient, in the sense of saving acquisition time. Thus, it might be the right tool to obtain large multi-coverage data sets.

### 6.3 Wavefield attributes and coherence measures for imaging

The (real) wavefield of a random medium at a point  $\xi$  at travelttime  $t$  can be written as, Shapiro et al. (1996):

$$u(\xi, t) = \langle u(\xi, t) \rangle + u_f(\xi, t) , \quad (6.1)$$

where  $\langle u \rangle$  is the coherent field or mean-field and  $u_f$  is the fluctuation of  $u$ , subsequently called the incoherent field. Its mean is  $\langle u_f \rangle = 0$ . The intention is to make use of the mean-field and the fluctuation of  $u$  to better localise a crack or foreign body. The following wavefield attributes and coherency measures were applied either during or after Kirchhoff migration. As mentioned before, Kirchhoff migration is based on a high-frequency approximation and the CRS Stack is based on ray theory which in turn is based on a high-frequency solution of the wave equation. The high-frequency approximation applies to the mean-field associated with the wave propagation in the corresponding homogeneous reference medium (effective medium). Therefore, the CRS Stack and Kirchhoff migration can be utilised for imaging in a random medium. Objects are imaged as long as they are larger than the fluctuations of the medium parameters.

#### 6.3.1 Envelope

The *envelope* is defined as

$$E(\xi, t) = \sqrt{u^2(\xi, t) + v^2(\xi, t)} . \quad (6.2)$$

Here,  $u(\xi, t)$  is the real part and  $v(\xi, t)$  is the imaginary part of the analytic signal. The imaginary part of the recorded (real) signal is computed with the Hilbert transform. The envelope represents the coherent part of the wavefield. Hence, it is used to emphasise the coherent reflection of a crack in a strongly scattering medium. The idea to compute the envelope of a migrated image was published by Simon (1998). There, the data were acquired above crystalline subsurface which possesses a heterogeneous structure similar to concrete.

#### 6.3.2 Semblance and derivative of semblance

In seismics, a widely used coherence function is the *semblance*, Neidell and Taner (1971). The semblance is a cheap coherence measure which yields, according to Mauch (1999)

“best visual interpretable results” and is “best able to enhance weak coherent reflections” compared to other standard coherence measures. The semblance coefficient  $S$  is given by

$$S = \frac{\sum_{j=k-(N/2)}^{k+(N/2)} \left( \sum_{i=1}^M u_{i,j(i)} \right)^2}{M \sum_{j=k-(N/2)}^{k+(N/2)} \sum_{i=1}^M u_{i,j(i)}^2}. \quad (6.3)$$

The number of traces is denoted by  $M$ , the number of samples of the time window equals  $N + 1$ .  $u_{i,j(i)}$  is the sample of the  $i$ th trace and the  $j$ th time increment. The time window is centred around the reference time  $t = k\Delta t$ , where  $\Delta t$  is the sampling interval. The semblance coefficient has a range from 0 to 1, where 1 means that the signal along the reference time does not change at all.

The semblance coefficient is computed during 2-D Kirchhoff migration along the diffraction traveltime curve. The same diffraction traveltime curve is used for stacking. The computed semblance coefficient is assigned to the same depth location where the stacked signal is assigned to. Thus, I obtain a migrated section and a semblance section.

Because of the length of a transient signal, a crack does not appear as a thin line in a semblance section but as an extended region with the crack somewhere inside of it. In order to locate the crack more precisely, I propose to compute the derivative of the semblance in depth direction

$$S_d = \frac{dS}{dz}. \quad (6.4)$$

The onset of the reflected signal, if it is minimum phase, can be detected with  $S_d$  as it is the location where the semblance coefficient changes maximally.

### 6.3.3 $\sigma$ -correlation — a combined phase and group correlation

Standard coherence measures, e.g., (normalised) cross-correlation or semblance, assume that the shape of the signal does not change within the spread of receivers. This is not the case in complex media where the scattering of waves plays a dominant role. The interferential character of a wavefield yields different phase and group velocities. This was shown by Gelchinsky et al. (1985). They pointed out that the group velocity is associated with the large scale structure, whereas the phase velocity corresponds rather to the inner structure of a rugged interface. This observation was extensively confirmed with synthetic and real data by Gelchinsky et al. (1985). In order to obtain a better velocity analysis for complex geologic media, a combined phase and group correlation was given by Gelchinsky et al. (1986).

A narrow-band signal with the amplitude spectral density  $|F(\xi, \omega)|$

$$u(\xi, t) = \frac{1}{\pi} \int_{\omega_0 - \Delta\omega/2}^{\omega_0 + \Delta\omega/2} |F(\xi, \omega)| \cos[\omega t - \alpha(\xi, \omega)] d\omega \quad (6.5)$$

can be represented, using Taylor expansion, in the form

$$\begin{aligned} u(\xi, t) &= f_1[\xi, t - \tau_g(\xi)] \cos \omega_0 [t - \tau_p(\xi)] \\ &- f_2[\xi, t - \tau_g(\xi)] \sin \omega_0 [t - \tau_p(\xi)], \end{aligned} \quad (6.6)$$

where

$$\begin{aligned} f_1(\xi, t) &= |F(\xi, \omega)| \frac{\sin[\Delta\omega [t - \tau_g(\xi)]/2]}{\Delta\omega [t - \tau_g(\xi)]/2} \cdot \frac{\Delta\omega}{2} \\ f_2(\xi, t) &= \left| \frac{dF(\xi, \omega)}{d\omega} \right| \frac{1}{t - \tau_g(\xi)} \left[ \frac{\sin[\Delta\omega [t - \tau_g(\xi)]/2]}{\Delta\omega [t - \tau_g(\xi)]/2} - \cos \frac{\Delta\omega}{2} (t - \tau_g(\xi)) \right] \cdot \frac{\Delta\omega}{2}, \end{aligned} \quad (6.7)$$

with

$$\tau_g = \frac{\partial \alpha(\omega_0, \xi)}{\partial \omega_0} \quad \text{and} \quad \tau_p = \frac{\alpha(\omega_0, \xi)}{\omega_0}. \quad (6.8)$$

$\tau_g$  is regarded as the traveltime corresponding to the wavefront of the wave package or group velocity, respectively, whereas  $\tau_p$  is associated with the traveltime of individual waves of different phase velocities. Those individual waves of different phase velocities make up the wave package.  $\omega_0$  is the dominant frequency of the signal and the width of the signal spectrum  $\Delta\omega$  is assumed to be small in comparison with  $\omega_0$ , i.e.,  $\Delta\omega \ll \omega_0$ . For the phase and group correlation, the signal (6.6) is represented by means of complex terms:

$$u(\xi, t) = E(\xi, t - \tau_g(\xi)) \cos \varphi(\xi, t). \quad (6.9)$$

The first term on the right-hand side is the envelope (6.2) and  $\varphi(\xi, t)$  is the instantaneous phase

$$\varphi(\xi, t) = \Phi(\xi, t - \tau_g(\xi)) + \omega_0 \cdot (t - \tau_p(\xi)). \quad (6.10)$$

It is composed of the slowly varying term  $\Phi$  and a rapidly changing term  $\omega_0 \cdot (t - \tau_p(\xi))$  which is the product of the dominant frequency and the phase traveltime. Insert the functions

$$\begin{aligned} f_1(\xi, t) &= E(\xi, t) \cos \Delta\omega(t) \cdot t \\ f_2(\xi, t) &= E(\xi, t) \sin \Delta\omega(t) \cdot t \end{aligned} \quad (6.11)$$

where

$$\Delta\omega(t) = \omega(t) - \omega_0, \quad \omega = \partial\varphi/\partial t \quad (6.12)$$

into Equation (6.9) yields the signal in the form of the Taylor expansion (6.6).

Now, I introduce a function  $\Psi_{gp}(\xi, \xi_0, t_0, \omega_0)$  which is applied for coherence analysis. The index  $g$  is assigned to the group travelttime and  $p$  to the phase travelttime:

$$\begin{aligned} \Psi_{gp}(\xi, \xi_0, t_0, \omega_0) &= \varphi(\xi, t = t_0 + \Delta\tau_g) - \varphi(\xi_0, t_0) \\ &+ \omega_0 \delta\tau_{gp}(\xi, \xi_0) \end{aligned} \quad (6.13)$$

where

$$\delta\tau_{gp}(\xi, \xi_0) = \Delta\tau_g(\xi, \xi_0) - \Delta\tau_p(\xi, \xi_0) \quad (6.14)$$

and

$$\Delta\tau_k = \tau_k(\xi) - \tau_k(\xi_0), \quad (6.15)$$

with  $k$  representing either  $g$  or  $p$ .  $\Delta\tau_k$  is the travelttime difference of the reflection travelttime curve of two adjacent traces. In order to have a smooth function for coherence analysis I use the cosine of  $\Psi$ . The application of some addition formulae yields:

$$\begin{aligned} \cos [\Psi_{gp}(\xi, \xi_0, t_0, \omega_0)] &= \frac{u(\xi, t_0 + \Delta\tau_g) u(\xi_0, t_0) + v(\xi, t_0 + \Delta\tau_g) v(\xi_0, t_0)}{E(\xi, t_0 + \Delta\tau_g) E(\xi_0, t_0)} \cos(\omega_0 \delta\tau_{gp}) \\ &- \frac{v(\xi, t_0 + \Delta\tau_g) u(\xi_0, t_0) - u(\xi, t_0 + \Delta\tau_g) v(\xi_0, t_0)}{E(\xi, t_0 + \Delta\tau_g) E(\xi_0, t_0)} \sin(\omega_0 \delta\tau_{gp}) \end{aligned} \quad (6.16)$$

where

$$\cos \varphi(\xi, t) = u(\xi, t) / E(\xi, t), \quad \sin \varphi(\xi, t) = v(\xi, t) / E(\xi, t). \quad (6.17)$$

If the time shift due to the difference of the phase velocity and the group velocity is already corrected for, Equation (6.15) is zero. Consequently, the second term of Equation (6.16) is zero and  $\cos(\omega_0 \delta\tau_{gp})$  equals one. Thus,  $\Psi_{gp}(\xi, \xi_0, t_0, \omega_0) = \Delta\varphi(\xi, \xi_0, t_0) = \varphi(\xi, t = t_0 + \Delta\tau_g) - \varphi(\xi_0, t_0)$ . The function  $\Delta\varphi(\xi, \xi_0, t_0)$  only depends on the group velocity and enters now into the so-called  $\sigma$ -correlation.

### 6.3.3.1 $\sigma$ -correlation

For every trace  $n$ , ( $n = 1, \dots, N$ ), the following functions are computed within a time window of  $2M + 1$  samples with a sample interval of  $\Delta t$ :

$$\cos \Delta\varphi_n(\xi_n, \xi_0, t_0) = \cos [\varphi_0(\xi_0, t_0) - \varphi_n(\xi_n, t_0 + \Delta\tau_n(\xi_n, \xi_0))] \quad (6.18)$$

$$\overline{\cos \Delta\varphi_n(\xi_n, \xi_0, t_0)} = \frac{1}{2M+1} \sum_{m=-M}^M \cos \Delta\varphi_n(\xi_n, \xi_0, t_0 + m\Delta t) \quad (6.19)$$

$$\sigma_n^2(\xi_n, \xi_0, t_0) = \frac{1}{2M} \sum_{m=-M}^M [\cos \Delta\varphi_n(\xi_n, \xi_0, t_0 + m\Delta t) - \overline{\cos \Delta\varphi_n(\xi_n, \xi_0, t_0)}]^2. \quad (6.20)$$

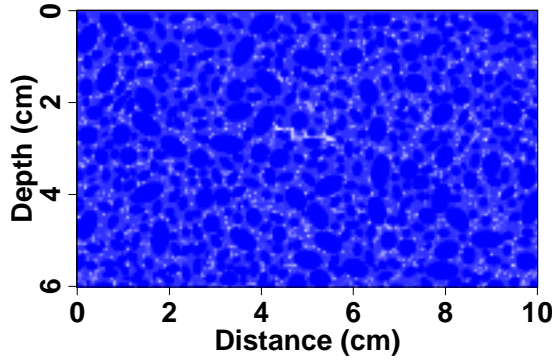


Figure 6.2: A part (10x6cm) of the crack-model.

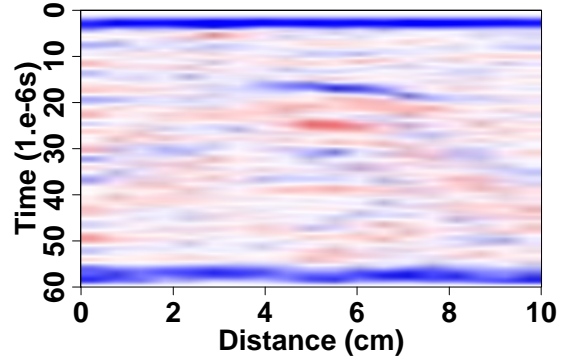


Figure 6.3: Plane wave response of the crack-model.

Equation (6.18) is equivalent to Equation (6.16) for  $\delta\tau_{gp} = 0$ . The sample average is given by Equation (6.19) and the sample variance by Equation (6.20). The value  $\Delta\tau_n(\xi_n, \xi_0)$  which minimises the value of  $\sigma_n^2$  defines the group time shift  $\Delta\tau_g(\xi_n, \xi_0)$ . For a multichannel procedure, the following function is used

$$\sigma^2(\xi_0, t_0) = \frac{1}{N} \sum_{n=1}^N \sigma_n^2(\xi_n, \xi_0, t_0), \quad (6.21)$$

which is the final equation used for  $\sigma$ -correlation.

## 6.4 Migration and correlation

Several models and the corresponding synthetic seismograms were produced in order to examine which wavefield attributes and correlation algorithms are successful in combination with Kirchhoff migration. The results for two concrete models with different types of inclusions are exemplarily presented. The first kind of inclusion is a crack, the second kind is a foreign body. Both types are often the focus for investigations made on concrete. Thus, the question is: Is it possible to detect and determine the correct location of a crack or a foreign body within a random medium like concrete?

### 6.4.1 Crack-model

The first model is the crack-model. Figure 6.2 shows a part of the model with a width of 10 cm and a depth of 6 cm (actual depth is 10 cm). The following technical informations correspond to a typical type of concrete in civil engineering. The ellipses which represent gravel of different sizes make up 50 % of the overall area. The gravel has a P-velocity of 4.03 km/s, a density of 2.59 g/cm<sup>3</sup>, and a standard P/S-ratio of  $\sqrt{3}$ . The background material, i.e. the cement, has a P-velocity of 3.95 km/s, a density of 2.17 g/cm<sup>3</sup> and also a P/S-ratio of  $\sqrt{3}$ . The model has a porosity of 4 %, i.e., 4 % of the area is covered by air

inclusions. The area of the crack is about  $8 \text{ mm}^2$ .

In Chapter 2, I mentioned that ray tracing is suitable for smoothly varying media whereas FD schemes are suitable for wave propagation in a heterogeneous medium. Witte et al. (1996) examined kinematic ray tracing in random media and supply the explanation why the synthetic seismograms were not computed with ray tracing as in the previous chapters but with FD. They conclude that it “only gives correct first-arrival traveltimes for sufficiently weak and smooth velocity fluctuations and for sufficiently short travelpaths”. Another result is that “in spite of very dense ray fields, the ray-tracing traveltimes show pronounced short-scale variations with distance. The reason is that ray tracing disregards diffracted rays and the associated wavefront healing”. The wavefront healing process obtained by FD computation is displayed in Figure 6.4 (for more comments on the snapshots see below).

The finite-difference program ULTIMOD of Karrenbach (1995) was used to compute the propagation of a plane wave through the model. In order to handle high contrasts, the computations in ULTIMOD are performed on a rotated staggered grid Saenger et al. (2000). A minimum phase Ricker-wavelet (first derivative of the Gaussian distribution curve) served as a source signal. The source was modelled as a body-force with a direction perpendicular to the top (depth = 0 cm) of the model. Its fundamental frequency was 300 kHz, whereas the maximum frequency was 500 kHz. The plane wave response is depicted in Figure 6.3, where blue (red) denotes a positive (negative) amplitude and white corresponds to the zero-crossing of the signal. This colour code is the same for all seismograms, snapshots, or depth images. There the z-component, i.e., perpendicular to the top of the model was measured. The two-way traveltime of the reflection of the crack is about  $16 \mu\text{s}$ . The blue horizontal event at the top of Figure 6.3 exists because sources and receivers are located at the same position in a thin (1.6 mm) homogeneous layer of cement. The first lobe of the minimum phase wavelet can be measured nearly undisturbed. The second part of the signal, i.e., the negative amplitude, is already strongly distorted because of scattering and interference with reflections from the top of the model. The model was surrounded by an air layer of 4 mm to obtain a free surface.

Different observations can be made in Figure 6.3: (a) the seismogram looks wavy, frayed and changes smoothly. (b) the amplitude of the back-echo, i.e., the reflection from the bottom of the model, is about as strong as the reflection of the crack. (c) lots of diagonal reflections are present. These phenomena can be explained with the six snapshots shown in Figure 6.4 with a time increment of  $2.1 \mu\text{s}$  beginning at  $6.3 \mu\text{s}$ . The scattering at the air inclusions and the scattering and reflection at the gravel produces from the beginning on, Figure 6.4 (a), a wavefield that changes its phase smoothly laterally and vertically. The plane wave is not plane anymore but turns into a wavy line. As the wavefront passes the crack, two phenomena can be observed: (i) a part of the plane wave is reflected back to the surface and (ii) the wavefront heals on its way down. Thus, it is nearly plane when it hits the lower side of the model. The diagonal reflections are due to critical reflections that generate head waves at the sides of the model. The head waves propagate such that they arrive at the receiver a little after the reflection from the crack arrives at the top.

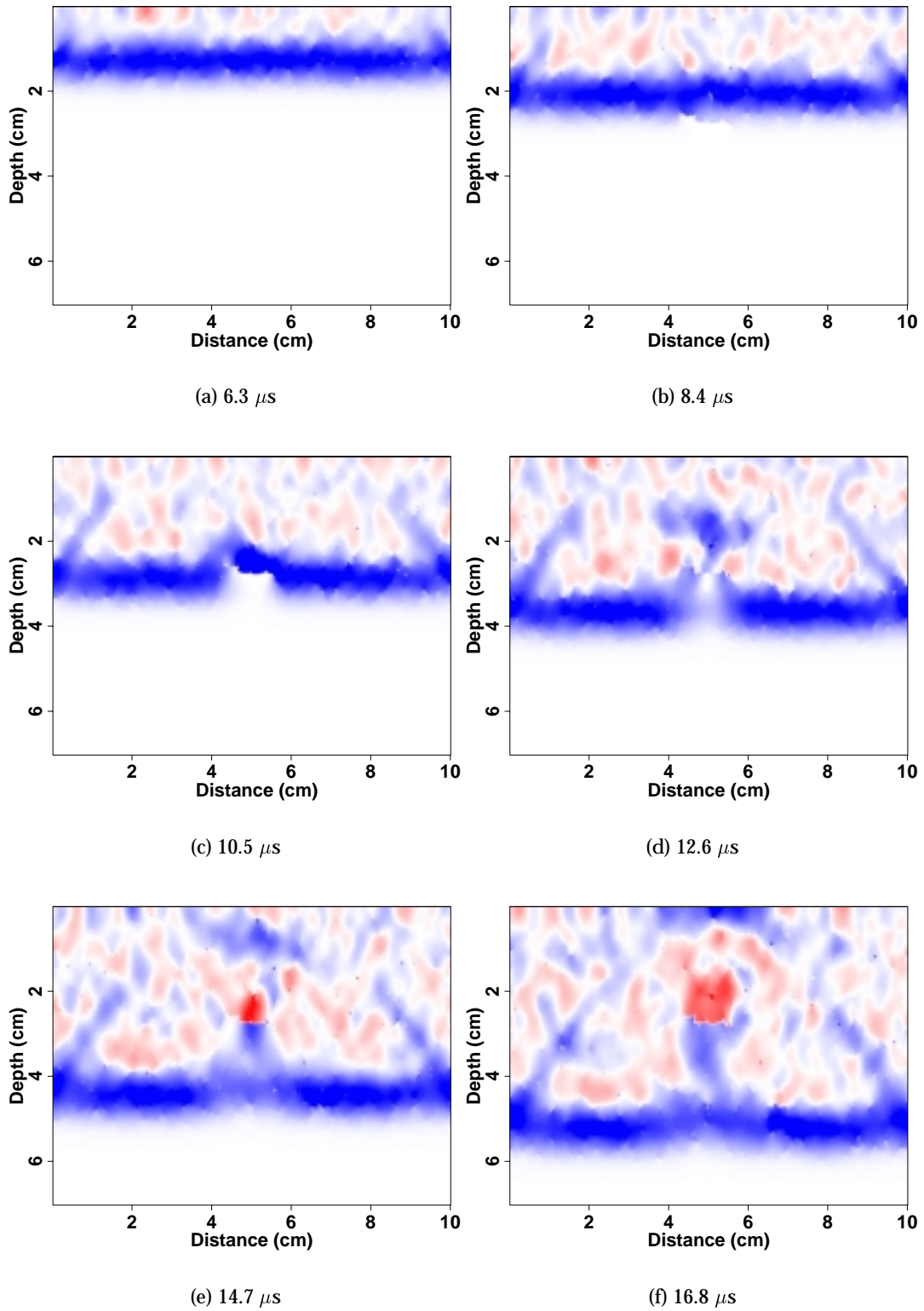


Figure 6.4: Six snapshots of the plane wave propagation.

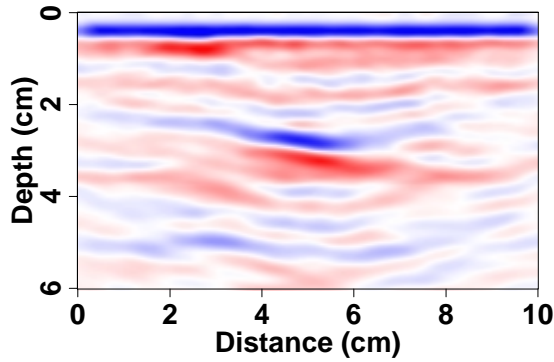


Figure 6.5: Constant velocity migration of the ZO section of Figure 6.3.

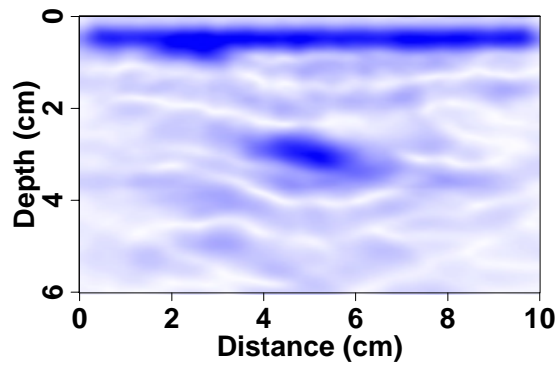


Figure 6.6: Envelope of the image, Figure 6.5.

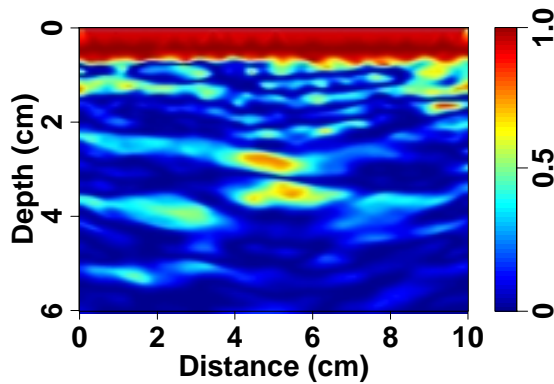


Figure 6.7: Semblance section computed during migration.

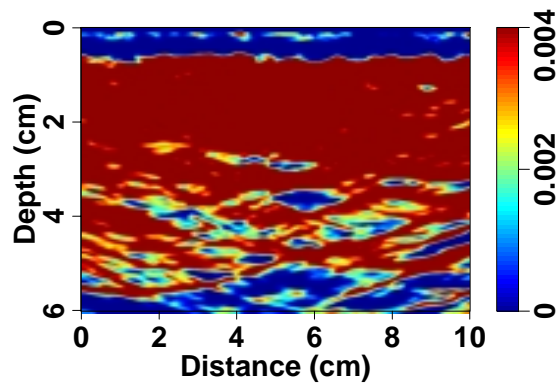


Figure 6.8:  $\sigma$ -correlation computed during migration.

These head waves correspond to the events, which occur immediately after source initiation, in the upper left and right corner and dip towards the crack reflection in the middle of Figure 6.3.

The effective velocity of, e.g., a concrete block is often determined by performing many transmission experiments. A pulse is excited by an ultrasonic transducer on one side and the signal is measured by another ultrasonic transducer on the other side of the concrete block. The first arrivals have to be picked and averaged. The traveltime distance, which is known, has to be divided by the average traveltime of many experiments, which yields the effective velocity  $v_{eff}$ . For constant velocity migration,  $v_{eff}$  is used.

In this experiment sources and receivers were placed on the same side. Thus, the back-echo serves as a reference to determine the effective velocity. For this model the effective velocity is  $v_{eff} = 3500$  m/s.

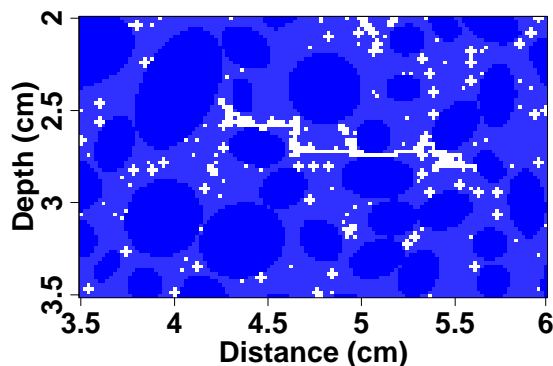


Figure 6.9: Magnification of the crack region of the model.

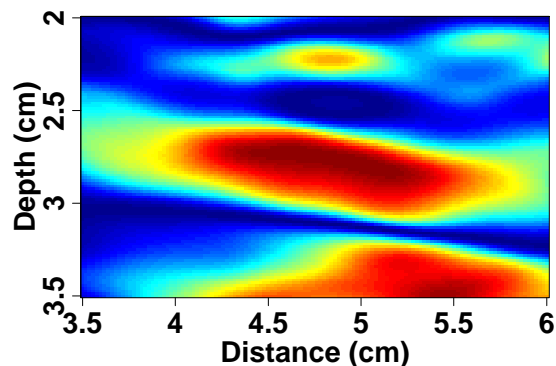


Figure 6.10: Magnification of the crack region of the semblance section.

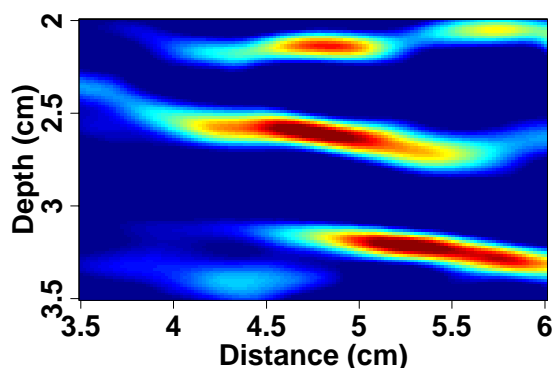


Figure 6.11: Magnification of the crack region of the section of the semblance-derivative.

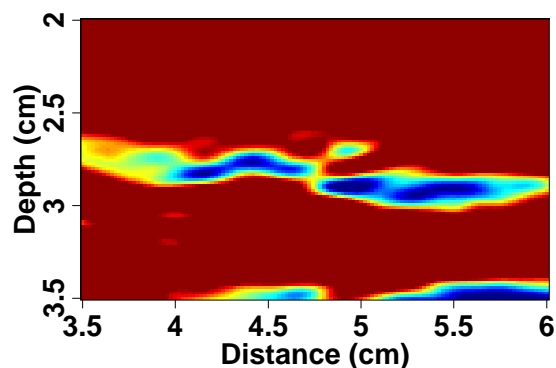


Figure 6.12: Magnification of the crack region of the  $\sigma$  section.

The image in Figure 6.5 was obtained using the Kirchhoff-migration integral (4.4) with the constant velocity  $v_{eff}$ . The steeply dipping events are not visible anymore because they correspond to the vertical sides of the model. The crack appears enhanced but it is difficult to define where it starts and ends in lateral direction. The slight dip of the crack is migrated correctly. The envelope of the image, Figure 6.6, improves the S/N ratio. Thus, the crack is even more pronounced and it is laterally better restricted. Figure 6.7 is the semblance section. A window width of  $0.23 \mu s$  was applied in time direction. In the semblance section, the crack is associated with the first big spot having a semblance coefficient close to 1. The second spot below corresponds to the negative amplitude of the Ricker source wavelet.

The time window for the  $\sigma$ -correlation was  $0.86 \mu s$ . The phase traveltimes were defined as  $\tau_p(\xi) = \tau_g(\xi) + \Delta t \cdot n$ , where  $\Delta t$  is the sampling rate and  $n$  is an integer that varied from -10 to +10. To compute the  $\sigma$ -correlation, Figure 6.8, it takes about 100 times more than to compute the semblance section. The result is not as clear as it is in the semblance section.

Please remember that a small  $\sigma$  coefficient is related to a coherent signal and a large  $\sigma$  coefficient is associated with an incoherent signal. The crack is depicted by small values. In the semblance section there appears coherent energy mainly above the crack whereas it is mainly below the crack in the  $\sigma$  section.

For a better evaluation, I zoomed into the model, Figure 6.9, the semblance section, Figure 6.10, the section of the semblance-derivative, Figure 6.11, and the  $\sigma$  section, Figure 6.12.

Because the source wavelet was minimum phase, the onset of the reflection marks the location of the crack. The S/N ratio is small at the onset of the reflection event and increases, at first quickly and then slower, up to the maximum amplitude location. This can be seen in the semblance section 6.10. Therefore, the exact position of the crack is obtained by the semblance-derivative because the maximal vertical change of the semblance, i.e., the change between incoherent and coherent energy, is due to the rapid increase of the amplitude of the source wavelet. Negative values in Figure 6.11 are set to zero as only the increase of the semblance is of interest. Due to the derivative the crack is not only confined vertically but also laterally.

The magnification of the  $\sigma$  section, Figure 6.12, shows the coherent region at the same position as in the semblance section. Though, the section seems to have a better resolution, it is not possible to confine the lateral extent more precisely than in Figure 6.11, which is the best result.

### 6.4.2 Poly-model

The poly-model is displayed in Figure 6.13. The white rectangular inclusions represent polystyrene. This model was also built by the sub-project A6 of the CRC 381. The intention was to model a laboratory experiment and to compare theory and experiment. Unfortunately, up to now no laboratory data are available. The poly-model has a size of  $35 \times 10$  cm. The physical parameters of the cement and the gravel are equivalent to the crack-model of Section 6.4.1 but here, 8 % of the area is covered by air inclusions. This porosity value was determined by the sub-project A6 of the CRC 381. The data acquisition is equivalent to the crack-model experiment. The size of the polystyrene is  $5 \times 1$  cm. It is a type of plastic with a density of  $1.05 \text{ g/cm}^3$  a P-velocity of  $2.35 \text{ km/s}$ , and a S-velocity of  $1.45 \text{ km/s}$ . The top of the left (right) polystyrene area is at a depth of 4.5 cm (3 cm). The left side of the left (right) polystyrene area is at a distance of 10 cm (24 cm).

The plane wave response of the model is depicted in Figure 6.14. The source wavelet was the same as for the crack-model. The first reflection on the left and right correspond to the top of the polystyrene. The second event with opposite phase is associated with the bottom of the polystyrene. The horizontal event on the right at about  $45 \mu\text{s}$  can be explained by the following propagation path: Transmission of the plane wave into the polystyrene, reflection at the bottom, reflection at the top, again a reflection at the bottom, and finally a transmission through the top of the polystyrene. The back-echo is not plane as in the

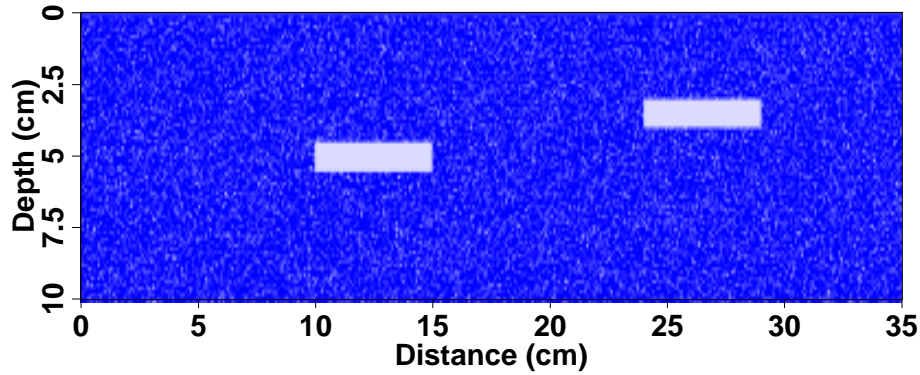


Figure 6.13: Poly-model with two polystyrene areas.

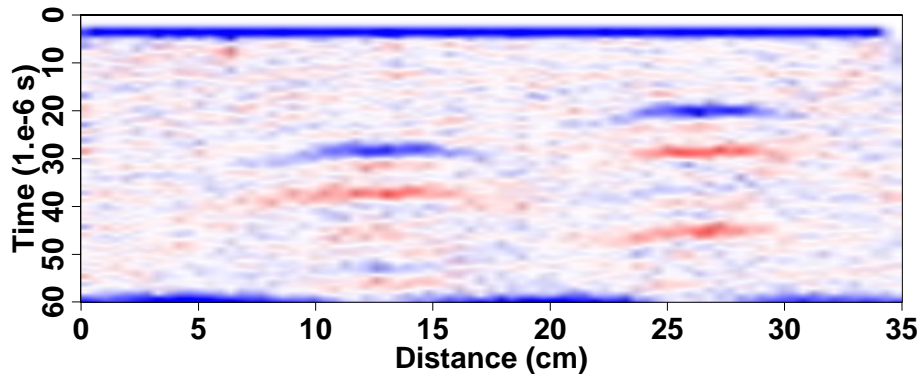


Figure 6.14: Plane wave response of the poly-model.

crack-model because the influence of the polystyrene areas on the wave healing process is too large. Again, head waves are visible but do not appear as dominant as in Figure 6.3, which is due to the better S/N ratio of the reflection events. Here, the effective velocity is 3400 m/s, which is 100 m/s slower than in the crack-model. The migrated section in Figure 6.15 shows the top and bottom of the polystyrene with opposite sign. The S/N ratio is already quite good, hence, I do not show the envelope of the image because it does not improve much compared to the image. The lateral confinements could be more distinct in the image. In the semblance section, Figure 6.16, those confinements improved. The time window used to determine the semblance coefficient was  $0.23 \mu\text{s}$  long. For this model the  $\sigma$  section, Figure 6.17, is better than for the crack-model, which is due to the increased S/N ratio of the events. The reflections from the lower side of the polystyrene are weaker than from the upper side. This is slightly visible in the semblance section and quite apparent in the  $\sigma$  section.

A closer look at the results can be taken using Figures 6.18-6.20. The left polystyrene area extends from 10 to 15 cm and the upper side is at 4.5 cm depth. The extension of the imaged polystyrene is similar in the zoomed sections of the semblance and the  $\sigma$ -

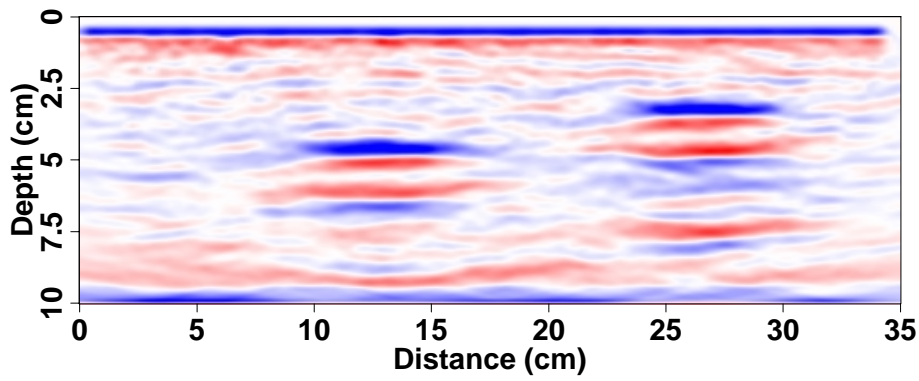


Figure 6.15: Constant velocity migration of the ZO section of Figure 6.14.

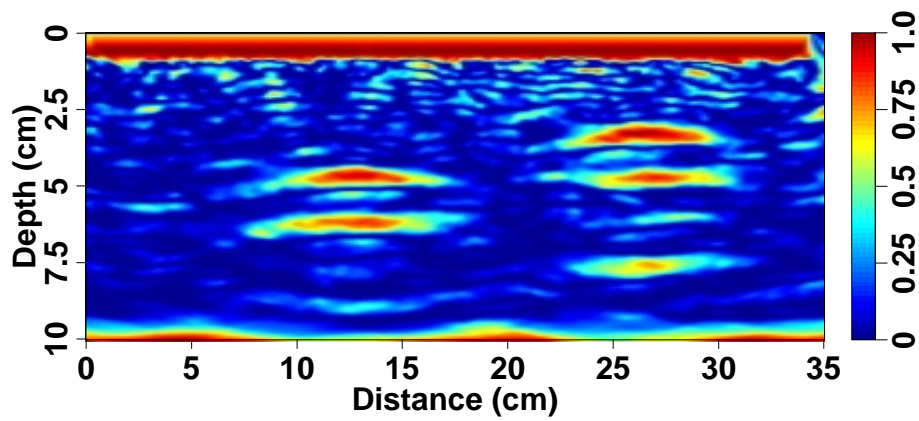


Figure 6.16: Semblance section computed during migration.

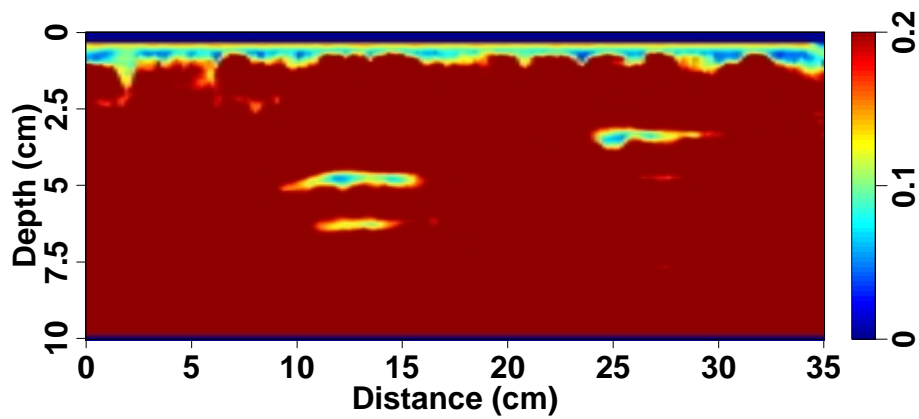


Figure 6.17:  $\sigma$  section computed during migration.

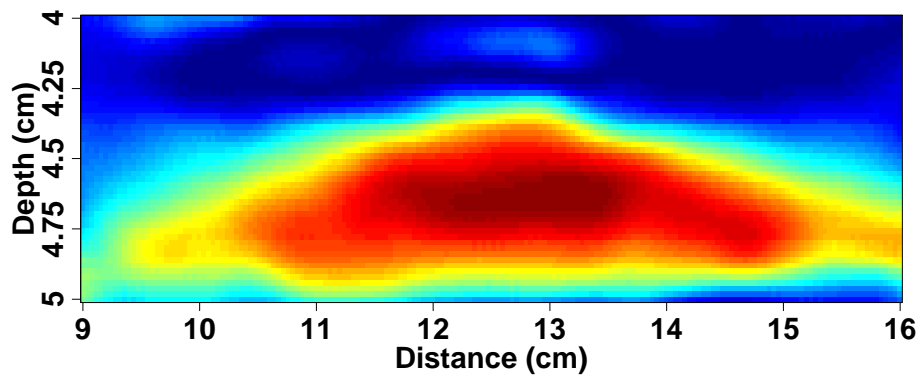


Figure 6.18: Magnification of the left polystyrene area of the semblance section.

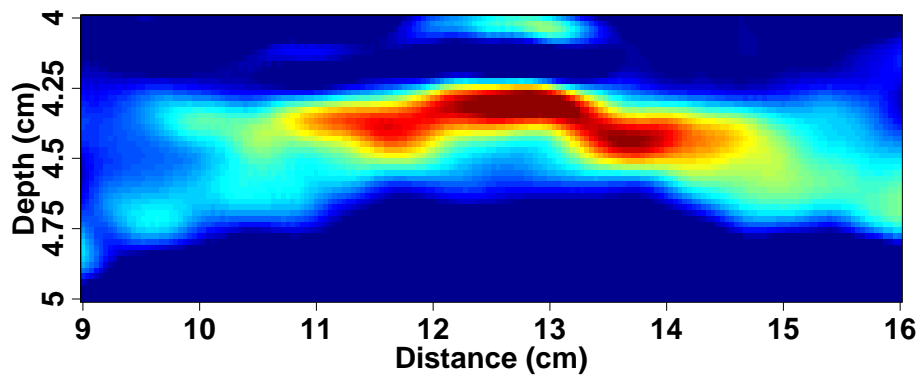


Figure 6.19: Magnification of the left polystyrene area of the semblance-derivative section.

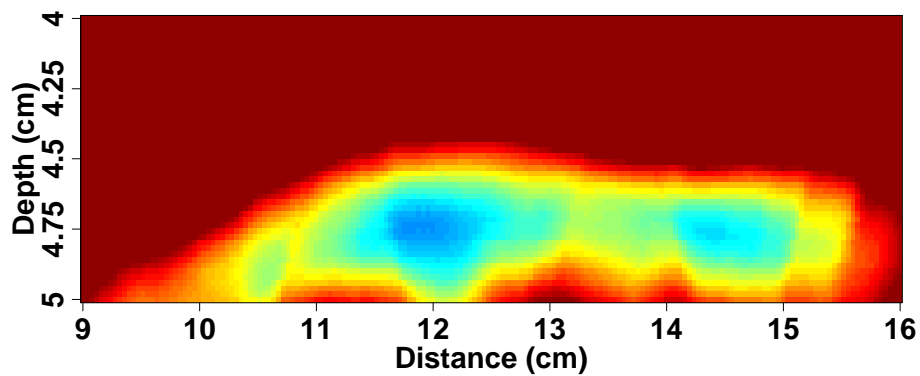


Figure 6.20: Magnification of the left polystyrene area of the  $\sigma$  section.

correlation. The width of the target zone is smaller in the semblance-derivative section. In the latter section the vertical position deviates from the exact position by approx. 2 mm. The deviation can be explained by a migration velocity that is a little too small. Due to the changing S/N ratio along the minimum phase source wavelet, the top of the polystyrene area appears in the semblance and  $\sigma$  section to be somewhere between a depth of 4.5 to 4.8 cm. The top of the area is quite straight in the  $\sigma$  section compared to the semblance section. This, I suppose, is the effect of taking the phase traveltimes into account.

## 6.5 Dip-model — The CRS Stack in NDT

If the target is parallel to the measurement surface it can be easily detected using only one transducer but if the target has got a certain dip it might not be localised. In NDT “angle beam transducers” are used to detect cracks with a certain angle to the surface normal, Bray and Stanley (1997). The disadvantage is that only a fixed angle can be tested with one special transducer. This problem could be overcome if a multi-coverage data set is acquired with many point sources and many receivers as in seismic exploration. This kind of acquisition is so far a problem in NDT because a point like transducer might not transfer enough energy into the test material. In addition, moving the transducers means to stick them on and remove them from the surface of the object many times which is very time consuming. Again, the air coupled transducer could be the solution.

In cooperation with the engineers of the sub-project A6, an experiment was designed to detect a dipping ( $45^\circ$ ) polystyrene area in concrete, Figure 6.21. The aim was to apply the CRS Stack to a NDT data set. The parameters of the geometry of source and receiver were supplied by sub-project A6. The model actually has a width of 30 cm but shown are only 20 cm as no additional information can be gained between 20 and 30 cm. For the data acquisition an extension of the model up to 30 cm was assumed to be sufficient. All up-coming sections are displayed up to a distance of 20 cm. The source had a width of 2 mm, the width of the receiver was 10 mm. 28 shot-gather with 29 receivers per shot were synthetically acquired. The first source position was at a distance of 1.6 cm and was moved 1 cm per shot to the right. The source was again a minimum phase Ricker-wavelet but with fundamental frequency of 250 kHz and a maximum frequency of 300 kHz. The physical parameters of the model were the same as in the two models above except that the porosity amounted to 2 %. After the acquisition, the direct wave was muted in the shot gathers.

The result of a simple one-transducer-experiment is depicted in Figure 6.22. A transducer with a diameter of 1 cm served as a source and a receiver. It is obvious that such a simple acquisition is not appropriate for a simple dipping object. In the Fresnel CRS Stack below it, Figure 6.24, the object is easily detectable but it has to be migrated into the correct position. Only in comparison with the Fresnel CRS Stack, the reflection from the polystyrene can be identified in the simple ZO experiment, Figure 6.22. The migrated reflection in Figure 6.23 coincides with the model at the top of the polystyrene and has the right dip but the positive lobe of the wavelet does not extend to the bottom of the polystyrene. A migration velocity of  $v_{eff} = 3500$  m/s was used. The envelope of the migrated Fres-

nel CRS Stack, Figure 6.25, did produce a slight improvement compared to the migrated section with respect to S/N ratio. Although the semblance coefficients are small in Figure 6.26 in comparison to the plane wave experiments, the dipping polystyrene stands out clearly. Like the positive lobe in the migrated section, the polystyrene appears shortened compared to the model. Short period fluctuations along the object and in its vicinity are visible in the semblance section. They are the reason why the derivative of the semblance section cannot reveal the dipping object. The parameters of the  $\sigma$ -correlation were chosen within reasonable ranges. With tolerable effort, a good image of the dipping inclusion could not be obtained by means of the  $\sigma$ -correlation, see Figure 6.27.

A practical alternative would be the angle beam method. Due to lack of time, this kind of experiment could not be simulated. Practically, one would have to test many angles. The question is: Is the operating expense of multiple angle beam experiments smaller than one multi-coverage data set? For instance, five angle beam experiments would allow five certain dip angles, whereas a multi-coverage data set allows a continuous imaging of dips only limited by the acquisition aperture.

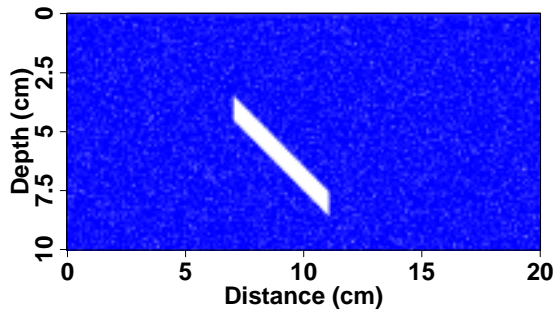


Figure 6.21: A part (10x20cm) of the dip-model.

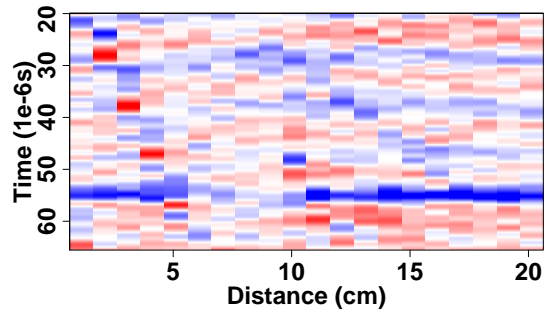


Figure 6.22: ZO section of the dip-model using a transducer with a diameter of 1cm.

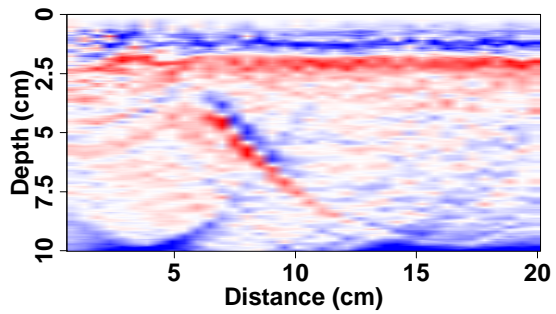


Figure 6.23: Migrated Fresnel CRS Stack.

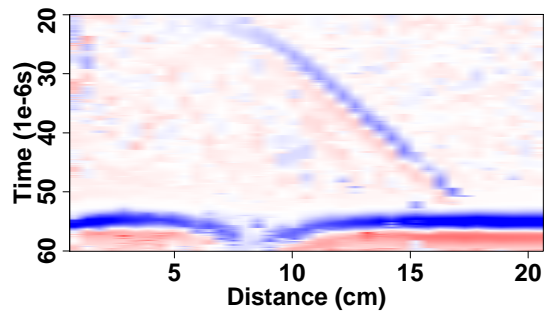


Figure 6.24: Fresnel CRS Stack.

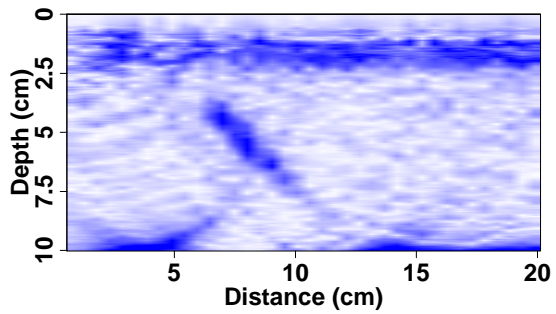


Figure 6.25: Envelope of migrated Fresnel CRS Stack.

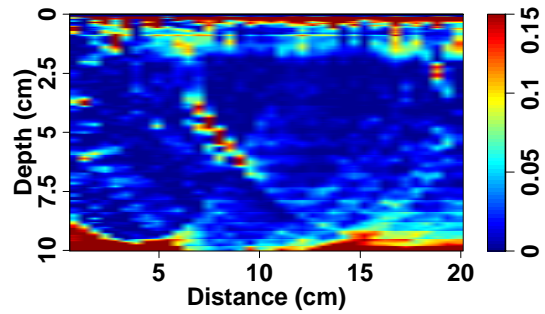


Figure 6.26: Semblance section computed during migration.

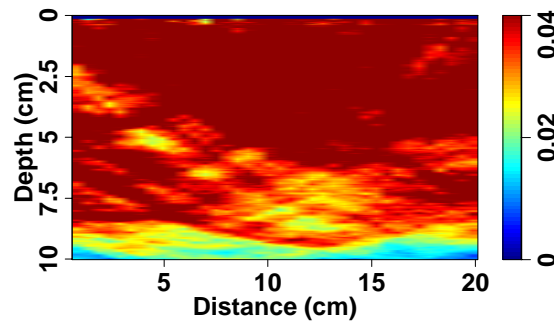


Figure 6.27:  $\sigma$  section computed during migration.

## Chapter 7

# Conclusions and perspectives

With the kinematic wavefield attributes of the CRS Stack a sequence of steps were presented in order to perform seismic imaging without the knowledge of a velocity model. In addition, the CRS Stack which was developed for reflection seismic imaging of layered media, was successfully applied, for the first time, in non-destructive testing.

The projected Fresnel zone and the geometrical spreading were expressed in terms of CRS Stack attributes. They play an important role in seismic imaging. First, the projected Fresnel zone, utilised as a minimum aperture, improves the simulated zero-offset sections. Therefore, the computation time is reduced to a minimum. Second, the capriciousness of choosing an aperture is removed by the application of the projected Fresnel zone as a minimum aperture. In addition, due to the fact that a ZO sample of the CRS Stack is associated with the normal ray, the minimum aperture is centered at the stationary point. This ensures to stack within the optimal range where the reflection signal comes from. Third, the geometrical spreading, based on the data-driven CRS Stack attributes, is a natural gain function. The natural gain function has got the effect that events at small and at large traveltimes are visible. Fourth and even more important, the amplitudes are correct with respect to the reflection coefficients. Thus, it is possible to use the GS corrected zero-offset sections for geological interpretation with respect to dynamics and not only with respect to the kinematics.

The CRS Stack attributes are computed for ZO. The CRS operator also includes data at finite offset. Hence, I proposed how to choose the aperture in midpoint direction for finite offsets. I recommend to implement the rotated elliptical aperture in future as it should further improve the results. The quality of the CRS Stack could not be improved by recursively computing and applying the projected Fresnel zone. My approach to obtain a ZO section with good resolution and continuous events is to choose for the parameter search an aperture rather too large than too small, compute the projected Fresnel zone, and perform a stack within those boundaries.

I presented a new parsimonious true-amplitude migration which makes extensive use of the CRS Stack attributes. A validation test concerning the TA character of the Initial and Fresnel CRS Stack revealed that the Fresnel CRS Stack is recommended for further

TA processing rather than the Initial CRS Stack. This test was necessary as these stacks serve as input for the parsimonious TA migration. The map-migrated synthetic depth section yielded the best results with respect to true-amplitude, fluctuations, and computation time. Using the coherence section of the CRS Stack for the selection of the data to be migrated, turnaround times can be additionally reduced. The application to real data was shown and is also possible in a TA sense if the 2.5-D GS is valid. So far, it is a disadvantage that the amplitude fluctuations along the picked events could not be reduced. Once the CRS Stack is available for finite offsets in 2-D or for ZO in 3-D, the parsimonious TA migration can also be extended to perform the corresponding 2-D or 3-D migration. Of course, the migration algorithm also works for macro-velocity models and is not restricted to layered models. If a ray tracer would have been available that can do ray tracing for macro-velocity models and uses the CRS Stack attributes as input, the parsimonious TA migration could have been applied to the complete BEB data set using the BEB macro-velocity model.

With the implementation of the robust locally weighted regression, it is now possible to invert CRS Stack attributes from real data to build a velocity model. The horizon inversion yielded a velocity model of the BEB data that is similar to their conventional NMO/DMO analysis. The stabilisation of the inversion of real data closes the cycle of a data-driven true-amplitude migration. Just remember that the CRS Stack does not require a velocity model, the inversion algorithm does not need an initial velocity model, and the migration makes use of the output of the horizon inversion. For more complex ZO sections, solutions are required to handle gaps in the picked events. The inversion of a blocky model would lead to layers with lateral inhomogeneities which is more realistic than the capabilities of the actual version.

The CRS Stack was also successfully applied to synthetic data in non-destructive testing. The acquisition of multi-coverage data is rarely performed in this special field. But I recommend to demand multi-coverage data, e.g., with air coupled transducers because it replaces the restricted processing of ZO or angle beam data acquisition. The conventional semblance, which is well known in geophysics, and the  $\sigma$ -correlation were applied during standard 2-D Kirchhoff migration. The aim was to better localise the boundaries of cracks or foreign bodies in concrete. While the semblance always yielded good results, the  $\sigma$ -correlation failed during the migration of the ZO section of the dip-model. Besides the encouraging quality of the semblance, it is about two orders faster than the  $\sigma$ -correlation. Additionally, I calculated the derivative of the semblance and the envelope of the image. The first increased the resolution, the second emphasised the crack region or the foreign bodies. As the computation time is negligible for the envelope and for the semblance, I propose to utilise the envelope for a rough localisation and the semblance or semblance-derivative for a detailed localisation. Unfortunately, no real data set was available to test the coherence measures or the CRS Stack. The application to real data should be a task for the future.

# References

- Aki, K., and Richards, P. G., 1980, Quantitative seismology, volume 1, Theory and Methods: W. H. Freeman and Company, New York.
- Berkhout, A., 1985, Seismic migration - imaging of acoustic energy by wave field extrapolation. Part A: Theoretical aspects: Elsevier.
- Bleistein, N., Cohen, J., and Stockwell, Jr., J., 2001, Mathematics of multidimensional seismic migration, imaging and inversion: Springer.
- Bleistein, N., 1984, Mathematics of wave phenomena: Academic Press Inc.
- Bleistein, N., 1986, Two-and-one-half dimensional in-plane wave propagation: Geophysical Prospecting, **34**, 686–703.
- Born, M., and Wolf, E., 1987, Principles of Optics - Electromagnetic Theory of Propagation, Interference and Diffraction of Light: Pergamon Press, 6th (corrected) edition.
- Bortfeld, R., 1989, Geometrical ray theory: Rays and traveltimes in seismic systems (second-order approximations of the traveltime): Geophysics, **48**, no. 3, 1342–1349.
- Bray, D. E., and Stanley, R. K., 1997, Nondestructive evaluation: a tool in design, manufacturing, and service: CRC Press.
- Bronstein, I. N., and Semendjajew, K. A., 1991, Taschenbuch der Mathematik: B. G. Teubner Verlagsgesellschaft.
- Burr, E., Vieth, K.-U., and Shapiro, S., 1998, Processing and imaging simulated ultrasonic B-scans of concrete: Otto-Graf Journal, **9**, 9–18.
- Burr, E., 1996, Theoretische Beschreibung und numerische Simulation elastischer Wellenausbreitung in zufallsverteilten Medien: Master's thesis, University of Karlsruhe.
- Červený, V., and Soares, J., 1992, Fresnel volume ray tracing: Geophysics, **57**, 902–915.
- Červený, V., 2001, Seismic Ray Theory: Cambridge University Press.
- Chen, Q., and Sidney, S., 1997, Seismic attribute technology for reservoir forecasting and monitoring: The Leading Edge, **16**, no. 5, 445–456.

## References

---

- Claerbout, J. F., and Doherty, S. M., 1972, Downward continuation of moveout-corrected seismograms: *Geophysics*, **37**, no. 05, 741–768.
- Claerbout, J. F., 1993, *Basic earth imaging: Stanford Exploration Project*, United States of America.
- Cleveland, W. S., 1979, Robust locally weighted regression and smoothing scatterplots: *Journal of the American Statistical Association*, **74**, 829–836.
- Deregowski, S. M., 1986, What is DMO?: *First Break*, **4**, no. 7, 7–24.
- Dix, C. H., 1955, Seismic velocities from surface measurements: *Geophysics*, **20**, no. 1, 68–86.
- Gelchinsky, B., Landa, E., and Shtivelman, V., 1985, Algorithms of phase and group correlation: *Geophysics*, **50**, no. 4, 596–608.
- Gelchinsky, B., Landa, E., and Shtivelman, V., 1986, Complex envelope and procedures of combined group and phase correlation: 56th Annual Internat. Mtg., Soc. Expl. Geophys., Expanded Abstracts, 268–270.
- Gelchinsky, B., Berkovitch, A., and Keydar, S., 1997, Multifocusing homeomorphic imaging: Parts I and II: Special Course on Homeomorphic Imaging, Seeheim, Germany, Course Notes.
- Gray, S., 1997, True-amplitude seismic migration: A comparison of three approaches: *Geophysics*, **62**, no. 3, 929–936.
- Hagedoorn, J., 1954, A process of seismic reflection interpretation: *Geophysical Prospecting*, pages 85–127.
- Hale, D., 1991, *Dip moveout processing*: Society of Exploration Geophysicists.
- Haufler, F., 2000, *Luftgekoppelter Ultraschall — Grundlagen der Anwendung bei Beton*: Master's thesis, University of Stuttgart.
- Herkenhoff, F., Cocker, J., Criddle, D., Stefani, J., and Rector, J., 2001, Some indications that relative amplitudes may be influenced by transmission more than reflection: 2nd Wave Inversion Technology Workshop on Seismic True Amplitudes, Karlsruhe (Germany), Abstracts.
- Höcht, G., de Bazelaire, E., Majer, P., and Hubral, P., 1999, Seismics and optics: hyperbolae and curvatures: *Journal of Applied Geophysics*, **42**, 261–281.
- Hua, B., and McMechan, G., 1999, Parsimonious Kirchhoff depth migration: 69th Annual Internat. Mtg., Soc. Expl. Geophys., Expanded Abstracts, 1382–1385.
- Hubral, P., and Krey, T., 1980, Interval velocities from seismic reflection travelttime measurements: *Soc. Expl. Geophys.*

- 
- Hubral, P., Schleicher, J., and Tygel, M., 1992a, Three-dimensional paraxial ray properties, Part I: Basic relations: *Journal of Seismic Exploration*, **1**, 265–279.
- Hubral, P., Schleicher, J., and Tygel, M., 1992b, Three-dimensional paraxial ray properties, Part II: Applications: *Journal of Seismic Exploration*, **1**, 347–362.
- Hubral, P., Schleicher, J., and Tygel, M., 1993a, Three-dimensional primary zero-offset reflections: *Geophysics*, **58**, no. 5, 692–702.
- Hubral, P., Schleicher, J., Tygel, M., and Hanitzsch, C., 1993b, Determination of Fresnel zones from travelttime measurements: *Geophysics*, **58**, no. 5, 703–712.
- Hubral, P., Höcht, G., and Jäger, R., 1999, Seismic illumination: *The Leading Edge*, **18**, no. 11, 1268–1271.
- Hubral, P., 1977, Time migration - Some ray theoretical aspects: *Geophys. Prosp.*, **25**, no. 04, 738–745.
- Hubral, P., 1983, Computing true amplitude reflections in a laterally inhomogeneous earth: *Geophysics*, **48**, no. 8, 1051–1062.
- Hubral, P., Ed., 1999, Macro-model independent seismic reflection imaging, volume 42, no. 3,4, *Journal of Applied Geophysics*.
- Jäger, R., Mann, J., Höcht, G., and Hubral, P., 2001, Common-reflection-surface stack: Image and attributes:, **66**, no. 1.
- Jäger, R., 1999, *The Common Reflection Surface Stack - Theory and Application*: Master's thesis, University of Karlsruhe, Germany.
- Karrenbach, M., 1995, *Elastic tensor wavefields*: Ph.D. thesis, Stanford University.
- Katz, S., and Henyey, T., 1992, Post-stack diffraction-type migration of the signal component of the wavefield: *Geophys. J. Int.*, **109**, 517–524.
- Kelly, K. R., Ward, R. W., Treitel, S., and Alford, R. M., 1976, Synthetic seismograms: A finite-difference approach: *Geophysics*, **41**, no. 1, 2–27.
- Keydar, S., Landa, E., Gelchinsky, B., and Belfer, I., 1998, Multiple prediction using the homeomorphic-imaging technique: *Geophys. Prosp.*, **46**, no. 4, 423–440.
- Knapp, R. W., 1991, Fresnel zones in the light of broadband data: *Geophysics*, **56**, 354–359.
- Kravtsov, Y. A., and Orlov, Y. I., 1980, *Geometrical optics of inhomogeneous media*: Moscow: Nauka.
- Kvasnička, M., and Červený, V., 1996, Analytical expressions for Fresnel volumes and interface Fresnel zones of seismic body waves. Part 1: Direct and unconverted reflected waves: *Studia geophysica et geodeatica*, **40**, 136–155.

## References

---

- Langenberg, K.-J., Fellingner, P., Marklein, R., Zanger, P., Mayer, K., and Kreutter, T., 1993, Inverse methods and imaging, in *Evaluation of materials and structures by quantitative ultrasonics*, Springer, 317–398.
- Majer, P., 2000, Inversion of seismic parameters: Determination of the 2-D iso-velocity layer model: Master's thesis, University Karlsruhe, Germany.
- Mann, J., Jäger, R., Müller, T., Höcht, G., and Hubral, P., 1999, Common-reflection-surface stack - a real data example: *Journal of Applied Geophysics*, **42**, 301–318.
- Mann, J., 2000, Common-reflection-surface stack (user's manual): Geophysical Institute, University of Karlsruhe, 4.1b edition.
- Mauch, R., 1999, Coherency analysis of seismic data: Master's thesis, University of Karlsruhe.
- Müller, T., 1999, The Common Reflection Surface Stack Method - Seismic imaging without explicit knowledge of the velocity model: Ph.D. thesis, University of Karlsruhe, Germany.
- Neidell, N. S., and Taner, M. T., 1971, Semblance and other coherency measures for multichannel data: *Geophysics*, **36**, no. 3, 482–497.
- Nelder, J. A., and Mead, R., 1965, A simplex method for function minimization: *Computer Journal*, **7**, 308–313.
- Newman, P., 1973, Divergence effects in a layered earth: *Geophysics*, **38**, no. 3, 481–488.
- Popov, M. M., and Pšenčík, I., 1978, Computation of ray amplitudes in inhomogeneous media with curved interfaces: *Studia Geophy. et Geod.*, **22**, 248–258.
- Popov, M., 1996, Ray Theory and Gaussian Beam Method for Geophysicists: Universidade Federal da Bahia.
- Saenger, E. H., Gold, N., and Shapiro, S. A., 2000, Modeling the propagation of elastic waves using a modified finite-difference grid: *Wave Motion*, **31**, no. 1, 77–92.
- Schleicher, J., Tygel, M., and Hubral, P., 1993, Parabolic and hyperbolic paraxial two-point traveltimes in 3D media: *Geophys. Prosp.*, **41**, no. 4, 495–514.
- Schleicher, J., Hubral, P., Tygel, M., and Jaya, M. S., 1997, Minimum apertures and Fresnel zones in migration and demigration: *Geophysics*, **62**, no. 1, 183–194.
- Schleicher, J., Tygel, M., and Hubral, P., 2001, Seismic true amplitude imaging: SEG Monograph.
- Schleicher, J., 1993, Bestimmung von Reflexionskoeffizienten aus Reflexionsseismogrammen: Ph.D. thesis, University of Karlsruhe.
- Schneider, W. A., 1978, Integral formulation for migration in two and three dimensions: *Geophysics*, **43**, no. 01, 49–76.

- Shapiro, S., Schwarz, R., and Gold, N., 1996, The effect of random isotropic inhomogeneities on the phase velocity of seismic waves: *Geoph. J. Int.*, **127**, 783–794.
- Sheriff, R. E., and Geldart, L. P., 1995, *Exploration seismology*: Cambridge University Press, 2nd Edition.
- Sheriff, R., 1975, Factors affecting seismic amplitudes: *Geophysical Prospecting*, **23**, 125–138.
- Simon, M., 1998, Avo analysis by offset-limited prestack migrations of crustal seismic data: *Tectonophysics*, **11**, no. 286, 143–153.
- Strang, G., and Fix, G., 1973, *An analysis of the finite element method*: Prentice Hall.
- Sun, J., 1996, The relationship between the first Fresnel zone and the normalized geometrical spreading factor: *Geophysical Prospecting*, **44**, 351–374.
- Sun, J., 1998, On the limited aperture migration in two dimensions: *Geophysics*, **63**, no. 3, 984–994.
- Sun, J., 2000, Limited-aperture migration: *Geophysics*, **65**, no. 2, 584–595.
- Tarantola, A., 1984, Linearized inversion of seismic reflection data: *Geophysical Prospecting*, **32**, 998–1015.
- Tygel, M., Schleicher, J., and Hubral, P., 1995, Dualities between reflectors and reflection-time surfaces: *Journal of Seismic Exploration*, **4**, 123–150.
- Tygel, M., Müller, T., Hubral, P., and Schleicher, J., 1997, Eigenwave based multiparameter traveltimes expansions: 67th Annual Internat. Mtg., Soc. Expl. Geophys., Expanded Abstracts, 1770–1773.
- Tygel, M., Schleicher, J., Hubral, P., and Santos, L. T., 1998, 2.5-D true-amplitude Kirchhoff migration to zero offset in laterally inhomogeneous media: *Geophysics*, **63**, no. 2, 557–573.
- Ursin, B., 1982, Quadratic wavefront and traveltimes approximations in inhomogeneous layered media with curved interfaces: *Geophysics*, **47**, no. 7, 1012–1021.
- Vieth, K.-U., and Shapiro, S., 1999, Imaging cracks in random media using coherence techniques and complex trace analysis: 4th Int. Conf. on Theoretical and Computational Acoustics, Trieste, *Bollettino di Geofisica*, A2–10.
- Vieth, K.-U., Shapiro, S., and Hubral, P., 1999, Crack imaging in randomly heterogeneous media: *High Performance Computing in Science and Engineering*, 46–51.
- Witte, O., Roth, M., and Müller, G., 1996, Ray tracing in random media: *Geophysical Journal International*, **124**, 159–169.
- Yilmaz, O., 1987, *Seismic data processing*: Soc. Expl. Geophys.

## References

---

- Zaske, J., Keydar, S., and Landa, E., 1999, Estimation of kinematic wavefront parameters and their use for multiple attenuation: *Journal of Applied Geophysics*, **42**, no. 3-4, 333-346.
- Zhang, Y., Bergler, S., Tygel, M., and Hubral, P., 2001, Model-independent traveltime attributes for 2-D, finite-offset multi-coverage reflections: accepted by PAGEOPH.

# Appendix A

## Some properties of the ray propagator matrix

### A.1 Reverse ray

$\underline{\mathbf{T}}^*$  is the surface-to-surface ray propagator matrix of the reverse ray in which source  $S$  and receiver  $G$  are interchanged. The wave travels now along the central ray but in opposite direction. This fact is mathematically expressed by the slowness vectors of the reverse ray at  $G$  and  $S$  which have the same components as the corresponding vectors of the original ray but with opposite sign. In terms of the elements of the propagator matrix  $\underline{\mathbf{T}}$ , the reverse propagator matrix reads (Hubral, 1983; Hubral et al., 1992a)

$$\underline{\mathbf{T}}^* = \begin{pmatrix} D & B \\ C & A \end{pmatrix}. \quad (\text{A.1})$$

In the ZO situation (when the central ray reduces to the normal ray)  $\underline{\mathbf{T}} = \underline{\mathbf{T}}^*$ . Therefore, the condition

$$A = D \quad (\text{A.2})$$

holds for a normal ray.

### A.2 Symplecticity

From elementary mathematical rules, it is known that Equation (2.15) is only integrable if its expression on the right-hand side is a total differential. This is the case if the mixed second-order derivatives of  $t$  are independent of the order of differentiation, i.e.

$$\frac{\partial^2 t}{\partial x \partial x'} = \frac{\partial p}{\partial x'} \stackrel{!}{=} -\frac{\partial p'}{\partial x} = \frac{\partial^2 t}{\partial x' \partial x}. \quad (\text{A.3})$$

Taking equations (2.16) and (2.17) into account this condition reads

$$B^{-1} = - \left( C - D B^{-1} A \right) \quad (\text{A.4})$$

or

$$AD - BC = 1. \quad (\text{A.5})$$

This is the symplectic property of the  $2 \times 2$  matrix  $\underline{\mathbf{T}}$ . According to Červený (2001), I can write the symplectic property in the form

$$\underline{\mathbf{T}}^T \underline{\mathbf{J}} \underline{\mathbf{T}} = \underline{\mathbf{J}}, \quad (\text{A.6})$$

where  $\underline{\mathbf{T}}^T$  is the transposed matrix of  $\underline{\mathbf{T}}$  and  $\underline{\mathbf{J}}$  is the  $2 \times 2$  matrix given by

$$\underline{\mathbf{J}} = \begin{pmatrix} 0 & 1 \\ -1 & 0 \end{pmatrix}. \quad (\text{A.7})$$

### A.3 Chain rule

The chain rule states that for any point  $M$  along the central ray  $SMG$  the surface-to-surface propagator matrix  $\underline{\mathbf{T}}$  satisfies the equation

$$\underline{\mathbf{T}}(G, S) = \underline{\mathbf{T}}(G, M) \underline{\mathbf{T}}(M, S). \quad (\text{A.8})$$

$\underline{\mathbf{T}}(G, M)$  and  $\underline{\mathbf{T}}(M, S)$  denote the propagator matrices for the ray branches  $SM$  and  $MG$  that build up the ray  $SMG$ . This equation holds for all points  $M$ , no matter if  $M$  lies upon an actual reflecting or transmitting interface or an arbitrarily introduced fictitious interface. If I denote the elements of the propagator matrix of the first ray branch  $SM$  by  $A_1, B_1, C_1$ , and  $D_1$  and the elements of the second ray branch by  $A_2, B_2, C_2$ , and  $D_2$  the elements of the whole ray  $SMG$  can be expressed by

$$A = A_2 A_1 + B_2 C_1, \quad (\text{A.9a})$$

$$B = A_2 B_1 + B_2 D_1, \quad (\text{A.9b})$$

$$C = C_2 A_1 + D_2 C_1, \quad (\text{A.9c})$$

$$D = C_2 B_1 + D_2 D_1. \quad (\text{A.9d})$$

Just as  $\underline{\mathbf{T}}(G, S)$  can be decomposed into the product of  $\underline{\mathbf{T}}(G, M)$  and  $\underline{\mathbf{T}}(M, S)$ , the latter two ray-branch propagator matrices may be further decomposed. This means that ultimately the propagator matrix  $\underline{\mathbf{T}}$  can be written as a product of many ray-segment propagator matrices. This general decomposition is referred to as chain rule of the  $\underline{\mathbf{T}}$  propagator matrix.

## Appendix B

# Projected Fresnel zone - finite-offset configuration

This Appendix shows that it is possible to express Kvasnička and Červený (1996) analytical expression of the interface radius, Equation (3.13), in terms of the CRS attributes. This radius is then projected onto the acquisition line along the paraxial reflection rays. Although, it can be expressed analytically, it is not possible to compute it straight forward. This is due to the fact that the paraxial reflection rays have to obey the boundary condition that their traveltimes have to differ by  $T/2$  compared to the traveltimes of their, in  $Q$ , diffracted rays, see Figure B.1. A range of reflection angles,  $\Psi_1$  and  $\Psi_2$ , has to be tested to fulfill the  $T/2$ -condition. These calculations, expressed in terms of the CRS attributes, are performed in order to compare this analytically expressed projected Fresnel zone with the one using the parabolic and hyperbolic traveltime approximations (3.2) and (3.3), respectively.

All subsequent variables are depicted in Figures 3.5 and B.1. For simplicity, it is assumed that the acquisition line is at  $z = 0$ . The origin of coordinates is located at the midpoint, *CMP*. Here, the emergence angle,  $\alpha$ , is positive if the ray emerges on the right of the surface normal, otherwise it is negative. The surface normal points in positive  $z$ -direction. The angle is counted from the normal to the surface. The same convention holds for the dip, i.e., it is positive in Fig. B.1. The source is assumed to be on the up-dip side.

The source, receiver and normal incidence point are expressed by:

$$\mathbf{S} = (-h, 0)^T, \quad \mathbf{G} = (h, 0)^T, \quad \mathbf{NIP} = R_{NIP}(\sin \alpha, \cos \alpha)^T, \quad (\text{B.1})$$

where  $T$  denotes transpose. The distance between the source/receiver and its projection onto the reflector along the reflector normal equals:

$$z_S = R_{NIP} - h \sin |\alpha|, \quad z_G = R_{NIP} + h \sin |\alpha|. \quad (\text{B.2})$$

Thus, the endpoint of the projection of the source is:

$$\mathbf{Sp} = \mathbf{S} + (z_S \sin \alpha, z_S \cos \alpha)^T. \quad (\text{B.3})$$

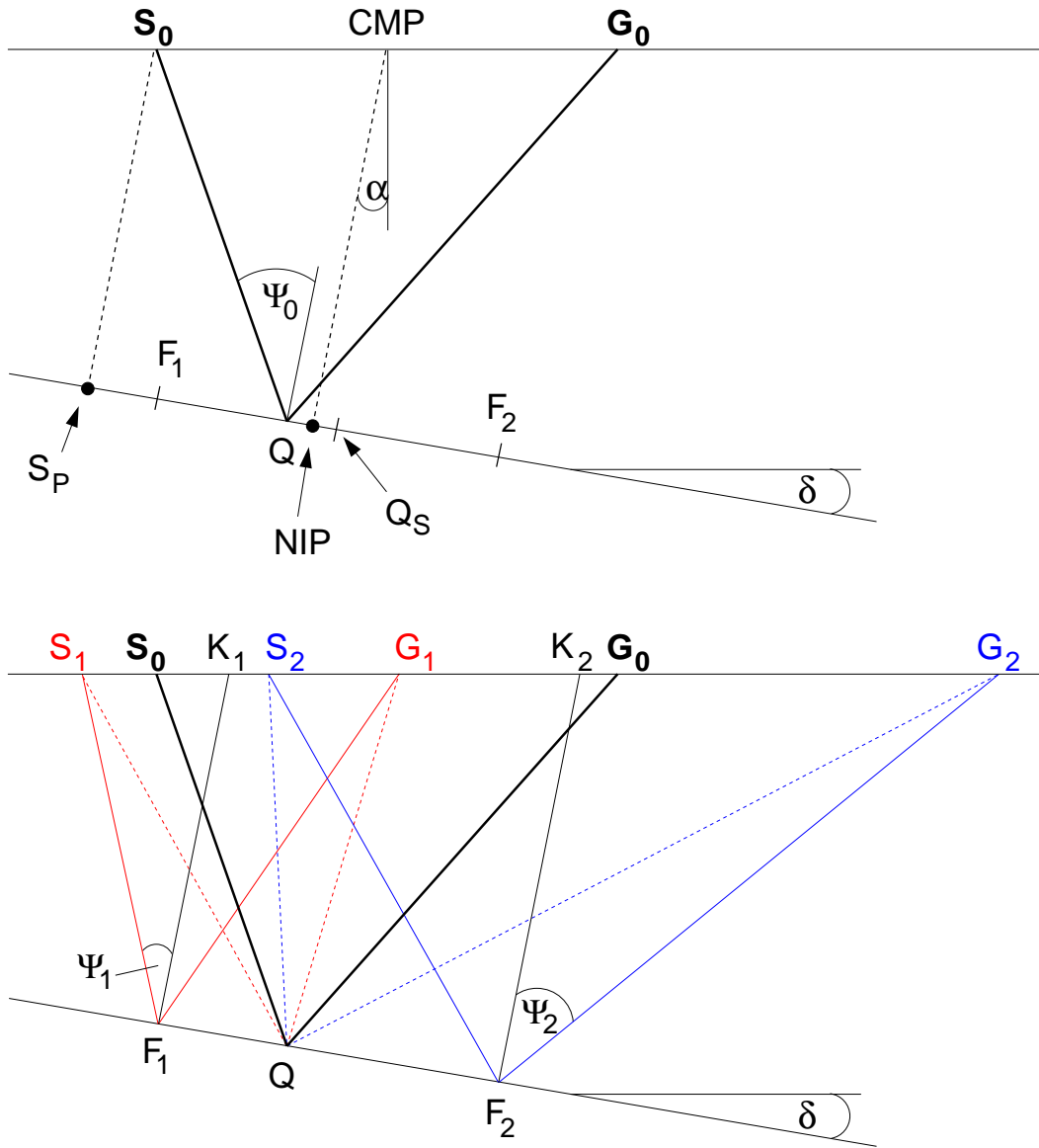


Figure B.1: The sketch serves for the description how to project the analytically expressed interface Fresnel zones for finite offset.

The following distances

$$|\mathbf{SpNIP}| = \frac{h}{\cos \alpha}, \quad |\mathbf{QNIP}| = \frac{h^2 \cos \delta \sin \delta}{R_{NIP}} \quad (\text{B.4})$$

and the so-called off-ray shift of the interface Fresnel zone, Kvasnička and Červený (1996), which describes the distance between the reflection point  $Q$  and the centre of the interface Fresnel zone  $Q_S$ :

$$d = \frac{|mg|\nu^2 \sqrt{1+g^2}}{1+g^2\nu^2}. \quad (\text{B.5})$$

Here, I stuck to the notation of the interface Fresnel zone,  $r$ , expressed by Equation 3.13. Now, the vectors associated with the reflection point,  $Q$ , the centre of the interface Fresnel zone,  $Q_S$ , and the boundaries of the interface Fresnel zone,  $F_1$  and  $F_2$ , are given by:

$$\mathbf{Q} = \mathbf{NIP} - |\mathbf{QNIP}| (\cos \alpha, -\sin \alpha)^T, \quad \mathbf{Q}_S = \mathbf{Q} + d (\cos \alpha, -\sin \alpha)^T \quad (\text{B.6})$$

$$\mathbf{F}_1 = \mathbf{Q}_S + r (\cos \alpha, -\sin \alpha)^T, \quad \mathbf{F}_2 = \mathbf{Q}_S - r (\cos \alpha, -\sin \alpha)^T \quad (\text{B.7})$$

Next, the projections of  $F_1$  and  $F_2$  along the interface normals to the surface have to be calculated. For this, various distances are needed:

$$|\mathbf{SpF}_1| = |\mathbf{SpNIP}| - |\mathbf{QNIP}| - r + d, \quad |\mathbf{SpF}_2| = |\mathbf{SpF}_1| + 2r \quad (\text{B.8})$$

$$|\mathbf{F}_1 \mathbf{K}_1| = z_S |\mathbf{SpF}_1| \tan |\alpha|, \quad |\mathbf{F}_2 \mathbf{K}_2| = z_S |\mathbf{SpF}_2| \tan |\alpha|. \quad (\text{B.9})$$

Thus, the projections yield:

$$\mathbf{K}_1 = (F_{1,X} + |\mathbf{F}_1 \mathbf{K}_1| \sin |\alpha|, 0)^T, \quad \mathbf{K}_2 = (F_{2,X} + |\mathbf{F}_2 \mathbf{K}_2| \sin |\alpha|, 0)^T, \quad (\text{B.10})$$

where the  $x$ -component of the vectors  $\mathbf{F}_1$  and  $\mathbf{F}_2$  are denoted by  $F_{1,X}$  and  $F_{2,X}$ . The emergence angles of the reflected paraxial rays at  $S_1$ ,  $S_2$ ,  $G_1$ , and  $G_2$  have to be determined:

$$\xi_{S_1} = \frac{\pi}{2} - \alpha - \Psi_1, \quad \xi_{G_1} = \frac{\pi}{2} + \alpha - \Psi_1 \quad (\text{B.11})$$

$$\xi_{S_2} = \frac{\pi}{2} - \alpha - \Psi_2, \quad \xi_{G_2} = \frac{\pi}{2} + \alpha - \Psi_2. \quad (\text{B.12})$$

Application of the sine law yields:

$$|\mathbf{S}_1 \mathbf{K}_1| = |\mathbf{F}_1 \mathbf{K}_1| \frac{\sin \Psi_1}{\sin \xi_{S_1}}, \quad |\mathbf{G}_1 \mathbf{K}_1| = |\mathbf{F}_1 \mathbf{K}_1| \frac{\sin \Psi_1}{\sin \xi_{G_1}} \quad (\text{B.13})$$

$$|\mathbf{S}_2 \mathbf{K}_2| = |\mathbf{F}_2 \mathbf{K}_2| \frac{\sin \Psi_2}{\sin \xi_{S_2}}, \quad |\mathbf{G}_2 \mathbf{K}_2| = |\mathbf{F}_2 \mathbf{K}_2| \frac{\sin \Psi_2}{\sin \xi_{G_2}}. \quad (\text{B.14})$$

This leads to the locations of the sources and receivers of the paraxial rays:

$$\mathbf{S}_1 = (K_{1,X} - |\mathbf{S}_1 \mathbf{K}_1|, 0)^T, \quad \mathbf{G}_1 = (K_{1,X} - |\mathbf{G}_1 \mathbf{K}_1|, 0)^T \quad (\text{B.15})$$

$$\mathbf{S}_2 = (K_{2,X} - |\mathbf{S}_2 \mathbf{K}_2|, 0)^T, \quad \mathbf{G}_2 = (K_{2,X} - |\mathbf{G}_2 \mathbf{K}_2|, 0)^T. \quad (\text{B.16})$$

In practice, at this point of the calculations it is possible to test whether the correct reflection angles  $\Psi_1$ ,  $\Psi_2$  have been chosen or not because all coordinates are known to compute the reflection and diffraction rays. Eventually, the size of the projected interface Fresnel zone is obtained by:

$$F_P = |\mathbf{G}_1 \mathbf{G}_2|. \quad (\text{B.17})$$



# Index

- acoustic wave equation, 6
- amplitude factors, 45
- caustic
  - phase shift, 18
  - point, 17
- chain rule, 13
- duality points, 14
- eigenwaves, 23
- eikonal equation, 7
- elements, 10
- envelope, 77
- Fresnel
  - section, 29
  - volume, 29
- Fresnel zone, 11
  - projected, 13
- geometrical spreading, 16
  - 2.5-D, 19
  - factor, 17
  - in-plane, 19
  - normalised, 18
  - out-of-plane, 19
- Hooke's law, 5
- image, 13
- map-migrated, 53
- moveout
  - dip, 22
  - normal, 21
- multifocus formula, 25
- N-wave, 23
- NIP-wave, 23
- ray Jacobian, 7, 17
- ray section, 16
  - elementary, 16
- ray theory, 5
- refraction law, 23, 66
- semblance, 77
- Snell's law, 66
- spherical divergence, 16
- Stack
  - Automatic CMP, 27
  - CRS, 21
  - Fresnel CRS, 34
  - Initial CRS, 27
  - Optimised, 27
  - Plane wave, 27
- stack-migrated, 53
- stationary point, 14, 49
- transducer, 76
- transmission law, 23, 66
- transport equation, 7
- true-amplitude, 16
- true-amplitude migration, 45



# Danksagung

Herrn Prof. Dr. Peter Hubral danke ich für die Übernahme des Hauptreferats. Für die Möglichkeit verschiedene Bereiche in und außerhalb der Geophysik kennen zu lernen danke ich ihm. Ich finde es bemerkenswert, mit welcher Unermüdlichkeit er seinen Doktoranden und Studenten beibringt, sich und ihre Arbeit zu präsentieren. Davon habe ich sehr profitiert.

Herrn Prof. Dr. Serge Shapiro danke ich für die Übernahme des Korreferats, für die Anregungen und sein Interesse an der Arbeit. Seine sehr fröhliche und positive Art war immer sehr motivierend.

Frau Payne danke ich für die permanente Hilfsbereitschaft und Unterstützung. Sie behält immer die Ruhe und den Überblick und hat stets einen guten Spruch auf den Lippen.

Dr. Andreas Kirchner war fast drei Jahre mein „Mitbewohner“. Wir haben viel Spaß und viele interessante Diskussionen gehabt. Wenn Andreas einen Text Korrektur gelesen hat, konnte man sich darauf verlassen, dass er gründlichst auf Inhalt, Stil und Rechtschreibung achtete. Freundlicherweise korrigierte Andreas auch nach dem Verlassen vom GPI große Teile dieser Arbeit, wofür ich ihm sehr dankbar bin.

Alexander Goertz danke ich für die schöne Zeit während des Studiums und der Promotionszeit. Die fachlichen und privaten Gespräche habe ich immer sehr geschätzt. Auch ihm danke ich für das Korrekturlesen.

Thomas Hertweck danke ich für viele gute Diskussionen und viele gute Korrekturen in der Arbeit. Auch wenn er viel um die Ohren hat, nimmt er sich Zeit. Sein Engagement ist wirklich beispielhaft.

Den „CRS-men“ Jürgen Mann und German Höcht danke ich für die programmiertechnische Unterstützung und für das Korrigieren der Arbeit.

Matthias Riede danke ich für die guten „true-amplitude migration“-Diskussionen.

Bei Prof. Dr. Lucio Santos und Prof. Dr. Jörg Schleicher aus Campinas (Brasilien) möchte ich mich für zahlreiche gute Diskussionen während ihres Aufenthaltes in Karlsruhe bedanken.

Dr. Christian Große (Universität Stuttgart) danke ich für die gute Zusammenarbeit im SFB 381.

Der BEB Erdöl und Erdgas GmbH danke ich für die Bereitstellung der Realdaten.

Wenn es abends um 23.00 Uhr zu Hause geklingelt hat, war das die richtige Zeit, um zum Entspannen noch ein Bierchen mit Dr. Jörg Zaske zu trinken und noch 'n Hammer zu essen.

Meinen Hiwis Christoph Jäger, Erik Ewig und Ingo Koglin danke ich für die Unterstützung bei vielen Tätigkeiten und bei der Erstellung vieler Bilder.

Ich möchte hier hervorheben, dass die Arbeit in der Arbeitsgruppe von Prof. Dr. Peter Hubral sehr interessant war und viel Spaß gemacht hat. Die tolle Arbeitsatmosphäre wurde von allen Mitarbeitern getragen und trug uns alle.

Meiner Mutter und ihrem Lebensgefährten danke ich für die Unterstützung während des Studiums und der Promotionszeit. Sie haben mir das Privileg einer so langen Ausbildung ermöglicht.

Der größte Dank geht an meine geliebte Frau Anke, die mich immer motiviert hat, wenn es mal nicht so lief, die viele Wochenenden allein auf die Kinder aufgepasst hat, wenn ich am Institut war und die mich immer verwöhnt hat. Meinen Kindern Elena und Peter danke ich für die fröhliche und lustige Zeit auf Spielplätzen, in Schwimmbädern, im Zoo und zu Hause.

Die schönsten Wochenenden habe ich bzw. wir unseren Freunden Sabine und Hartmann mit ihren vier Kindern Katharina, Michaela, Carolin und Leon zu verdanken. Da Elena Urlaub hatte, habe ich bei ihnen die ersten dreißig Seiten in Ruhe unterm Dach geschrieben.

# Lebenslauf

## Persönliche Daten

Name: Kai-Uwe Vieth  
Geburtsdatum: 16.10.1969  
Geburtsort: Wilhelmshaven  
Nationalität: Deutsch  
Stand: verheiratet mit Anke Lüttich  
Kinder: Elena Charlotte (5) und Peter Tom (3/4)

## Schulbildung

1976 – 1980 Grundschule, Wilhelmshaven  
1980 – 1982 Orientierungsstufe, Wilhelmshaven  
1982 – 1986 Max-Planck Gymnasium, Wilhelmshaven  
1987 John-Wycliffe-Christian School, Warrimoo (Australien)  
1988 – 1990 Max-Planck Gymnasium, Wilhelmshaven

## Hochschulbildung

1991 – 1998 Studium der Geophysik an der  
Universität Karlsruhe  
26.03.1998 Diplom  
seit 01.04.1998 Doktorand an der Fakultät für Physik  
der Universität Karlsruhe

